

**US Army Corps
of Engineers®**
Engineer Research and
Development Center

ERDC
INNOVATIVE SOLUTIONS
for a safer, better world

Airfield Damage Repair Modernization Program

AM2 Brickwork Pattern Evaluation

Lyan Garcia, Jeff Fisher, Timothy W. Rushing, and
Jeb S. Tingle

December 2016



The U.S. Army Engineer Research and Development Center (ERDC) solves the nation's toughest engineering and environmental challenges. ERDC develops innovative solutions in civil and military engineering, geospatial sciences, water resources, and environmental sciences for the Army, the Department of Defense, civilian agencies, and our nation's public good. Find out more at www.erdcl.usace.army.mil.

To search for other technical reports published by ERDC, visit the ERDC online library at <http://acwc.sdp.sirsi.net/client/default>.

AM2 Brickwork Pattern Evaluation

Lyan Garcia, Timothy W. Rushing, and Jeb S. Tingle

*Geotechnical and Structures Laboratory
U.S. Army Engineer Research and Development Center
3909 Halls Ferry Road
Vicksburg, MS 39180-6199*

Jeff Fisher

*Applied Research Associates
430 West 5th Street, Suite 700
Panama City, FL 32401*

Final report

Approved for public release; distribution is unlimited.

Prepared for Headquarters, Air Force Civil Engineer Center
Tyndall Air Force Base, FL 32403-5319

Abstract

AM2 airfield matting has a long history of successful performance as an expeditionary airfield surfacing system. The U.S. Marine Corps established different lay patterns to assemble AM2 mat expanses that can be used to form aircraft operating surfaces. A program was initiated by the Naval Air Systems Command to evaluate and identify optimal AM2 lay patterns under different traffic conditions and to validate a Dynamic Interface Model with mat breakage, deformation, and recorded strain data. The efforts of the test program discussed in this report focused on evaluating an AM2 surface installed in a brickwork pattern on both a uniform subgrade surface and a subgrade with artificial voids to determine the effect of voids beneath the mat on the structural integrity of AM2. The mat surface was subjected to simulated F-15E and C-17 traffic while monitoring damage, deformation, and strain response. Premature failure was observed, but posttest investigations and analyses revealed a manufacturing error that produced a weak end connector design. This report provides test results for each evaluation and discussions comparing their performance to previous tests conducted under similar conditions.

DISCLAIMER: The contents of this report are not to be used for advertising, publication, or promotional purposes. Citation of trade names does not constitute an official endorsement or approval of the use of such commercial products. All product names and trademarks cited are the property of their respective owners. The findings of this report are not to be construed as an official Department of the Army position unless so designated by other authorized documents.

DESTRUCTION NOTICE - For classified documents, follow the procedures in DOD5200.22-M, Industrial Security Manual, Section II-19, or DOD 5200.1-R, Information Security Program Regulation, Chapter IX. For unclassified, limited documents, destroy by any method that will prevent disclosure of contents or reconstruction of the document.

Contents

Abstract.....	ii
Figures and Tables.....	v
Preface	ix
Unit Conversion Factors.....	x
1 Introduction	1
1.1 Background	1
1.1.1 Naval Air Systems Command Dynamic Interface Model	1
1.1.2 AM2 certified configuration lay patterns	1
1.1.3 AM2 brickwork lay pattern and NAVAIR void criteria	3
1.2 Objective and scope	4
2 Materials	5
2.1 AM2 airfield mat.....	5
2.2 High-plasticity clay (CH) subgrade	6
3 Experimental Program	9
3.1 Test section general description.....	9
3.2 Test section construction	13
3.2.1 Subgrade construction and posttest forensics	13
3.2.2 AM2 strain gauge instrumentation	16
3.2.3 AM2 mat installation.....	21
3.3 Traffic application	24
3.3.1 F-15E load cart.....	25
3.3.2 C-17 load cart.....	26
3.4 Data collection	27
3.4.1 Centerline profile.....	28
3.4.2 Unloaded cross sections.....	28
3.4.3 Loaded cross sections	28
3.4.4 Dynamic deflection	31
3.4.5 Strain measurements	31
3.4.6 Borescope observation and void depth measurement.....	31
3.5 Failure criteria	32
3.5.1 Mat breakage criteria	33
3.5.2 Permanent deformation criteria.....	33
4 Mat breakage	35
4.1 Results.....	35
4.1.1 F-15E-V item	35
4.1.2 F-15E item	38
4.1.3 C-17 item	43

4.2	Analysis	45
4.2.1	F-15E-V item	45
4.2.2	F-15E item	47
4.2.3	C-17 item	47
5	Permanent deformation	48
5.1	Results.....	48
5.1.1	F-15E-V item	48
5.1.2	F-15E item	51
5.1.3	C-17 item	54
5.1.4	Summary	57
5.2	Void measurements in the F-15E-V item.....	58
5.3	Analysis	59
5.3.1	F-15E-V item	59
5.3.2	F-15E item	60
5.3.3	C-17 item	60
6	Elastic Deflection	62
6.1	Results.....	62
6.2	Analysis	62
7	Strain Data	66
7.1	Results.....	66
7.1.1	F-15E-V item	66
7.1.2	F-15E item	70
7.1.3	C-17 item	75
7.2	Analysis	81
7.2.1	F-15E-V item	81
7.2.2	F-15E item	86
7.2.3	C-17 item	89
8	Conclusions and Recommendations	91
8.1	Conclusions.....	91
8.2	Recommendations	92
	References.....	94
	Appendix A: F-15E-V Item Strain Gage Data Summary	96
	Appendix B: F-15E Item Strain Gage Data Summary	101
	Appendix C: C-17 Item Strain Gage Data Summary	106
	Report Documentation Page	

Figures and Tables

Figures

Figure 2.1. F71 (left) and F72 (right) mat packages.....	6
Figure 2.2. AM2 (a) overlap/underlap and (b) male/female hinge connections.....	6
Figure 2.3. Gradation curve for Vicksburg Buckshot CH.....	7
Figure 2.4. Dry density vs. moisture content for CH subgrade material.	8
Figure 2.5. CBR vs. moisture content for CH subgrade material.	8
Figure 3.1. Test section profile.....	9
Figure 3.2. AM2 brickwork pattern on voided subgrade panel layout.....	11
Figure 3.3. AM2 brickwork pattern panel layout.	12
Figure 3.4. Test section excavation (left) lined with impervious sheeting (right).	14
Figure 3.5. Pulverizing CH (left) and adding moisture (right).....	14
Figure 3.6. Leveling (left) and compacting (right) CH.	15
Figure 3.7. Nuclear gage (left) and CBR test (right).	15
Figure 3.8. Strain gauge locations on upper underlap and lower overlap regions.....	18
Figure 3.9. Typical strain gauge installation on lower overlap region.....	18
Figure 3.10. F-15E-V item instrumentation layout.	19
Figure 3.11. F-15E and C-17 items instrumentation layout.....	20
Figure 3.12. Void installation on subgrade surface.	21
Figure 3.13 Insertion of aluminum locking bar between adjacent panels.....	22
Figure 3.14. Installation of AM2 panels on the test section subgrade.	22
Figure 3.15. Typical Installation of male keylock.....	23
Figure 3.16. F-15E-V item.	24
Figure 3.17. F-15E (left) and C-17 (right) items.....	24
Figure 3.18. F-15E test load cart.....	25
Figure 3.19. Plan view showing F-15E normally distributed traffic lanes.	26
Figure 3.20. C-17 test load cart.....	27
Figure 3.21. Plan view showing C-17 normally distributed traffic lanes.	27
Figure 3.22. Data collection layout for F-15E-V item.	30
Figure 3.23. Data collection layout for F-15E and C-17 items.....	30
Figure 3.24. Surveying unloaded (left) and loaded (right) cross section.	31
Figure 3.25. Prism mounted on F-15E load cart.....	32
Figure 3.26. Borescope (left) and void depth measurement (right).....	32
Figure 4.1. Layout of damaged and failed panels in the F-15-V item.....	35
Figure 4.2. Broken upper underlap rail (left) and top skin tear (right) in F81.	36
Figure 4.3. Broken end connector in F118.	36
Figure 4.4. F88 after removing from test section.	37

Figure 4.5. Layout of damaged and failed panels in the F-15E item.	39
Figure 4.6. Broken upper underlap rail in G58.	39
Figure 4.7. End connector weld failure at G23.	40
Figure 4.8. Top skin tear in G59.	40
Figure 4.9. G65 after removing from test section.	41
Figure 4.10. Crack at weld of overlap connector in G107.	41
Figure 4.11. Layout of damaged and failed panels in the C-17 item.	43
Figure 4.12. Lower overlap rail failure in G111.	44
Figure 4.13. Partial breakage of lower overlap rail in G33.	44
Figure 5.1. Subgrade centerline of the F-15E-V item after 1,008 passes.	48
Figure 5.2. Centerline profile on the mat surface of the F-15E-V item.	49
Figure 5.3. Average deformation on the subgrade of the F-15E-V item.	50
Figure 5.4. Average deformation on the loaded mat surface of the F-15E-V item.	50
Figure 5.5. Average deformation on the unloaded mat surface of the F-15E-V item.	51
Figure 5.6. Subgrade centerline profile of the F-15E item after 476 passes.	52
Figure 5.7. Centerline profile on the mat surface of the F-15E item.	52
Figure 5.8. Average deformation on the subgrade of the F-15E item.	53
Figure 5.9. Average deformation on the loaded mat surface of the F-15E item.	53
Figure 5.10. Average deformation on the unloaded mat surface of the F-15E item.	54
Figure 5.11. Subgrade centerline profile of the C-17 item after 308 passes.	55
Figure 5.12. Centerline profile on the mat surface of the C-17 item.	55
Figure 5.13. Average deformation on the subgrade of the C-17 item.	56
Figure 5.14. Average deformation on the loaded mat surface of the C-17 item.	56
Figure 5.15. Average deformation on the unloaded mat surface of the C-17 item.	57
Figure 5.16. Void depth beneath the mat throughout traffic of the F-15E-V item.	58
Figure 5.17. Pretest (a,c) and posttest (b,d) voids.	59
Figure 6.1. Elastic deflection measurements' wander distribution on F-15E-V item.	63
Figure 6.2. Elastic deflection elevation distribution on F-15E-V item.	64
Figure 6.3. Elastic deflection on F-15E-V item mat surface at various pass levels.	64
Figure 6.4. Elastic deflection on F-15E item mat surface at various pass levels.	65
Figure 7.1. F-15E-V item strain gauge layouts.	66
Figure 7.2. Panel movement for compressive and tensile strains.	67
Figure 7.3. F-15E-V item F45-F46 panel joint strains for passes 1-10.	68
Figure 7.4. F-15E-V item F45-F46 panel joint strains for passes 1-2.	68
Figure 7.5. F-15E-V item F45-F46 panel joint strains for passes 697-716.	69
Figure 7.6. F-15E item strain gauge layouts.	71
Figure 7.7. F-15E item G46-G47 panel joint strains for passes 1-10.	72

Figure 7.8. F-15E item G46-G47 panel joint strains for passes 1-2.	72
Figure 7.9. F-15E item G46-G47 panel joint strains for passes 241-267.	73
Figure 7.10. C-17 item strain gauge layouts.	75
Figure 7.11. C-17 wheel placement relative to instrumented joints.	76
Figure 7.12. Northbound C-17 load cart wheel progression, pass 1.	77
Figure 7.13. C-17 item G74-G75 panel joint strains for passes 1-12.	78
Figure 7.14. C-17 item G74-G75 panel joint strains for passes 1-2.	79
Figure 7.15. C-17 item G74-G75 panel joint strains for passes 113-140.	79
Figure 7.16. (a) Material strength properties for 6061-T6 aluminum alloy and (b) same data truncated to 10,000 microstrain.	83
Figure 7.17. Strain amplitude for gauge F81S2.	84
Figure 7.18. (a) F81-F82 joint strain data during pass 1 and (b) tire load footprint locations.	85
Figure 7.19. Strain amplitude for gauge G58S3.	86
Figure 7.20. Joint of Panels G58 and G53.	87
Figure 7.21. (a) G58-G59 joint strain data during pass 1, and (b) tire load footprint locations.	88
Figure 7.22. Strain amplitude data for gauge G50S2.	89
Figure 7.23. G50-G51 joint strain data during pass 1.	90

Tables

Table 1.1. AM2 testing program.	2
Table 1.2. Summary of AM2 brickwork pattern subgrade sensitivity testing results.	3
Table 1.3. Summary of test program.	4
Table 2.1. AM2 mat properties.	5
Table 2.2. Laboratory tests for Vicksburg Buckshot CH.	6
Table 3.1. Void locations and descriptions.	13
Table 3.2. Field tests on each constructed lift.	15
Table 3.3. Average in situ properties of the subgrade in each test item.	17
Table 3.4. Strain gauges in each test item.	20
Table 3.5. Data collection intervals for F-15E traffic.	29
Table 3.6. Data collection intervals for C-17 traffic.	29
Table 4.1. Mat damage in F-15E-V item.	38
Table 4.2. Mat damage in F-15E item.	42
Table 4.3. Mat damage in C-17 item.	45
Table 5.1. Permanent deformation values for all test items.	57
Table 7.1. F-15E-V item average maximum strains.	70
Table 7.2. F-15E item average maximum strains.	74
Table 7.3. C-17 wheel load distribution relative to instrumented joints.	76

Table 7.4. C-17 item average maximum strains.80

Table 7.5. Prong thickness for five panels.....81

Preface

This study was conducted for the U.S. Naval Air Systems Command (NAVAIR) Expeditionary Airfield (EAF) team and the U.S. Air Force Civil Engineer Center (AFCEC). Technical oversight was provided by Jeb S. Tingle.

The work was performed by the Airfields and Pavements Branch (APB) of the Engineering Systems and Materials Division (ESMD), U.S. Army Engineer Research and Development Center, Geotechnical and Structures Laboratory (ERDC-GSL). At the time of publication, Dr. Timothy W. Rushing was Chief, APB; Dr. Gordon W. McMahon was Chief, ESMD; and Nicholas Boone was the Technical Director for Force Projection and Maneuver Support. The Deputy Director of ERDC-GSL was Dr. William P. Grogan and the Director was Bartley P. Durst.

COL Bryan S. Green was the Commander of ERDC, and Dr. Jeffery P. Holland was the Director.

Unit Conversion Factors

Multiply	By	To Obtain
cubic feet	0.02831685	cubic meters
feet	0.3048	meters
inches	0.0254	meters
kip-inches	112.948	newton-meters
pounds (force)	4.448222	newtons
pounds (force) per square foot	47.88026	pascals
pounds (force) per square inch	6.894757	kilopascals
pounds (mass)	0.45359237	kilograms
square feet	0.09290304	square meters
square inches	6.4516 E-04	square meters

1 Introduction

1.1 Background

1.1.1 Naval Air Systems Command Dynamic Interface Model

AM2 aluminum matting has been the primary temporary airfield matting system used by the U.S. military since the late 1960s. AM2 was developed by the U.S. Navy, but has been adopted for use by the U.S. Air Force (USAF) and U.S. Army for fixed-wing and rotary-wing operational surfaces. Over the years, AM2 has been modified to address limiting structural concerns. The current production version of AM2 is modification (Mod) 5.

An AM2 surface is composed of interlocking 2-ft by 12-ft full panels and 2-ft by 6-ft half panels that are 1.5 in. thick. An AM2 mat expanse can be assembled to form runways, vertical takeoff and landing pads, taxiways, and aircraft parking aprons. The Naval Air Systems Command (NAVAIR) developed a Dynamic Interface Model (DIM) to analyze aircraft landings and takeoffs on AM2. The model was initially validated through laboratory subscale tests, but additional development and validation was required to accurately model the matting subsurface and soil interaction for various installation patterns. Therefore, a program was initiated to validate the model through full-scale testing using simulated fighter and cargo aircraft loads. The NAVAIR Expeditionary Airfield Team (EAF) partnered with the Air Force Civil Engineer Center (AFCEC) to sponsor the evaluations listed in Table 1.1. Reports currently published documenting results are also provided in Table 1.1.

1.1.2 AM2 certified configuration lay patterns

Descriptions of the lay patterns in Table 1.1 (brickwork, 2-1, and 3-4) are provided in NAWCADLKE-MISC-48J200-0011 (Naval Air Warfare Center 2006). The alternate patterns were established as part of an initiative to optimize the use of 6-ft half panels. The original AM2 shipping package, F44, contained sixteen 12-ft panels and four 6-ft panels. Each package was designed to allow assembly of two 108-ft wide rows or four 54-ft wide rows in a brickwork configuration with no continuous longitudinal joints. The brickwork pattern assures improved load carrying capability of the system.

Since 6-ft panels are only used for the row ends, more 12-ft panels are required for assembly.

Table 1.1. AM2 testing program.

Test Sequence	Test Name	AM2 Lay Pattern	Condition of AM2 Mats	F-15E Traffic	C-17 Traffic	Reference
1	In-plane bow on asphalt surface	Brickwork	New	N/A	N/A	—
2	Vehicle braking test on asphalt surface	Brickwork	New	N/A	N/A	—
3	Brickwork on voided subgrade (CBR of 6)	Brickwork	New and Refurbished	X	-	ERDC/GSL TR-15-30
4	Brickwork on CBR of 6	Brickwork	New and Refurbished	X	X	ERDC/GSL TR-15-30
5	In-plane bow on CBR of 6	Brickwork	New	N/A	N/A	—
6	Opposite Lay on CBR of 6	Brickwork	New	X	X	ERDC/GSL TR-15-14
7	3-4 Lay on CBR of 6	3-4	New	X	X	ERDC/GSL TR-14-38
8	2-1 Lay on CBR of 6	2-1	New	X	X	—
9	Brickwork on voided subgrade (CBR of 6)	Brickwork	New	X	-	
10	Brickwork on CBR of 6	Brickwork	New	X	X	

However, ship transportation of the mats across the globe led to a need for the mats to be shipped on an International Organization of Standardization (ISO) flat racks for compatibility with other containerized goods. A decision was made by the U.S. Navy to design new AM2 shipping packages, which resulted in the F71 and F72 shipping configurations. The F71 contains eighteen 12-ft mats, and the F72 contains eighteen 6-ft mats. The new configurations allowed one F71 and one F72 to be placed end-to-end on one 20-ft ISO flat rack and optimized use of the available space. The new package configuration also reduced confusion when designing a mat surface. In some instances, F44 packages were re-bundled with different numbers of 6-ft panels inside the 12-ft mat packages. Separating the panels into the F71 and F72 packages eliminated the need to include mixed sizes in packages and improved the accuracy of panel inventories.

Optimizing the packaging and shipping of AM2 required equal numbers of 12-ft and 6-ft mat panels to be delivered with each AM2 order. Since only a fraction of the available 6-ft panels are needed to assemble a brickwork pattern, many extra 6-ft panels were unused. To optimize mat use, NAVAIR EAF created an allowance for two alternate assembly patterns, the 2-1 and the 3-4 lay patterns. Although the two patterns were approved

by NAVAIR EAF, they had not been evaluated under simulated aircraft loading conditions to determine if any reduction in the number of allowable passes was caused by the allowance of continuous longitudinal joints. Therefore, they were included in the test program.

1.1.3 AM2 brickwork lay pattern and NAVAIR void criteria

Although the brickwork pattern has been evaluated over different subgrade materials and strengths (Table 1.2), information obtained from these tests was not sufficient to validate the model. Therefore, NAVAIR and AFCEC included testing of the brickwork pattern in the program with appropriate strain gauge instrumentation at the end connector joint to provide input to the DIM. The brickwork pattern test on a subgrade with artificial voids was also included in the program to test NAVAIR criteria for the installation of AM2 on a subgrade with voids. NAWCADLKE-MISC-48J200-0011 describes a void as a space in a soil or rock mass that is not occupied by solid mineral matter. Operational realities required that some leeway be provided to accommodate small voids in the subgrade that would not affect the integrity of the AM2 mat. Therefore, the following criteria were established, according to NAWCADLKE-MISC-48J200-0011:

1. One 6-ft sheet of AM2 mat shall have no more than 1 void underneath its surface.
2. One 12-ft sheet of AM2 mat shall have no more than 2 voids underneath its surface.
3. There is no required separation distance between voids, other than the maximum allowable per individual AM2 mat sheet; however, a void cannot exist within 1 ft of any end connector of any sheet of AM2 mat.
4. There is no depth limit for a void; however, the void shall not exceed 6 in. in any horizontal dimension.

Table 1.2. Summary of AM2 brickwork pattern subgrade sensitivity testing results.

Subgrade Strength (CBR)	Sustained Traffic Passes		
	F-15E	C-17	Reference
6	1,500	1,500	Rushing and Tingle (2007)
10	3,000	6,000	Rushing et al. (2008)
15	4,100	7,000	Rushing and Mason (2008)
25	6,300	10,000	Garcia et al. (2014a)
100	23,000	^a	Garcia et al. (2014b)

^aFailure was not achieved. Trafficking was stopped because of time constraints.

1.2 Objective and scope

The objectives of the effort described herein were to:

1. Evaluate the AM2 brickwork pattern on a subgrade with a CBR of 6 under simulated F-15E and C-17 aircraft traffic.
2. Evaluate the effect of voids in the subgrade on the performance of AM2 when placed using the brickwork pattern on a subgrade with a CBR of 6 and loaded with F-15E traffic.

Each test was conducted to:

1. Determine the number of allowable passes,
2. Record strain measurements at the end connectors, and
3. Record subgrade deformation.

To accomplish these objectives, a full-scale test section was constructed with a 36-in.-deep high-plasticity clay (CH) subgrade, which had been processed to obtain a CBR of 6. Artificial voids were installed at specific locations on the subgrade surface. The AM2 mat system was installed in the brickwork pattern to conduct simulated F-15E traffic above the voided surface. After completion of this test, mat panels were removed and a new set of panels were installed next to the previously trafficked area to conduct the F-15E and C-17 traffic tests on a uniform subgrade surface. A brief summary of the test program described in this report is provided in Table 1.3.

Table 1.3. Summary of test program.

Test Section Name	Test Section Number	Test Item Name	Traffic Type	Test Sequence	Traffic Application
Brickwork on voided subgrade	1	F-15E-V	F-15E	1	Normally distributed
Brickwork	2	F-15E	F-15E	2	Normally distributed
Brickwork	2	C-17	C-17	3	Normally distributed

2 Materials

2.1 AM2 airfield mat

AM2 airfield mat was developed in the 1960s under a program sponsored by the Naval Air Engineering Center, in Philadelphia, PA. Various versions of AM2 were tested under simulated aircraft loads at the U.S. Army Engineer Waterways Experiment Station in Vicksburg, MS from 1961 through 1971 with major procurements beginning in 1965. The original AM2 mat has been modified through the years to address limiting structural concerns. The current production version of AM2 is Mod 5.

AM2 panels are 2 ft by 12 ft by 1.5 in. and fabricated from a single 6061-T6 aluminum alloy extrusion with end connectors welded to the 2-ft ends to form a complete panel. The core of the extruded panels is composed of vertical stiffeners spaced 1.75 in. apart in the 12-ft direction. The mat is also made in half-panels to allow a staggered brickwork configuration. The panels were joined along the two 12-ft edges by a hinge-type male/female connection. The adjacent 2-ft ends were joined by an overlap/underlap connection secured by an aluminum locking bar. The panels were coated with a nonskid material to increase the surface friction. Pertinent properties of AM2 mat are shown in Table 2.1. All AM2 mat used for testing was obtained from NAVAIR. The AM2 panels were delivered in F71 and F72 packages. Photographs of the AM2 F71 and F72 packages similar to those used in this test are shown in Figure 2.1. Drawings of the connections are shown in Figure 2.2.

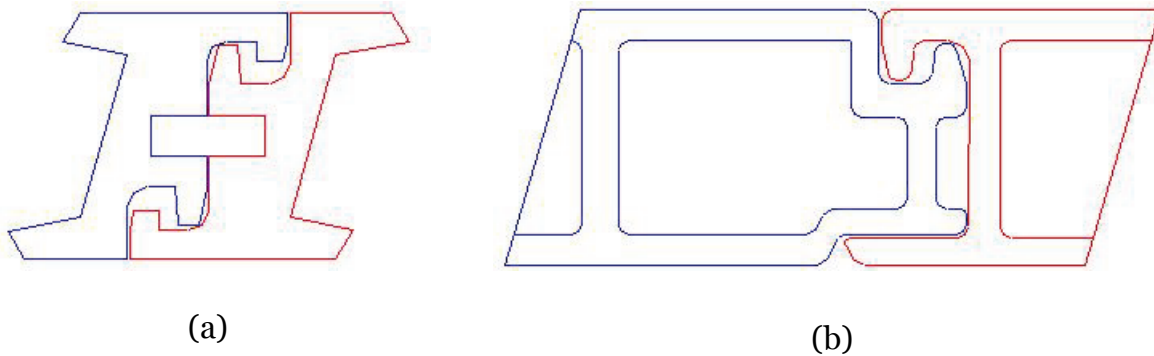
Table 2.1. AM2 mat properties.

	Full-panel	Half-panel
Length (ft)	12.0	6.0
Width (ft)	2.0	2.0
Thickness (in.)	1.5	1.5
Panel Weight (lbf)	145.5	74.4
Unit Weight (lbf/ft ²)	6.1	6.3

Figure 2.1. F71 (left) and F72 (right) mat packages.



Figure 2.2. AM2 (a) overlap/underlap and (b) male/female hinge connections.



2.2 High-plasticity clay (CH) subgrade

The CH material used for subgrade construction was procured from a local source in Vicksburg, MS, and was subjected to laboratory tests listed in Table 2.2. Classification data for the subgrade soil are shown in Figure 2.3. Moisture-density and CBR-moisture content relationships are shown in Figures 2.4 and 2.5, respectively. These data were used to determine the target moisture content and dry density required to obtain the target CBR of 6. As shown in Figure 2.5, the target moisture content was 34 percent to achieve a CBR of 6. The expected dry density for quality control at 34 percent moisture content was 85 lb/ft³.

Table 2.2. Laboratory tests for Vicksburg Buckshot CH.

Test Name	ASTM
Standard Practice for Classification of Soils for Engineering Purposes (USCS)	D2487
Standard Test Method for Particle Size Analysis of Soils	D422
Standard Test Method for Laboratory Compaction Characteristics of Soil Using Modified Effort	D1557
Standard Test Method for CBR of Laboratory Compacted Soils	D1883
Standard Test Methods for Liquid Limit, Plastic Limit, and Plasticity Index of Soils	D4318

Figure 2.3. Gradation curve for Vicksburg Buckshot CH.

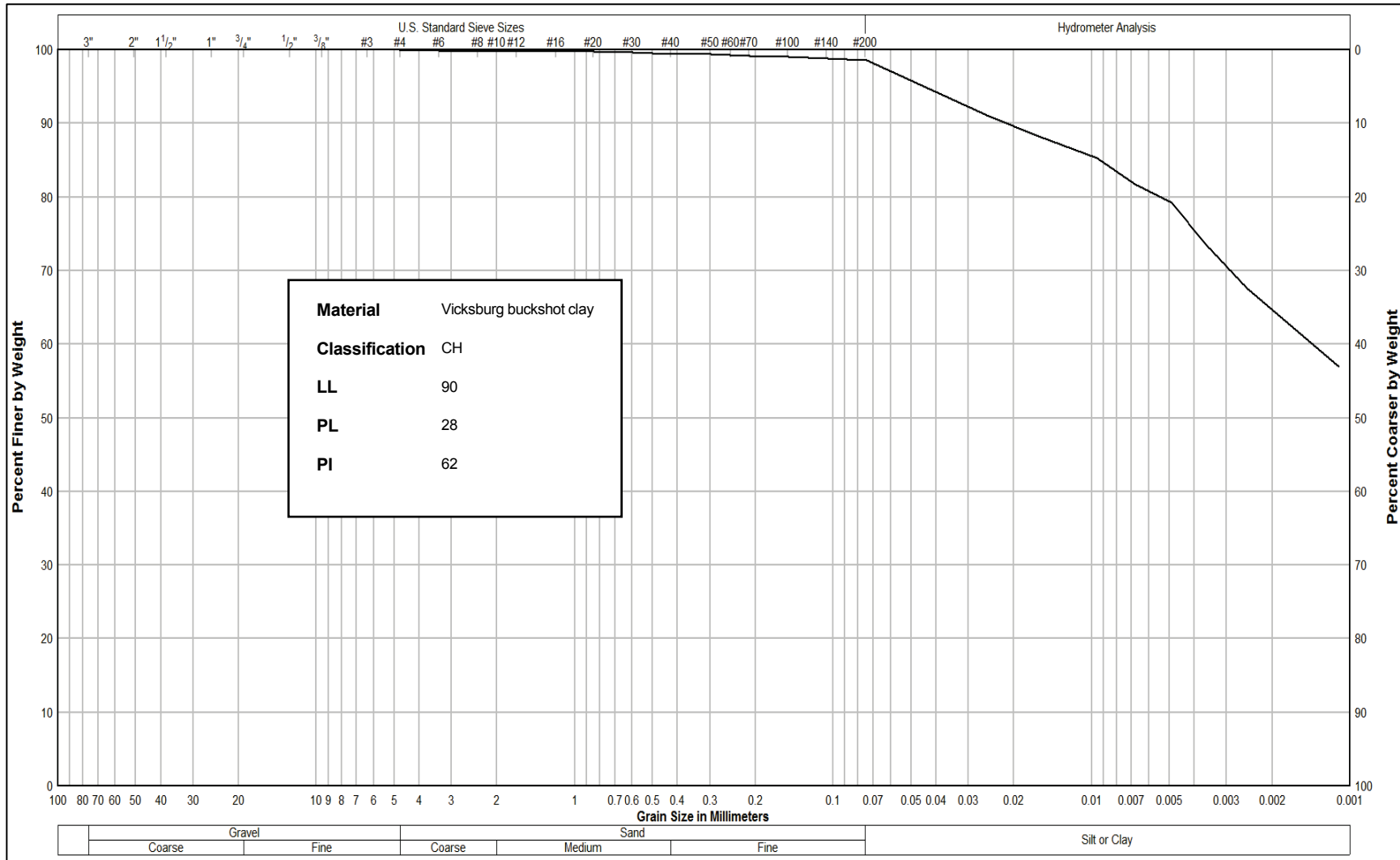


Figure 2.4. Dry density vs. moisture content for CH subgrade material.

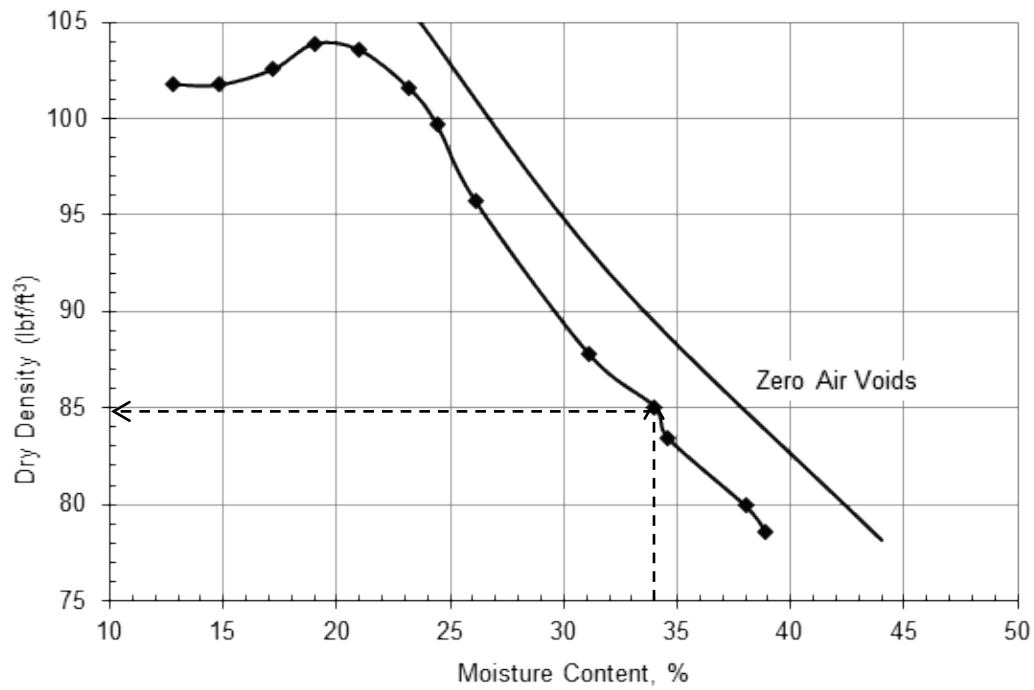
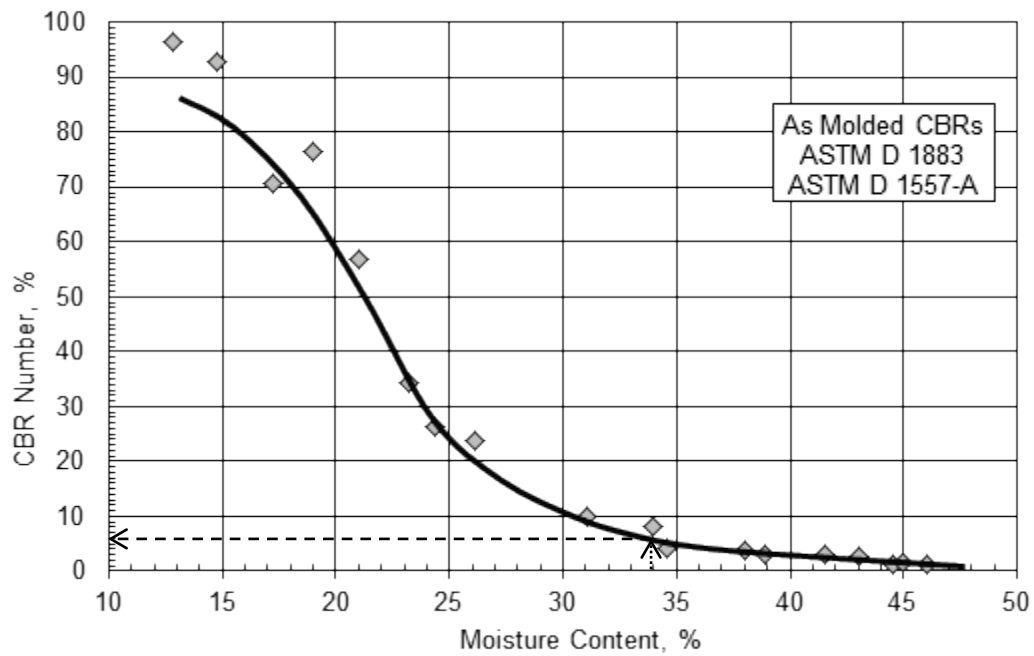


Figure 2.5. CBR vs. moisture content for CH subgrade material.

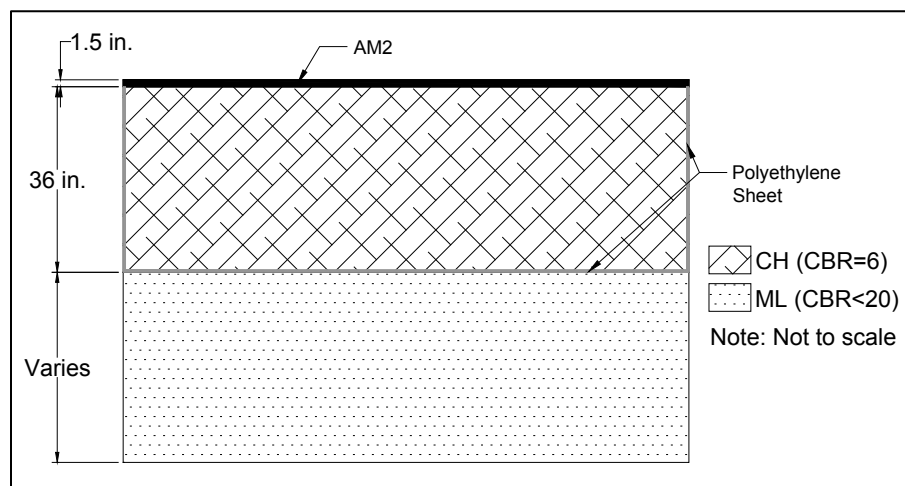


3 Experimental Program

3.1 Test section general description

The tests were conducted on full-scale test sections constructed and trafficked under shelter in the Hangar 4 pavement test facility at the U.S. Army Engineer Research and Development Center (ERDC). AM2 mat panels were placed directly over a 36-in.-thick CH subgrade prepared to a CBR of 6 over an existing silt foundation, as shown in Figure 3.1.

Figure 3.1. Test section profile.



General layouts of each test section, along with panel designations, are shown in Figures 3.2 and 3.3. Each panel was identified with a number to track damage during trafficking. Each test consisted of a 66-ft-wide by 42-ft-long section of matting. For the brickwork pattern test on a voided subgrade, voids were prepared on the subgrade surface (approximately 30 ft from the west edge of the test section) before placing AM2 mat. Void locations and descriptions are provided in Figure 3.2 and Table 3.1. An area centered 30 ft from the west edge of the test section had a 3.75-ft-wide lane designated for simulated F-15E traffic in a normally distributed wander pattern. Traffic was applied bidirectionally.

The second brickwork pattern test section consisted of two test items (Figure 3.3). An area centered 18 ft from the west edge of the test section had a 3.75-ft-wide lane designated for simulated F-15E traffic, and an area centered 18 ft from the east edge had a 9-ft-wide lane designated for simulated C-17 traffic. Lanes for the F-15E and C-17 items were trafficked according to normally distributed wander patterns associated with the

F-15E and C-17 aircrafts, which are described later in this chapter. As shown in Table 1.3 and throughout this report, the brickwork test item on the voided subgrade will be called “F-15E-V.” The two test items on the second brickwork test section will be called “F-15E” and “C-17.”

Figure 3.2. AM2 brickwork pattern on voided subgrade panel layout.

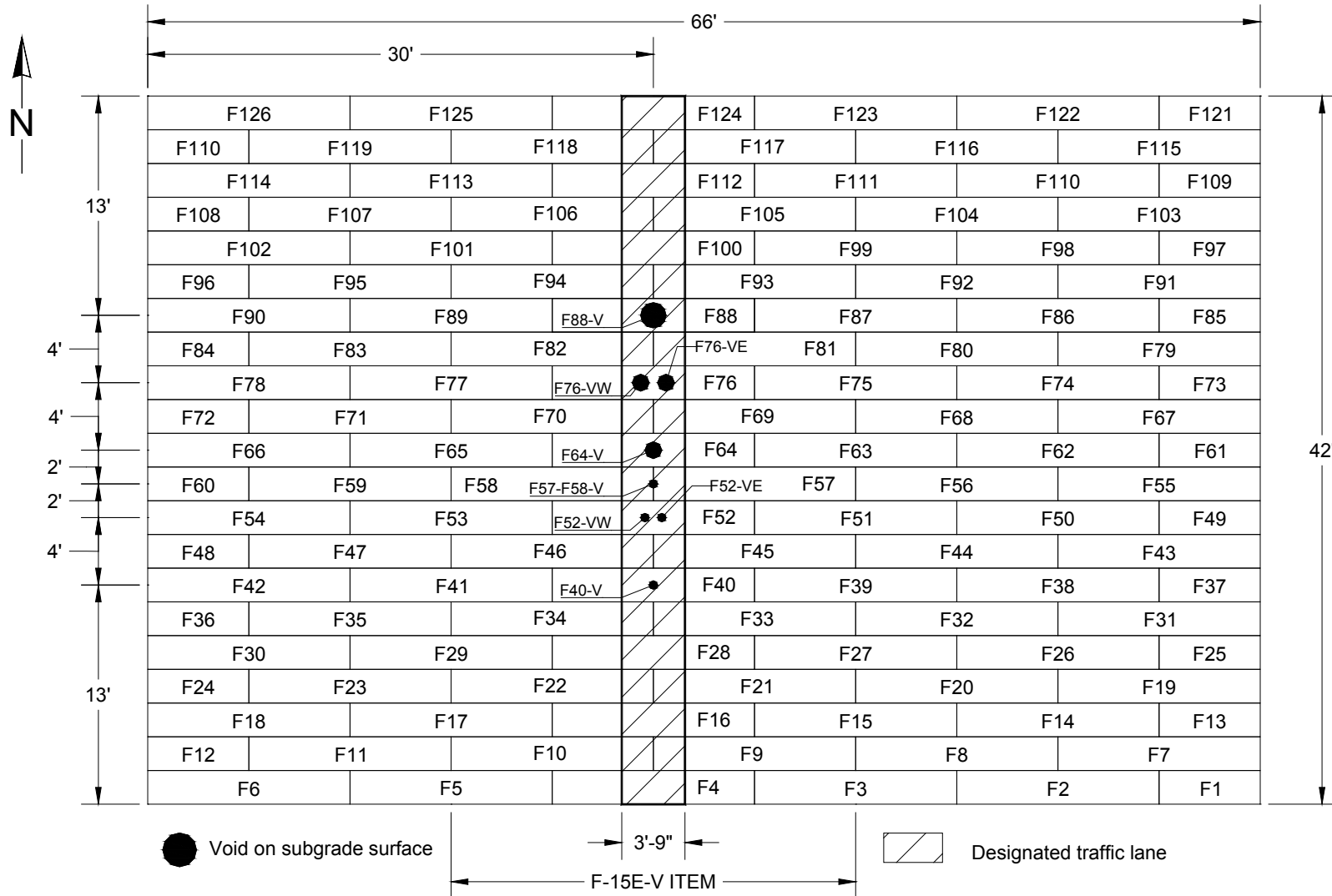


Figure 3.3. AM2 brickwork pattern panel layout.

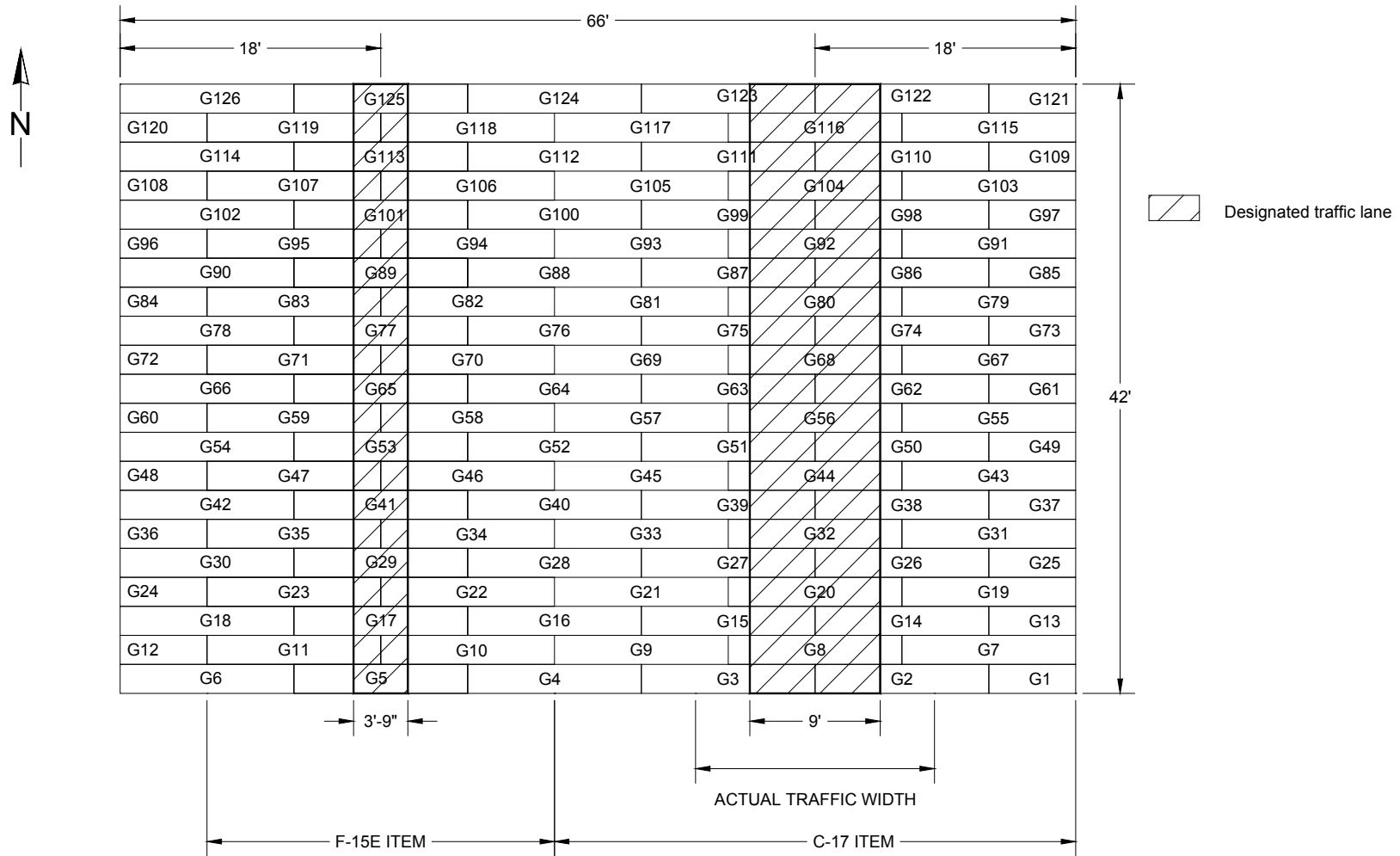


Table 3.1. Void locations and descriptions.

Void Designation	Diameter (in.)	Location
F40-V	6	Center of Panel F40
F52-VE	6	6 in. offset east from center of Panel F52
F52-VW	6	6 in. offset west from center of Panel F52
F57-F58-V ^a	6	Center of joint between Panels F57 and F58
F64-V	12	Center of Panel F64
F76-VE	12	9 in. offset east from center of Panel F76
F76-VW	12	9 in. offset west from center of Panel F76
F88-V	18	Center of Panel F88

^aNot monitored during traffic;

Note: all voids 2 in. deep

3.2 Test section construction

The following sections describe the construction of the foundation subgrade and the AM2 mat installation. Field and laboratory soil testing data used to determine the moisture, density, and bearing capacity in terms of CBR are also included.

3.2.1 Subgrade construction and posttest forensics

The test section subgrade was built using in-place material from a previous AM2 test section constructed to a CBR of 6. The original subgrade was constructed by excavating a 60-ft-wide by 40-ft-long test pit to a minimum 36-in. depth below the existing finished grade in Hangar 4, as shown in Figure 3.4. The soil at the bottom of the excavation was a silt material (ML) having a CBR less than 20. The existing ML material was leveled with a bulldozer and compacted with a pneumatic roller and a vibratory steel-wheel compactor to ensure that the remainder of the test section was constructed over a stable foundation. The bottom and sides of the test pit were lined with impervious 6-mil polyethylene sheeting to minimize moisture migration from the 36 in. of new CH soil serving as the test section subgrade, as shown in Figure 3.4.

Figure 3.4. Test section excavation (left) lined with impervious sheeting (right).



The CH material was processed at a nearby preparatory site by spreading the material to a uniform 12-in. depth, pulverizing the material with a rotary mixer, adjusting the moisture content, pulverizing the material again, and stockpiling (Figure 3.5). This was an iterative process necessary to achieve a uniform distribution of moisture throughout the material. Once the CH had been processed to the target moisture content, it was placed in the test section, spread by a bulldozer in 8-in. lifts, and compacted with a pneumatic roller to a depth of 6 in. (Figure 3.6).

Figure 3.5. Pulverizing CH (left) and adding moisture (right).



Each compacted lift was subjected to the test methods listed in Table 3.2 at stations 10 and 30 along the centerline of each test item to verify that target values had been met (Figure 3.7). If the average pretest CBR of a lift differed from the target value by more than +1.0 or -0.5 CBR, the lift was reconstituted. Each lift was surveyed to obtain an average thickness. After data collection, the surface was scarified an average depth of 1 in. with a rotary mixer prior to placement of the following lift to facilitate bonding at the interface.

Figure 3.6. Leveling (left) and compacting (right) CH.



Table 3.2. Field tests on each constructed lift.

Test Name	Test Designation	Pre-test	Post-test
Standard test method for in-place density and water content of soil and soil aggregate by nuclear methods (shallow depth)	ASTM D6938	X	X
Standard Test Method for Laboratory Determination of Water Content of Soil and Rock Mass	ASTM D2216	X	X
Standard Test Method for Use of the Dynamic Cone Penetrometer in Shallow Pavement Applications ^a	ASTM D6951	X	X
Standard Test Method for Determining the California Bearing Ratio of Soils	CRD-C654-95	X	X

^aConducted after last lift was compacted.

Figure 3.7. Nuclear gage (left) and CBR test (right).



For the evaluation discussed in this report, the upper 6 to 8 in. (approximately 1 lift) of the existing test bed were removed and replaced with newly processed material. Posttest values from the previous evaluation 6 in. below the surface of the subgrade showed that the material retained its moisture and a CBR of approximately 6. It was assumed that the remainder of the subgrade depth retained its pretest values. Therefore, reconstruction of the entire depth was unnecessary. The newly processed material was replaced in one 6-in. lift. The methods listed in Table 3.2

were performed at stations 10 and 30 along the centerline of each test item to ensure the target values were achieved.

Once trafficking was completed, posttest forensics were conducted at the same locations to determine the depth of subgrade that might have undergone gradual drying and possible densification under traffic. Some increase in CBR was expected because of thixotropic properties of clay structures and gradual drying and densification during trafficking. Based on historic testing data, surface increases of less than 5 CBR and increases of less than 3 CBR at a depth of 6 in. are common and therefore acceptable (Rushing and Tingle 2007; Rushing and Torres 2007; Rushing et al. 2011; Garcia et al. 2012; Rushing et al. 2012).

For the F-15E-V item, the posttest CBR increased to 11.3 for the top 6 in. at the three stations. The posttest CBR increased by 5.0 from the pretest value of 6.3. For the F-15E test item, the posttest CBR measurements at the surface increased from 5.8 to 10.4 during trafficking. For the C-17 test item, the posttest CBR measurements at the surface increased from 5.9 to 8.8. Additional measurements beneath the surface showed minor increases in the strength. Since these measurements were within historic ranges, the strength of the subgrade remained within acceptable limits throughout testing.

Subgrade properties prior to installing mat and after completing traffic on each test item are shown in Table 3.3. The pretest moisture content and density measurements generally follow the trends found in laboratory measurements presented in Figures 2.4 and 2.5. However, previous experience has shown that the field moisture content required to construct a CBR of 6 typically ranges from 30 to 32 percent instead of 34 percent as suggested in Figure 2.5. This is due to the compaction energy in the field exceeding the laboratory standard compaction energy.

3.2.2 AM2 strain gauge instrumentation

Prior to installation, several mat panels were instrumented with foil strain gauges on the upper underlap or lower overlap regions of the 2-ft end connectors as shown in Figures 3.8 and 3.9. The gauges were installed by the Applied Research Laboratory (ARL) at Pennsylvania State University (PSU) under a contract with NAVAIR. The mats with gages installed were delivered to ERDC for this evaluation. The locations of panels with gages in the test array are shown in Figure 3.10 for the F-15E-V item and in

Figure 3.11 for the F-15E and C-17 items. The number and location of gauges installed on each panel are detailed in Table 3.4.

Table 3.3. Average in situ properties of the subgrade in each test item.

Test Depth	Nuclear gauge test			CBR Test		
	Wet Density (lb/ft ³)	Dry Density (lb/ft ³)	Moisture (%)	Oven Moisture (%)	In Situ CBR (%)	Δ CBR (%)
F-15E-V ITEM						
PRETEST						
Surface‡	118.6	88.3	34.3	29.4	6.3	-
6 in. ^a	115.6	85.8	34.7	33.1	6.8	-
12 in. ^b	117.4	90.5	29.8	30.7	6.0	-
18 in. ^b	117.6	90.7	29.6	31.1	6.0	-
24 in. ^b	115.7	88.0	31.4	27.4	5.8	-
30 in. ^b	116.3	87.8	32.3	32.9	6.1	-
POSTTEST						
Surface	119.8	92.8	28.0	-	11.3	5.0
F-15E ITEM						
PRETEST						
Surface‡	116.5	88.1	32.3	31.9	5.8	-
6 in.	118.8 ^b	92.2 ^b	28.8 ^b	30.2 ^a	6.4 ^a	-
12 in. ^b	118.8	92.3	28.7	29.1	6.2	-
18 in. ^b	118.1	91.4	29.3	31.3	6.1	-
24 in. ^b	116.3	87.6	32.7	27.2	5.7	-
30 in. ^b	117.4	88.9	32.0	32.5	6.2	-
POSTTEST						
Surface	119.2	88.9	34.2	29.5	10.4	4.6
6 in.	119.4	88.9	34.6	31.6	7.4	1.0
12 in.	119.6	89.7	33.7	31.7	7.3	1.1
18 in.	120.7	92.9	30.0	31.9	8.1	2.0
24 in.	119.5	90.6	32.0	32.8	8.6	2.9
C-17 ITEM						
PRETEST						
Surface ^c	118.0	89.5	31.8	32.4	5.9	-
6 in.	118.9 ^b	92.1 ^b	29.1 ^b	32.9 ^a	6.5 ^a	-
12 in. ^b	116.1	88.7	30.8	32.2	5.8	-
18 in. ^b	117.1	90.1	29.9	30.8	6.0	-
24 in. ^b	115.1	88.5	30.2	27.5	5.9	-
30 in. ^b	115.2	86.8	32.7	33.2	6.1	-
POSTTEST						
Surface	119.2	87.7	35.9	27.5	8.8	3.0
6 in.	119.8	91.9	30.6	35.4	6.6	0.1
12 in.	119.2	90.6	31.6	28.6	8.1	2.3
18 in.	116.2	89.8	33.1	29.4	7.7	1.7
24 in.	116.0	85.6	35.4	30.1	7.5	1.6

^a Newly measured data.

^b Average values from original construction.

^c New lift.

Figure 3.8. Strain gauge locations on upper underlap and lower overlap regions.

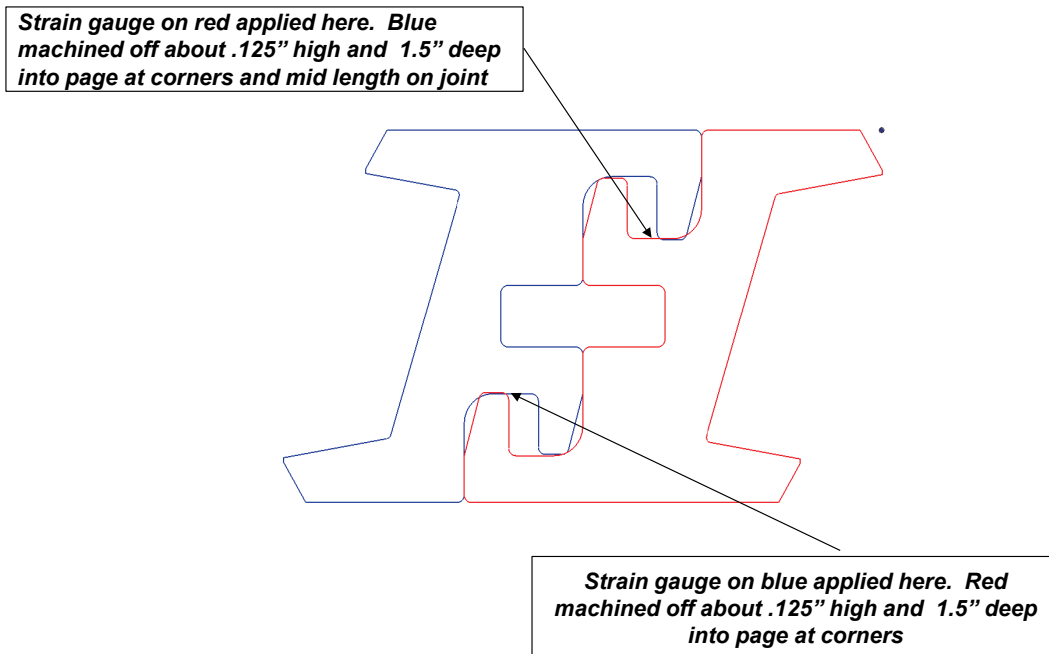
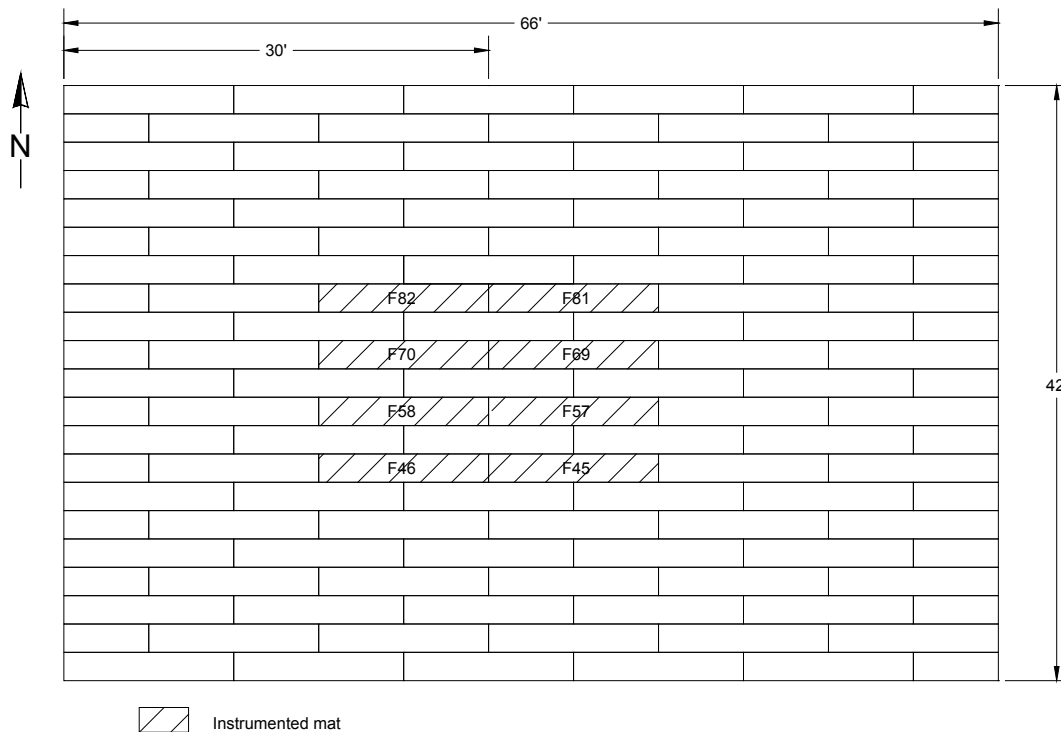


Figure 3.9. Typical strain gauge installation on lower overlap region.



Figure 3.10. F-15E-V item instrumentation layout.



The strain gauges were used to gather critical strain information. The DIM showed the installation regions on the prongs to be the component most susceptible to breaking. These regions have also been shown to be the predominant failure regions in full-scale tests of AM2 reported by Rushing and Tingle (2007), Rushing and Torres (2007), Rushing et al. (2008), Rushing and Mason (2008), Garcia and Rushing (2013), and Rushing et al. (2014). The gauged end connectors were placed along the centerline of each item to measure the maximum strains induced under simulated aircraft traffic loads.

Figure 3.11. F-15E and C-17 items instrumentation layout.

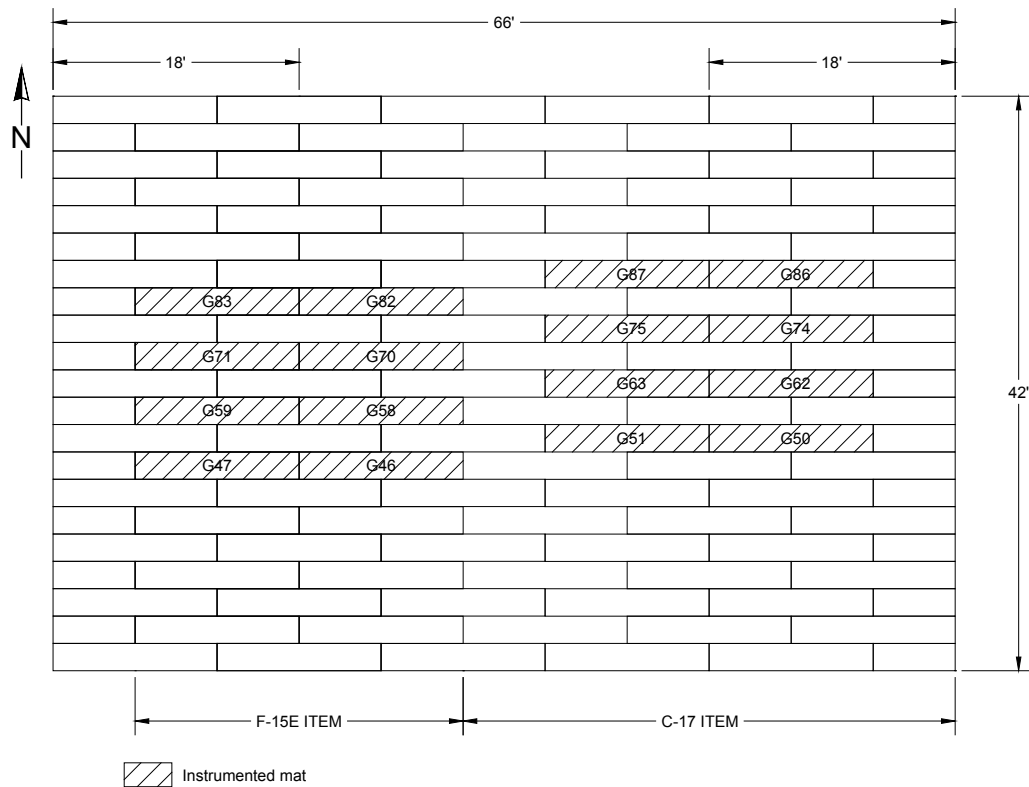


Table 3.4. Strain gauges in each test item.

Test Item	Panel Number (gauge count)	
	12-ft Panel Lower Overlap	12-ft Panel Upper Underlap
F-15E-V	F46 (2)	F45 (2)
	F58 (2)	F57 (2)
	F70 (2)	F69 (2)
	F82 (2)	F81 (2)
F-15E	G47 (2)	G46 (2)
	G59 (3)	G58 (3)
	G71 (3)	G70 (3)
	G83 (2)	G82 (2)
C-17	G51 (2)	G50 (2)
	G63 (3)	G62 (3)
	G75 (3)	G74 (3)
	G87 (2)	G86 (2)

3.2.3 AM2 mat installation

Prior to installation of AM2 on the subgrade surface, 2-in.-deep voids were excavated on the surface at the locations shown in Figure 3.2 and to the diameters listed in Table 3.1. Photographs of the process are shown in Figure 3.12. The AM2 airfield mat system was placed on the surface of the prepared test section subgrade by an experienced crew. The mat bundles were placed on the test section with a forklift, and the individual panels were carried by two men and placed into position.

Figure 3.12. Void installation on subgrade surface.



The first mat panel was placed flat on the ground with the long dimensions perpendicular to the direction of traffic and with the male hinge connector facing north. The second panel was positioned adjacent to the 2-ft end of the first, allowing the overlapping end connector of the second panel to drop into position over the underlapping end connector of the first panel. A rectangular slot was formed between the two end connector rails, and an aluminum locking bar was inserted into the slot, as shown in Figure 3.13. This locking bar prevented the ends of the mat panels from separating. This process was continued until the first row was installed.

For the second row, the 12-ft female hinge connector was attached to the male hinge connector of panels from the first row, and the panel was pivoted into place, as shown in Figure 3.14. The next panel was installed by attaching the female hinge connector to the male hinge connector of panels in the first row and allowing the overlapping end connector rail to pivot over and connect to the underlapping end connector rail of the adjacent panel. An aluminum locking bar was inserted into the space provided to keep the panels from separating. This process was repeated until the entire mat test section was assembled in a brickwork configuration with half-panels on alternating ends of every other row.

Figure 3.13 Insertion of aluminum locking bar between adjacent panels.



Figure 3.14. Installation of AM2 panels on the test section subgrade.



Once assembly was complete, full-panels of AM2 were installed along the ends of the traffic lanes to facilitate the entrance and exit of the test vehicles. Male keylocks were attached to the female hinge connector of the

panels in the first row to facilitate ramp installation, as shown in Figure 3.15. A photograph of the assembled F-15E-V test item is shown in Figure 3.16. Once the mats had been installed, 1,000-lb steel weights were placed along the edges of the test section to anchor the mats and simulate the resistance to movement provided by a large expanse of matting.

After completing the F-15E-V item test, the panels were removed and replaced with panels for the F-15E and C-17 items. Entrance/exit ramps and steel weights were placed in the same manner. General views of each item in the second brickwork test section are shown in Figure 3.17.

Figure 3.15. Typical Installation of male keylock.



Figure 3.16. F-15E-V item.



Figure 3.17. F-15E (left) and C-17 (right) items.



3.3 Traffic application

This section describes the application of simulated aircraft traffic on the AM2 airfield mat system. Pertinent data concerning the test load carts are provided.

3.3.1 F-15E load cart

A specially designed single-wheel load cart was used to simulate F-15E aircraft traffic. The load cart was equipped with a 36-in. by 11-in., 30-ply tire inflated to 325 lbf/in.² and loaded such that the test wheel was supporting 35,235 lb. The F-15E load cart was equipped with an outrigger wheel to prevent overturning and was powered by the prime mover of a Case vibratory steel-wheel roller as shown in Figure 3.18.

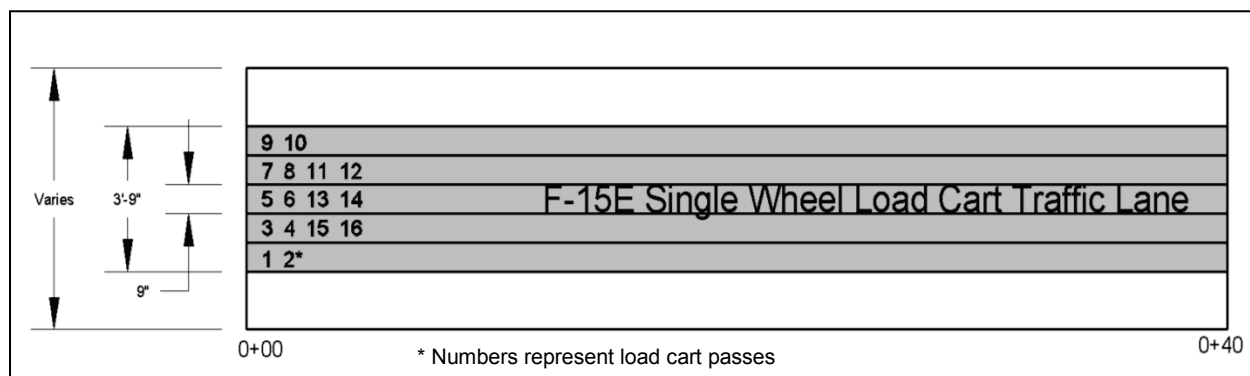
Figure 3.18. F-15E test load cart.



A normally distributed pattern of simulated traffic was applied in a 3.75-ft-wide traffic area for the F-15E test item, as shown in Figure 3.19. The traffic area was divided into five lanes that were designed to simulate the traffic distribution pattern, or wander width, of the main landing gear wheel on a mat surface when taxiing to and from an active runway. The width of each lane corresponded to the measured contact width, 9 in., of the F-15E tire when fully loaded and not the overall published tire width of 11 in. The normally distributed traffic patterns were simplified for ease-of-use by the load cart operator. Traffic was applied by driving the load cart forward and then backward over the length of the test item and then shifting the path of the load cart laterally approximately one tire width on each forward path. Odd numbered load cart passes traveled north (forward pass) and even numbered passes traveled south (backward pass).

This procedure was continued until one pattern of traffic was completed. One pattern resulted in 16 passes, or 4 coverages.

Figure 3.19. Plan view showing F-15E normally distributed traffic lanes.



3.3.2 C-17 load cart

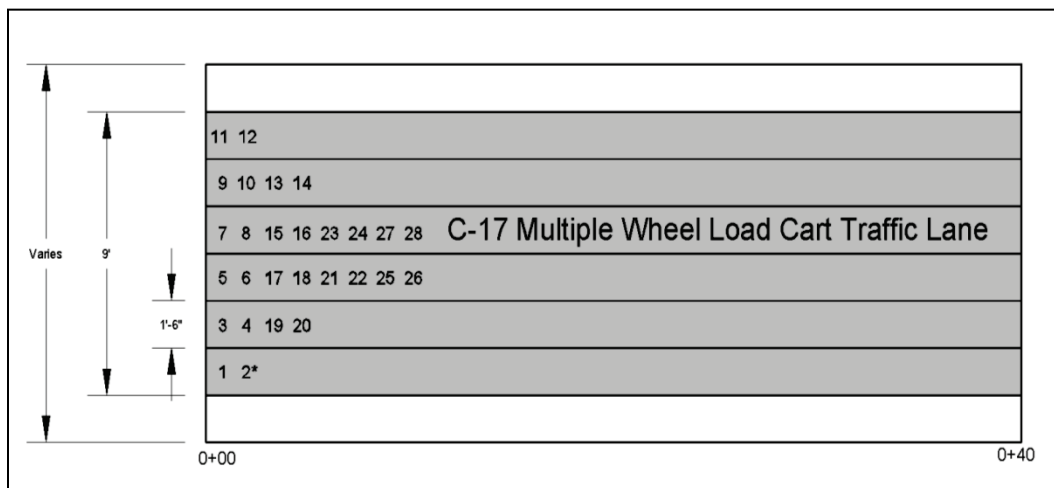
The multiple-wheel C-17 load cart was designed to exactly match one full main gear of a C-17 aircraft. The multiple-wheel C-17 load cart was equipped with six 50-in. by 21-in., 20-ply tires inflated to 142 lbf/in.² and loaded such that the test gear was supporting 269,560 lb, with estimated individual wheel loads of 44,930 lb. The test cart was powered by the front half of a Fiat scraper as shown in Figure 3.20.

A simulated normally distributed traffic pattern was applied in a 9-ft-wide traffic area for the C-17 test item, as shown in Figure 3.21. The traffic areas were divided into individual lanes designed to simulate the traffic distribution pattern, or wander width, of the main landing gear wheels on a mat surface when taxiing to and from an active runway. The width of each lane corresponded to the measured contact width, 18 in., of the C-17 tires when fully loaded and not the overall published tire width of 21 in. The normally distributed traffic patterns were simplified for ease-of-use by the load cart operator. Traffic was applied by driving the load cart forward and then backward over the length of the C-17 test item and then shifting the path of the load cart laterally approximately one tire width on each forward pass. Odd numbered load cart passes traveled north (forward pass) and even numbered passes traveled south (backward pass). Tracking guides were attached to assist the driver in shifting the load cart the proper amount for each forward pass. This procedure was continued until one pattern of traffic was completed. For the C-17 test item, one pattern resulted in 28 passes, or 25 coverages.

Figure 3.20. C-17 test load cart.



Figure 3.21. Plan view showing C-17 normally distributed traffic lanes.



3.4 Data collection

Data collection included:

- robotic total station measurements of centerline profiles, cross sections, and dynamic elastic deflections
- dynamic strain measurements, and
- borescope observation videos.

Data collection intervals for F-15E and C-17 traffic are shown in Tables 3.5 and 3.6, respectively. Data collection layouts are shown in Figures 3.22 and 3.23. For the F-15E-V item, voids on the subgrade surface were measured before mat installation to verify they were excavated to the correct dimensions and depth and inspected after traffic was concluded to determine the extent of movement of the material. The mat surface was inspected for damage periodically during traffic.

3.4.1 Centerline profile

Data collected on the pretest subgrade, on the mat surface at scheduled pass levels, and the posttest subgrade after removing the mat along the traffic centerline are labeled “centerline profiles” in this report. For the F-15E and C-17 items, robotic total station elevation data were collected at 1-ft intervals on both the subgrade and mat surface. Data were collected at 6-in. intervals for the F-15E-V item.

3.4.2 Unloaded cross sections

Data collected transverse to the direction of traffic on the pretest subgrade, on the mat at scheduled pass levels and the posttest subgrade after removing the mat at the locations labeled A1, A2, and A3, are called “cross sections” in this report. The locations of perpendicular lines A1, A2, and A3 were selected near the quarter-points of the test items to characterize the average performance while avoiding potential end effects associated with boundary conditions at the ends of the test sections. Robotic total station elevation data were collected at 1-ft intervals from 2-ft to 10-ft offset from the centerline and at 6-in. intervals up to 2-ft offset from the centerline for the F-15E and F-15E-V items. For the C-17 item, data were recorded at 1-ft intervals from 8-ft to 18-ft offset from the centerline and at 6-in. intervals up to 8-ft offset from the centerline. A typical survey of an unloaded cross section is shown in Figure 3.24.

3.4.3 Loaded cross sections

In an attempt to measure the permanent deformation of the subgrade underneath the mat surface, a forklift carrying two 2,000-lb lead weights was parked on the mat surface adjacent to each cross section, and elevation data were once again recorded at the same intervals (Figure 3.24). The wheel load applied was approximately 6,000 lb. These data are noted as “loaded cross sections” in this report. The goal of the load application

was to deflect the mat enough to contact the subgrade but not so much as to induce elastic deflections in the subgrade.

Table 3.5. Data collection intervals for F-15E traffic.

F-15E-V Item Total Passes	F-15E Item Total Passes	Centerline Profile	Unloaded Cross sections	Loaded Cross sections	Dynamic Deflection	Strain Gauges ^a	Void Depths
Pretest Subgrade	Pretest Subgrade	X	X				
0	0	X	X	X	X	X	X
10	10	X	X	X	X	X	X
16	16	X	X	X	X	X	X
32	32	X	X	X	X	X	X
48	48	X	X	X	X	X	X
112	112	X	X	X	X	X	X
240	240	X	X	X	X	X	X
496	476	X	X	X	X	X	X
1008	-	X	X	X	X	X	X
Posttest Subgrade	Posttest Subgrade	X	X				

^a Data were collected continuously.

Table 3.6. Data collection intervals for C-17 traffic.

Total Passes	Centerline Profile	Unloaded Cross Sections	Loaded Cross Sections	Dynamic Deflection	Strain Gauges ^a
Pretest Subgrade	X	X			
0	X	X	X	X	X
12	X	X	X	X	X
28	X	X	X	X	X
56	X	X	X	X	X
84	X	X	X	X	X
168	X	X	X	X	X
308	X	X	X	X	X
Post-test Subgrade	X	X			

^aData were collected continuously.

Figure 3.22. Data collection layout for F-15E-V item.

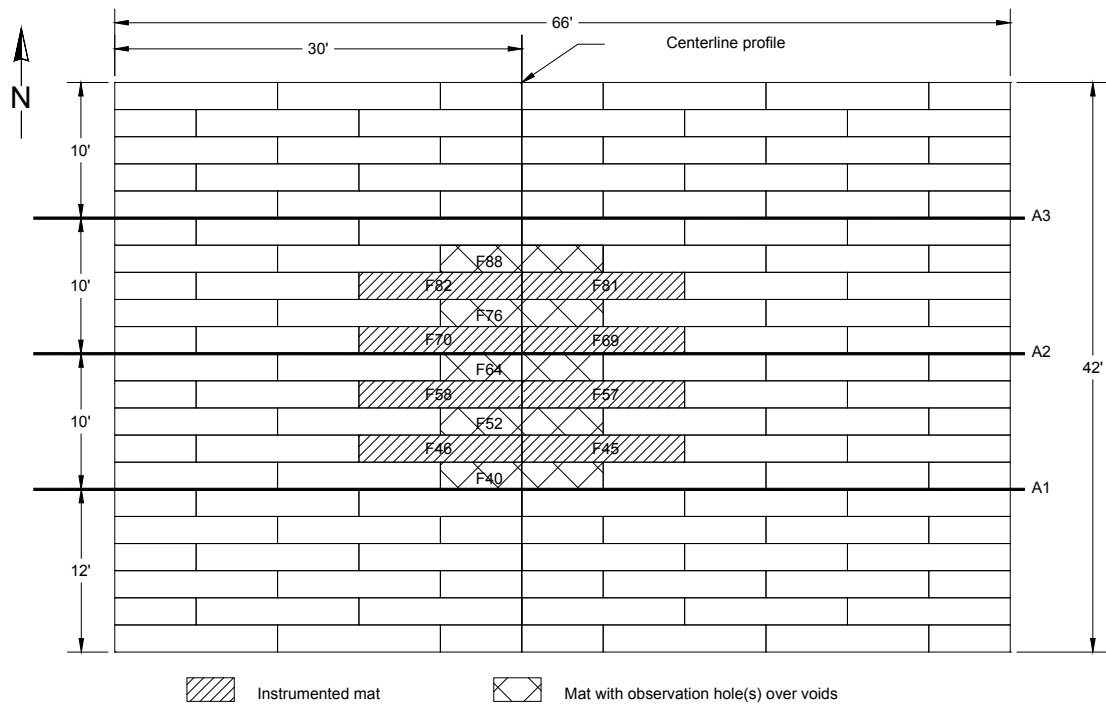
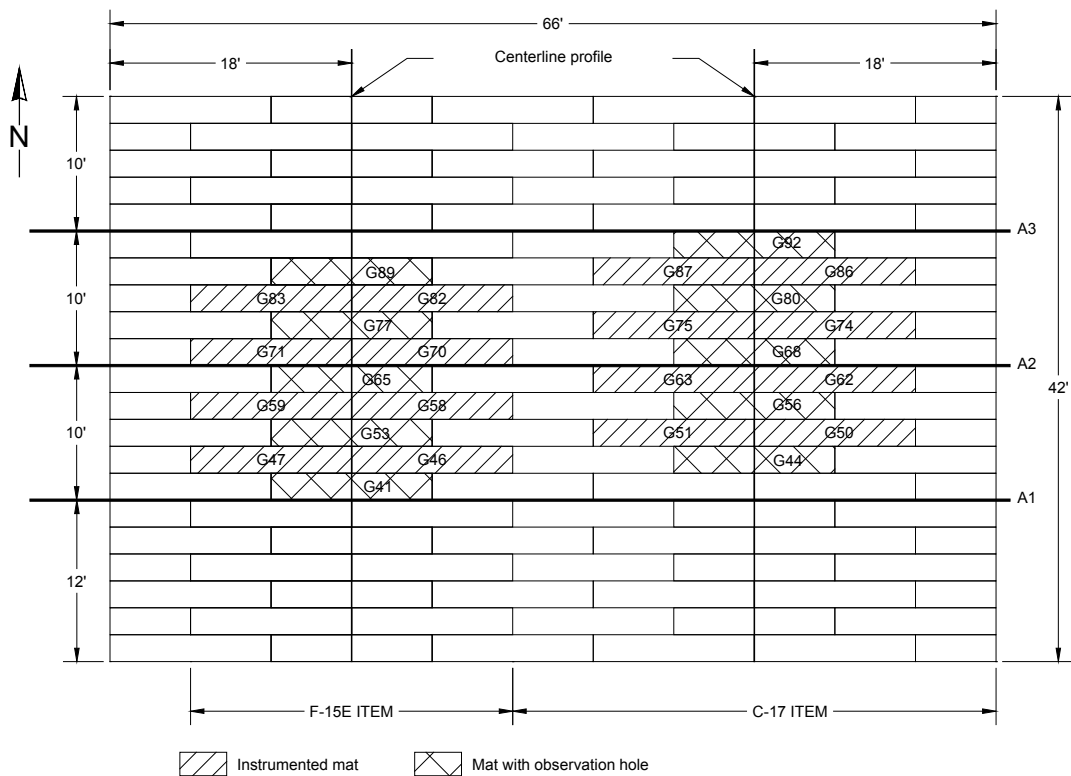


Figure 3.23. Data collection layout for F-15E and C-17 items.



3.4.4 Dynamic deflection

Elevation data were collected dynamically on the F-15E and F-15E-V items by mounting a survey prism just above the load wheel on the F-15E load cart, as shown in Figure 3.25, during the first 16 passes of each data collection interval (or all passes during an interval that was less than 16 passes). The robotic total station recorded elevation measurements for every 6 in. of forward or backward movement of the load cart. The data were referenced to unloaded data collected along the centerline of the mat surface to calculate elastic deflection, as explained later in this report. Elastic deflection was not measured on the C-17 item because of the inability to mount a survey prism in an acceptable location on the load cart and other safety concerns.

Figure 3.24. Surveying unloaded (left) and loaded (right) cross section.



3.4.5 Strain measurements

National Instruments NI SCXI data acquisition hardware was used to collect data points at a rate of 100 Hz. Strain data were collected continuously and data recording was only paused at the pass levels shown in Tables 3.5 and 3.6, and when traffic needed to be stopped temporarily for inspection of the mat surface.

3.4.6 Borescope observation and void depth measurement

For the F-15E-V item, holes were drilled to take borescope video directly above each of the voids. Videos of the borescope observations have been retained for archiving. In addition, a depth gage was inserted through each hole to measure the distance from the surface of the mat to the surface of the subgrade. By subtracting the thickness of the mat, the distance between the bottom surface of the mat and the surface of the subgrade

could be determined (Figure 3.26). Depth measurements for the F-15E and C-17 items are not reported in this document. Depth measurements are reported for the F-15E-V item in terms of void designation.

Figure 3.25. Prism mounted on F-15E load cart.

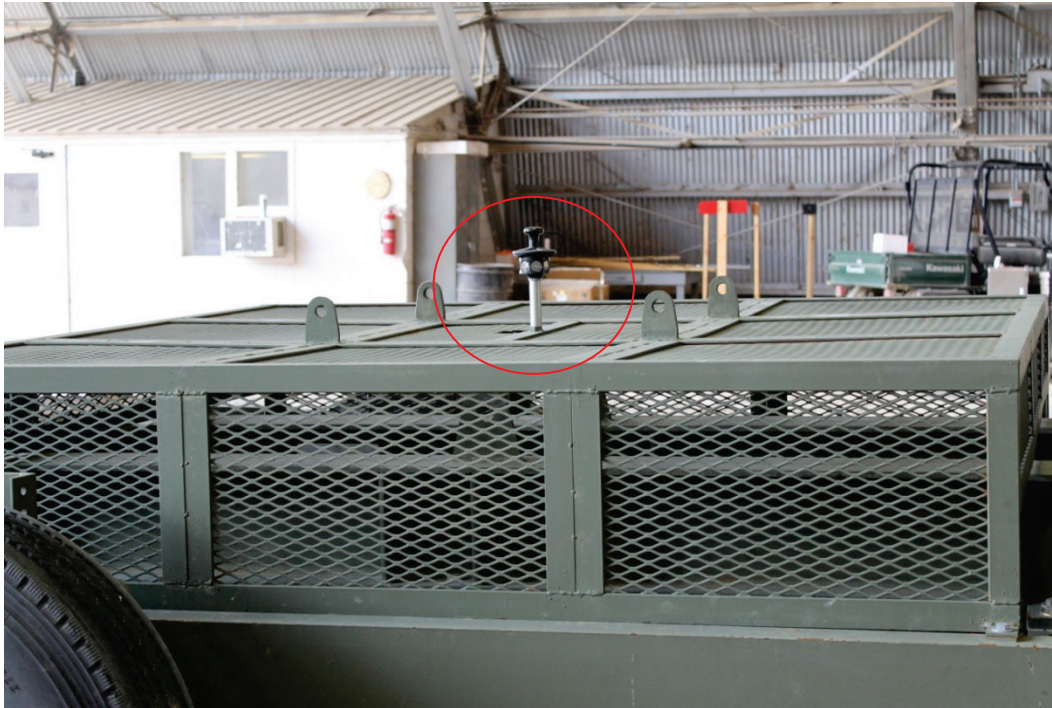
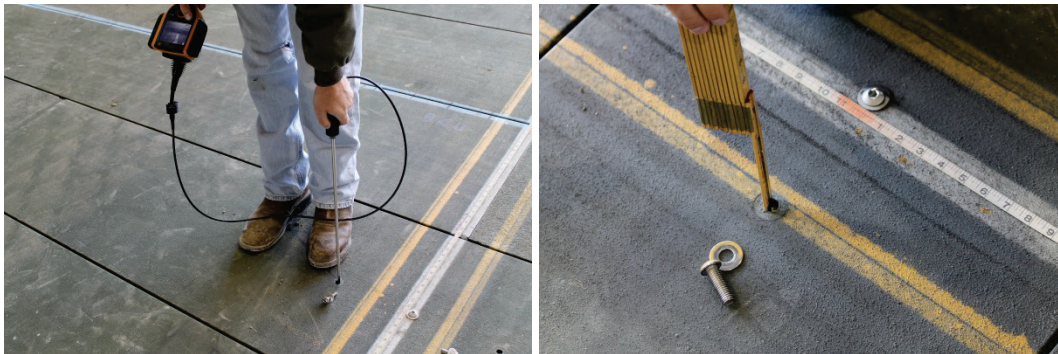


Figure 3.26. Borescope (left) and void depth measurement (right).



3.5 Failure criteria

The failure criteria established were either (1) 10 percent mat breakage or (2) the development of 1.25 in. of permanent surface deformation for the F-15E or 3.0 in. of permanent surface deformation for the C-17. These failure criteria were developed based on previous testing of airfield matting and USAF requirements. Failure criteria values were recorded and monitored for compliance.

3.5.1 Mat breakage criteria

Mat breakage percentages were calculated by dividing the area of the failed panel by the total area influenced by the simulated traffic application in the assembled test item. For example, the total area influenced by the F-15E item was 1008 ft² (24 ft by 42 ft). Ten percent of this area is 100.8 ft², which is equal to the area of 4.2 12-ft panels (5 full-panels). Individual panels were considered failed if observed damage posed a significant tire hazard or caused instability of the load cart. Tire hazards were defined as damage that could not be reasonably maintained by simple field maintenance procedures. A typical example was a top skin tear in excess of 10 to 12 in., representing significant structural damage to the surface skin with sharp edges that may endanger an aircraft tire.

3.5.2 Permanent deformation criteria

The permanent surface deformation limits of 1.25 in. and 3.0 in. are based on roughness limitations for the F-15E and C-17 aircrafts, respectively. An abrupt change in elevation or the development of a rut in the wheel path greater than the allowable values may exceed aircraft roughness limits. The rut depth limit is required since many connecting taxiways and aprons intersect at 90 deg, and crossing perpendicular to a pre-formed rut may cause an abrupt change in elevation, exceeding aircraft limits. Permanent surface deformation was determined from robotic total station elevation measurements of cross sections and centerline profiles. Each of the following data collection categories were analyzed for compliance with the failure criterion:

1. centerline profile deformation,
2. unloaded surface deformation, and
3. loaded surface deformation

3.5.2.1 Centerline profile deformation

The difference in elevation between one or two stations apart (1 or 2 ft apart) was analyzed from plots of the centerline profile data to determine if an abrupt change in elevation reached failure limits during trafficking.

3.5.2.2 Unloaded surface deformation

Unloaded surface deformation was determined from data collected according to the methods described in section 3.4.2. The maximum deformation

at each location was determined as the difference in elevation from the average height of the elevated material on each side of the trough to the deepest point in the bottom of the trough. Measurements were averaged to obtain a single value for comparison to the failure criterion.

3.5.2.3 Loaded surface deformation

Loaded surface deformation was determined from data collected according to the methods described in section 3.4.3. The maximum deformation at each location was determined as the difference in elevation from the average height of the elevated material on each side of the trough to the deepest point in the bottom of the trough. Measurements were averaged to obtain a single value for comparison to the failure criterion.

4 Mat breakage

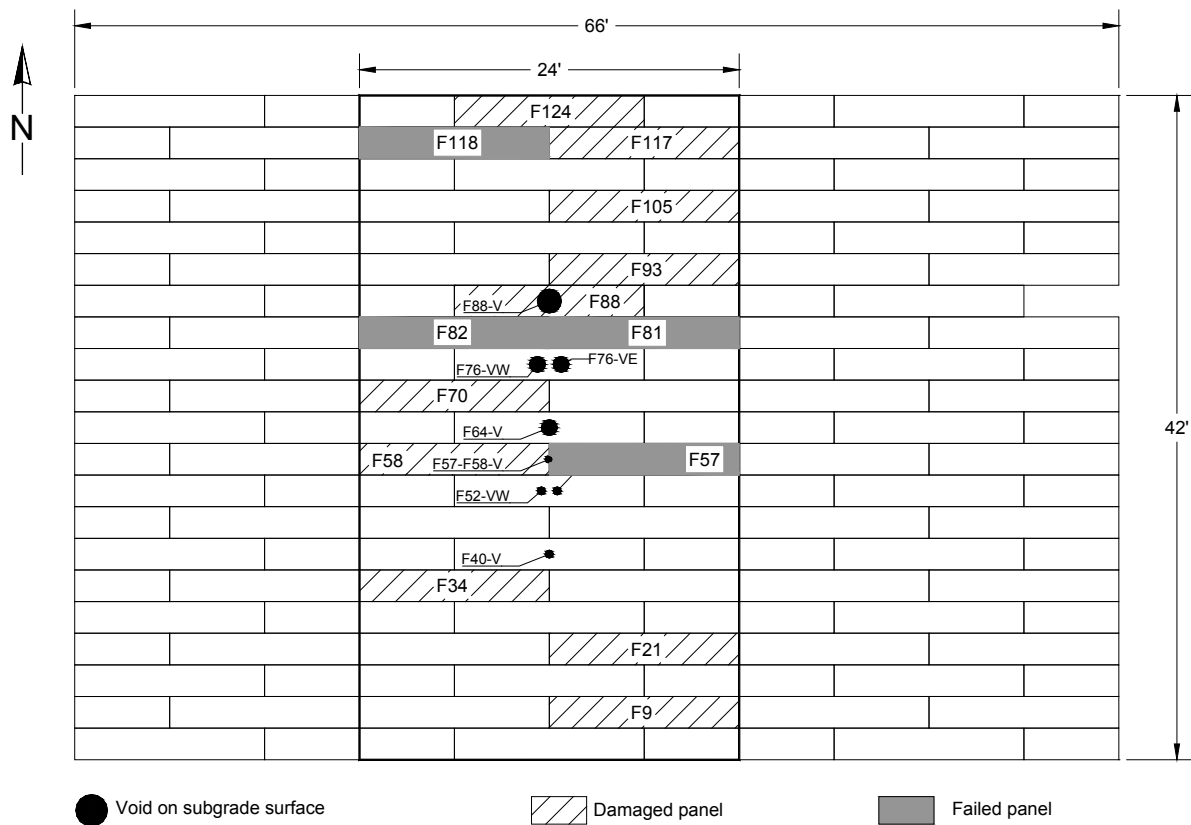
The following sections describe all mat breakage and the behavior of the AM2 airfield mat under F-15E and C-17 traffic.

4.1 Results

4.1.1 F-15E-V item

Figure 4.1 shows the layout of failed and damaged panels for the F-15E-V item after trafficking concluded.

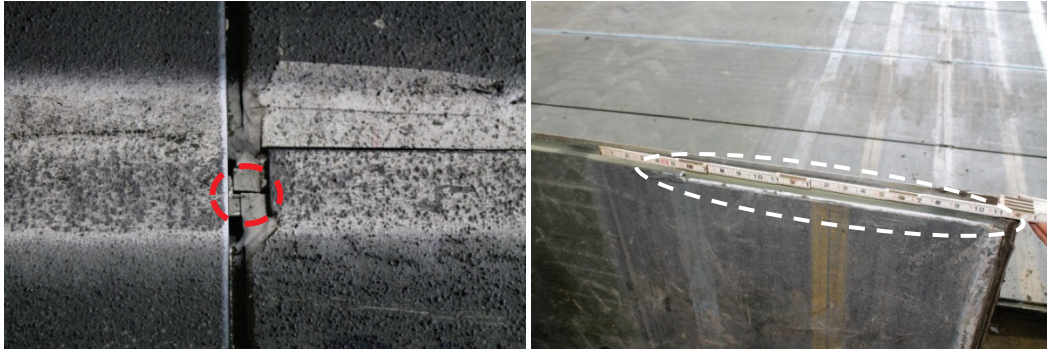
Figure 4.1. Layout of damaged and failed panels in the F-15-V item.



Trafficking of the F-15E-V test item began on July 9, 2013. No panel damage was noted until 32 passes were reached. Panel F70 had a 1/8-in. corner curl in the southeast corner. After 240 passes, Panel F81 failed when the upper underlap rail broke (Figure 4.2), allowing separation at the joint with F82. Panel F105 also developed a 1/8-in. corner curl in the southwest corner. After 496 passes, most panels with south corners

located on the traffic centerline developed 1/8-in. corner curls. Panel F81 had an 11-in.-long top skin tear after pass 548. The skin tear began near the southwest corner and propagated along the top flange of the female hinge. The loose piece of skin was posing a risk to the tire and was cut for maintenance.

Figure 4.2. Broken upper underlap rail (left) and top skin tear (right) in F81.



After 643 passes, Panel F118 failed when a 5-in.-long crack developed along the weld of the overlap end connector, causing the end connector to separate from the panel (Figure 4.3). Panel F82 had a 7-in.-long top skin tear along the top flange of the female hinge after pass 794. The loose piece of skin was removed to prevent a tire hazard. Panel F57 failed after pass 794 when the upper underlap rail broke. A 6.5-in.-long top skin tear had also developed.

Figure 4.3. Broken end connector in F118.



After pass 890, the top skin tear of Panel F82 increased to 11 in. causing the fourth panel failure. The top skin tear lengths on Panels F57 and F81 had increased to 9.5 in. and 23 in., respectively. Traffic was stopped after 1,008 passes due to tire hazards present throughout the traffic lane.

When the panels were removed after trafficking, additional damage was noted. Cracking along the center of the female hinge on Panel F124 had developed. The end connector weld crack on the bottom surface of Panel F118 was 10 in. long, starting at the female hinge connector side (Figure 4.3). Panel F88 developed cracking along the center of the female hinge with the bottom flange cracking and bent at the center (Figure 4.4). The overlap end connector weld on Panel F58 had cracked from the top surface to the bottom surface, and a 7-in.-long crack developed below the top flange of the female hinge. Table 4.1 summarizes post-traffic damage found in panels along with mat distresses and failures at various pass levels for the F-15E-V item.

Figure 4.4. F88 after removing from test section.



Table 4.1. Mat damage in F-15E-V item.

Pass Number	Panel Number	Description of Damage	Cumulative Failed Panels	Cumulative Mat Breakage, %
32	F70	Corner curl, 1/8 in. in southeast corner	-	-
240	F81	Upper underlap rail broke. Corner curl 1/8 in. in southwest corner	1	2.4
	F105	Corner curl, 1/8 in. in southwest corner	-	-
496	F9, F21, F34, F58, F82, F93, F117, F118	Corner curl, 1/8 in. in south corner on centerline of traffic lane	-	-
548	F81	Top skin tear length increased to 11 in. in southwest corner. Cut for maintenance to prevent a tire hazard	-	-
643	F118	5-in.-long crack developed along weld of prongs down end connector. End connector separating from panel	2	4.8
748	F82	Top skin tear developed, 7- in.-long. Cut for maintenance	-	-
794	F57	Upper underlap rail broke. Top skin tear developed, 6.5 in. long	3	7.1
890	F82	Top skin tear increased to length of 11 in.	4	9.5
	F57	Top skin tear increased to length of 9.5 in.	-	-
	F81	Top skin tear length increased to 23 in.	-	-
	F124	Cracking along center of female hinge	-	-
Posttest (1,008)	F118	End connector weld cracked length of 10 in. on bottom surface, starting at female hinge connector side	-	-
	F88	Cracking along center of female hinge. Bottom flange cracked and bent at center	-	-
	F58	Weld of overlap end connector cracked from top surface to bottom surface. Crack 7 in. long below top flange of the female hinge, starting at east edge	-	-

4.1.2 F-15E item

Trafficking of the F-15E test item began on July 29, 2013. Figure 4.5 shows the layout of failed and damaged panels for the F-15E item after trafficking concluded. No panel damage was noted until 240 passes were reached. Panel G58 failed when the upper underlap rail broke, allowing complete separation with connecting Panel G59 (Figure 4.6). Several panels with their joint along the traffic lane had a 1/16- to 3/16-in. corner curl in the south corner. After 406 passes, Panel G23 failed when the end connector detached from the panel (Figure 4.7). A crack was visible throughout the length of the weld. Panel G58 had a 6-in.-long tear in the top skin along the top flange of the female hinge. The loose piece of skin was removed because it was posing a risk to the tire. Removal of this skin revealed a 6-in. crack in the male hinge of Panel G53.

Figure 4.5. Layout of damaged and failed panels in the F-15E item.

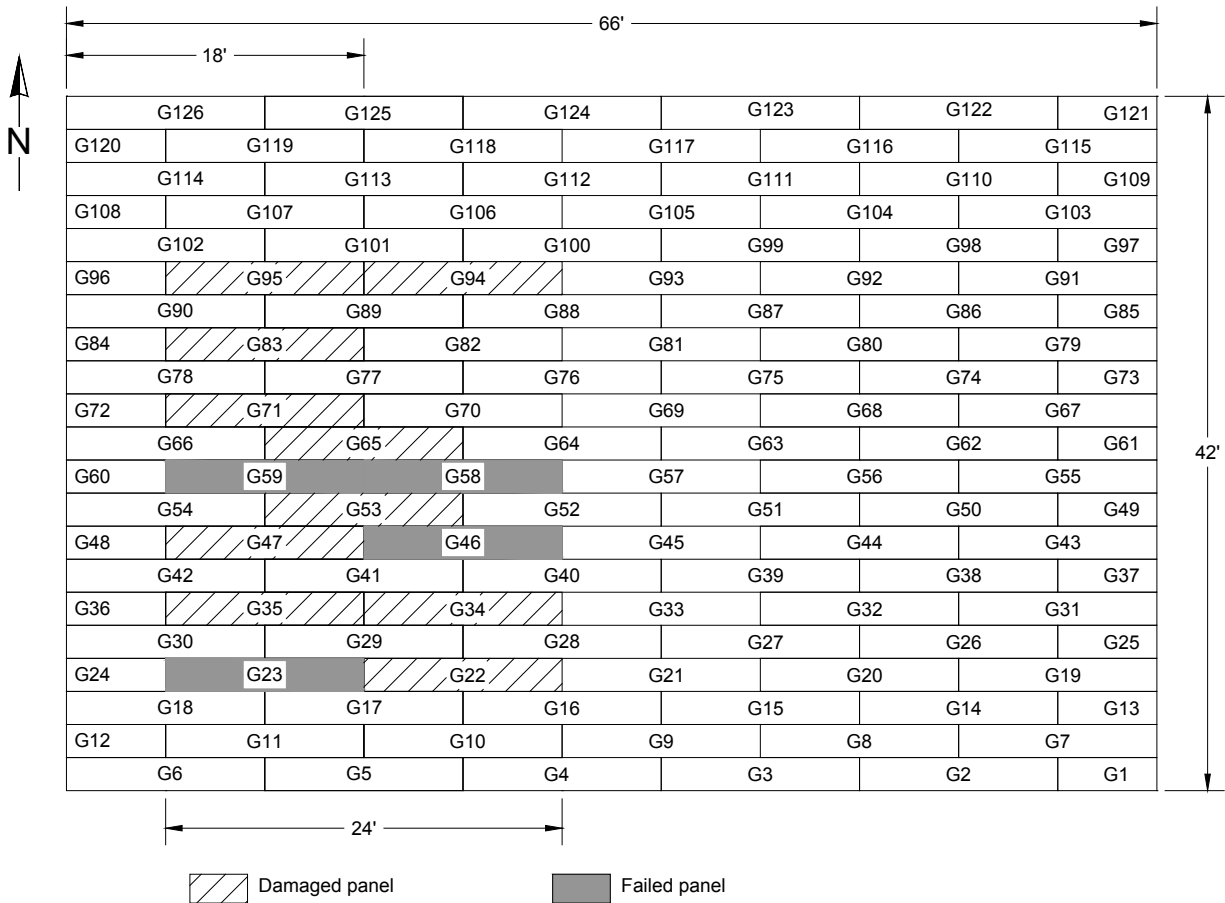


Figure 4.6. Broken upper underlap rail in G58.

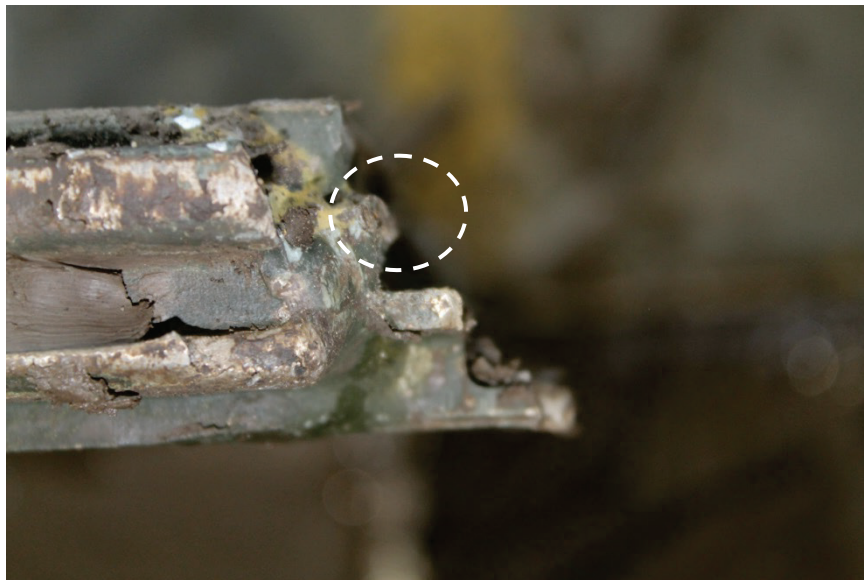
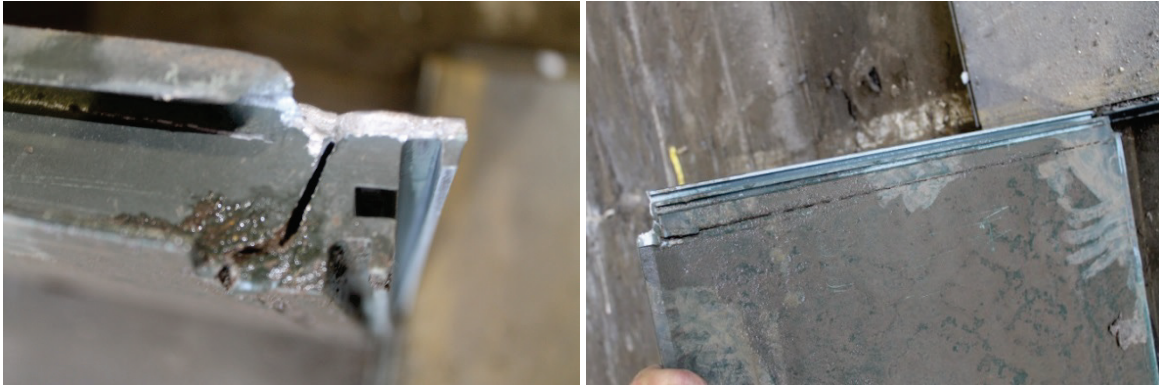


Figure 4.7. End connector weld failure at G23.



After pass 429, the upper under lap rail of Panel G46 broke, and Panels G23 and G59 had a small piece of the corner of the top skin chip off. After 476 passes, G59 had a top skin tear that was curled back a width of 2 in. along the weld and a length of 16 in. along the top flange of the female hinge, but had cracked a length of 9 in. (Figure 4.8). A vertical separation at the joint of G34 and G35 was noted, indicating breakage of a rail at one or both of the panels. Traffic was stopped due to tire hazards present throughout the lane.

Figure 4.8. Top skin tear in G59.



When panels were removed after trafficking was completed, additional damage was noted. The upper underlap rail of G34 broke a length of 10 in., starting at the north edge. However, since the length of breakage was less than 12 in. (half the length of the end connector), the panel was not considered failed. The bottom flange of the female hinge tore a length of 60 in. along the center of G65 (Figure 4.9). Panel G107 developed cracking at the weld of the overlap end connector, from the top surface to the bottom surface (Figure 4.10). Panel G71 had minor cracking at the southeast corner below the top flange of the female hinge connector. Table 4.2

summarizes post-traffic damage found in panels along with mat distresses and failures at various pass levels for the F-15E item.

Figure 4.9. G65 after removing from test section.



Figure 4.10. Crack at weld of overlap connector in G107.



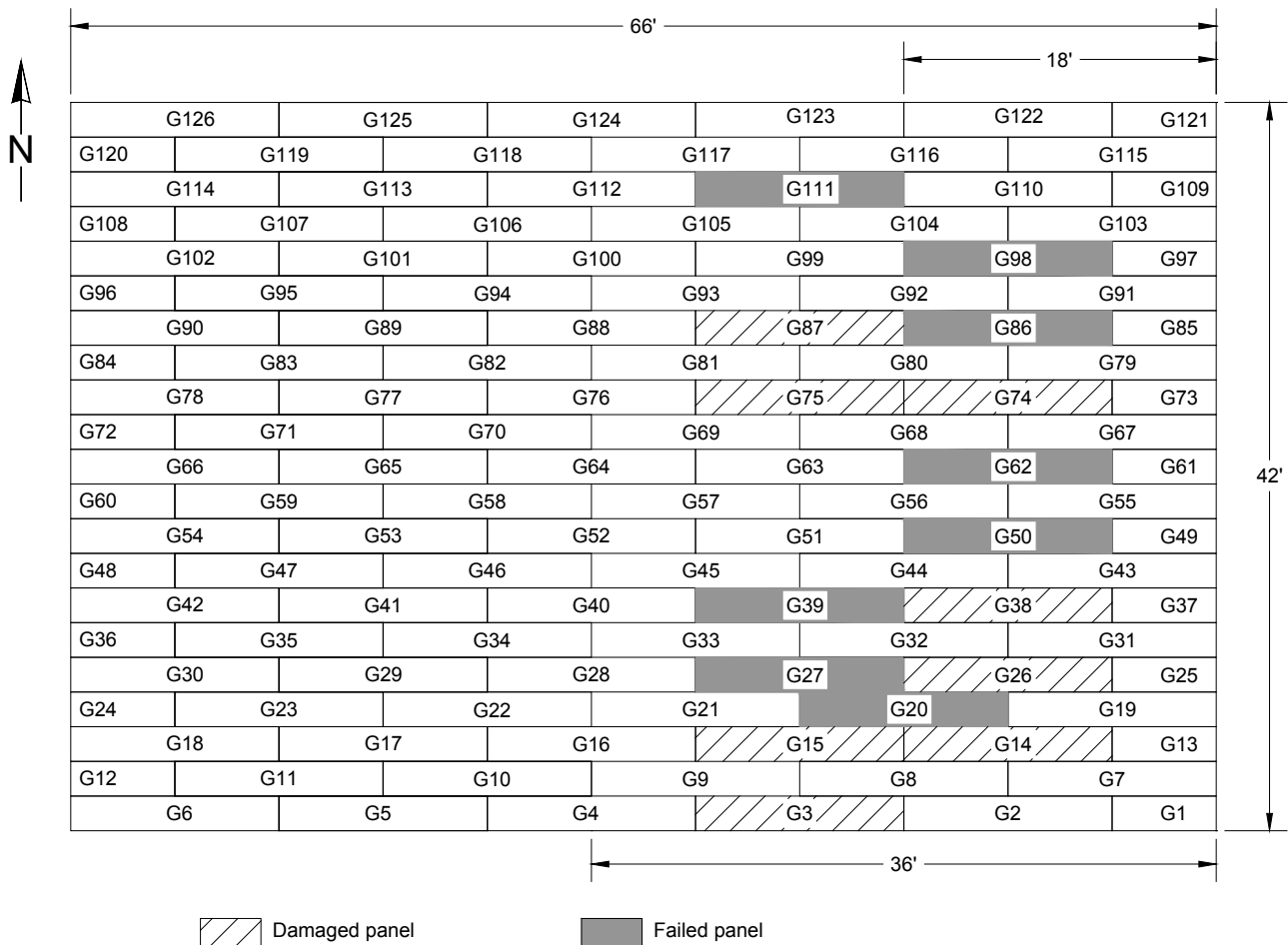
Table 4.2. Mat damage in F-15E item.

Pass Number	Panel Number	Description of Damage	Cumulative Failed Panels	Cumulative Mat Breakage, %
240	G58	Upper underlap rail broke	1	2.4
	G22,G23	Corner curl 3/16 in. in south corner on centerline of traffic lane	-	-
	G34, G35, G58, G59	Corner curl ¼ in. in south corner on centerline of traffic lane	-	-
	G94, G95, G47, G83	Corner curl 1/16 in. in south corner on centerline of traffic lane	-	-
406	G23	End connector detached from panel. Crack visible throughout length of weld. Corner curl increased to ¼ in.	2	4.8
	G58	Top skin tear in southwest corner, 6 in. Cut for maintenance to prevent a tire hazard.	-	-
	G53	Horizontal crack, 6 in., above male hinge connector. Crack visible due to skin removed from Panel G58.	-	-
	G46, G47	Corner curl ¼ in. in south corner on centerline of traffic lane	-	-
429	G59	Top skin on southeast corner chipped off	-	-
	G46	Upper underlap rail broke	3	7.1
	G23	Top skin on southeast corner chipped off	-	-
476	–	Traffic stopped	-	-
	G59	Top skin curled back length of 16 in. along top flange of female hinge and a width of 2 in. along the weld. Tear was 9 in. long	4	9.5
	G34	Vertical separation noted at joint with Panel G35	-	-
Posttest (476)	G107	Crack at weld of prongs down end connector, from top surface to bottom surface	-	-
	G71	Minor cracking in southeast corner, below top flange of female hinge connector	-	-
	G65	Bottom flange of female hinge tore length of 60 in. along center of panel	-	-
	G59	Cracking below top flange of female hinge (below the top skin tear) about 15 in.	-	-
	G58	Cracking below top flange of female hinge (below the top skin tear) about 18 in.	-	-
	G53	Bottom flange of female hinge tore length of 35 in. along center of panel	-	-
	G46	Crack at weld of underlap end connector, from top surface to bottom surface	-	-
	G34	Upper underlap rail broke at length of 10 in., starting at male hinge connector side	-	-

4.1.3 C-17 item

Trafficking of the C-17 test item began on August 1, 2013. Figure 4.11 shows the layout of failed and damaged panels for the C-17 item after trafficking concluded.

Figure 4.11. Layout of damaged and failed panels in the C-17 item.



No panel damage was noted until 168 passes were reached. Panel G50 and G62 each had the upper underlap rail break, which was evident from cracking visible on the north end at the upper underlap rail. Several panels had a slight corner curl in the south corner on the centerline of the traffic lane. After 308 passes, vertical separation was noted at many of the centerline joints, indicating failure of several rails. Traffic was stopped to prevent instability of the load cart.

When panels were removed after trafficking was completed, rail failures were confirmed for panels G20, G27, G39, G86, G98 and G111 (Figure 4.12). Panels G3, G15, G33, and G75 each developed cracking along the lower overlap rail, but the length of breakage was less than 12 in. in each panel. Since the end connector in these panels did not fully disengage from connecting panels for more than half the length of the joint, G3, G15, G33, and G75 were not considered failed (Figure 4.13). Table 4.3 summarizes post-traffic damage found in panels along with mat distresses and failures at various pass levels for the C-17 item.

Figure 4.12. Lower overlap rail failure in G111.

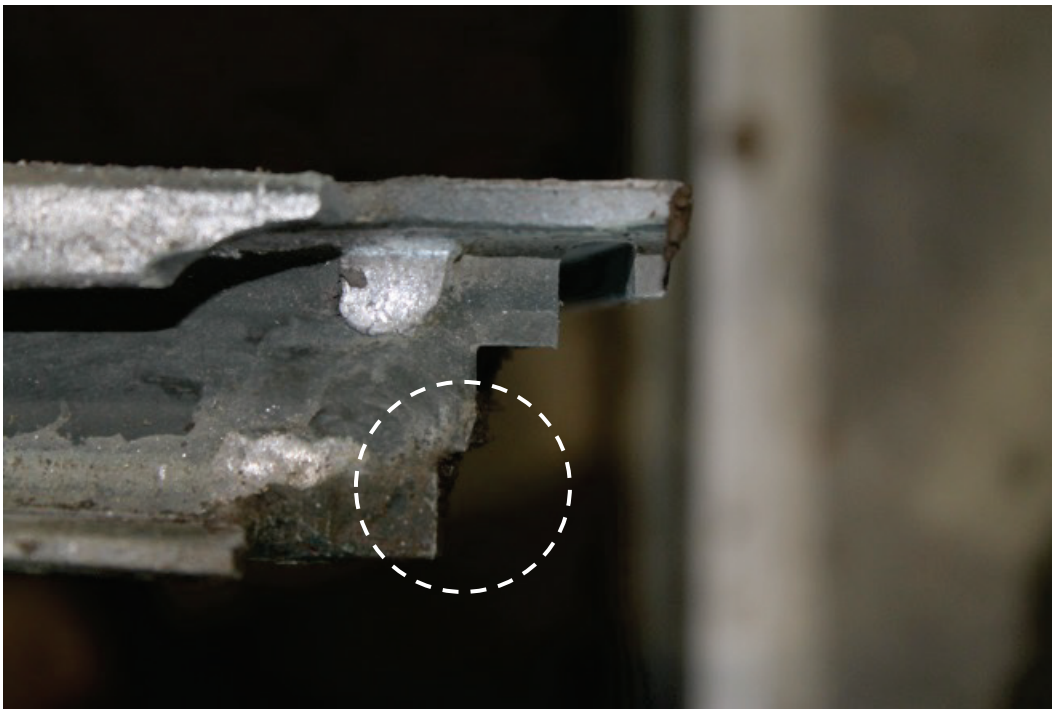


Figure 4.13. Partial breakage of lower overlap rail in G33.



Table 4.3. Mat damage in C-17 item.

Pass Number	Panel Number	Description of Damage	Cumulative Failed Panels	Cumulative Mat Breakage, %
168	G50	Upper underlap rail broke	1	1.6
	G62	Upper underlap rail broke	2	3.2
	G14, G26, G38, G50, G62, G74,	Slight corner curls on southwest corner on centerline of traffic lane	-	-
	G27	Slight corner curls on southeast corner on centerline of traffic lane	-	-
308	-	Traffic stopped. Vertical separation of joints throughout centerline. Most panels with joints on centerline failed.	-	-
Posttest (308)	G111	Lower overlap rail broke	3	4.8
	G98	Upper underlap rail broke	4	6.3
	G87	Upper overlap rail cracked and bent length of 3 in., starting at male hinge connector side	-	-
	G86	Upper underlap rail broke	5	7.9
	G75	Lower overlap rail broke length of 2 in., starting at female hinge connector side	-	-
	G39	Lower overlap rail broke	6	9.5
	G33	Lower overlap rail broke length of 8 in., starting at female hinge connector side	-	-
	G27	Lower overlap rail broke	7	11.1
	G20	Upper underlap rail broke	8	12.7
	G15	Lower overlap rail broke length of 6 in., starting at female hinge connector side	-	-
	G3	Lower overlap rail broke length of 5 in., starting at female hinge connector side	-	-

4.2 Analysis

4.2.1 F-15E-V item

The F-15E-V test item was trafficked until 1,008 passes were completed. Four (4) panels failed and the deformation on the subgrade and loaded mat surface exceeded 1.25 in. This is approximately a 35 percent reduction in performance when compared to results from Rushing and Tingle (2007). All damage (mostly corner curls and minor cracking) and failures were typical and similar to that observed by Rushing and Tingle (2007), Rushing and Torres (2007), Rushing et al. (2008), Rushing and Mason (2008), and Garcia and Rushing (2013) in AM2 when trafficked over weak subgrade conditions.

Upper underlap rail failure occurred because of stress concentrations located in the corner of the locking bar insertion slot at the interface with the smallest cross-sectional area of the rail. Cyclic loading caused a crack

to incubate in the described location and then propagate along the end connector until the rail completely separated from the panel. End connector cracking at the weld is normally associated with manufacturing defects at the weld location. Top skin tearing occurred because of shear forces subjected to the corner of the top skin of panels with joints along the centerline. A skin tear began as the corner curled upward or when a minor crack developed at the weld, but always propagated along the top flange of the female hinge. When the test tire was located along the joint, the top flange of the female hinge at the south edge pulled at the connecting male hinge for support. As cracking started to develop at (or near) the panel south corner, the top flange required support farther away from the joint, causing cracking to propagate along its length with increasing load repetitions.

With the exception of F118, it seems most failures occurred near the larger voids. As expected, F57, which had the joint directly with F58 above a void, failed at the connection. F58 was found to have damage after posttest inspection, but not enough to render it as failed. Posttest inspection also revealed extensive damage at the female connection of F88, which was located above the 18-in. void. However, it is likely that this was associated with failure at the connection of F82 and F81 and not necessarily with the void, mostly because similar damage was noted in other tests near joint failures.

It should be noted that a detailed investigation of the mat and subgrade conducted after this test revealed the manufacturer's drawing used for the extrusion die for the AM2 end connector inadvertently omitted filleted corners in the locking bar channel. These corners have been identified as areas of high stress concentrations where failure typically occurs. Follow-up testing was conducted by Garcia et al. (2015b) after the manufacturer corrected the drawings and produced new AM2 panels with filleted corners. Garcia et al. (2015b) conducted a side-by-side full-scale comparative test to determine whether an appreciable difference could be observed in the performance of AM2 with the filleted design versus the non-filleted design. AM2 panels were subjected to simulated F-15E traffic. The authors were able to prove that the filleted AM2 end connector design outperformed the non-filleted design by twice the number of passes to failure. The results of the filleted design showed good comparison to results from Rushing and Tingle (2007).

Thus, it is difficult to conclude whether damage noted in the F-15E-V item was more associated with the existence of voids or with the non-filletted end connector design. Similar testing conducted on a voided subgrade by Garcia et al. (2015a) on refurbished AM2 matting showed that voids did not affect mat performance significantly. It is reasonable, then, to assume the same for the F-15E-V item in this test.

4.2.2 F-15E item

The F-15E test item was trafficked until 476 passes were completed. Four (4) panels had failed and 1.25 in. of deformation was measured on the loaded mat surface. All damage and failures were typical and similar to that observed by Rushing and Tingle (2007), Rushing and Torres (2007), Rushing et al. (2008), Rushing and Mason (2008), and Garcia and Rushing (2013) in AM2 when trafficked over weak subgrade conditions. However, results represent about a 70 percent reduction in terms of passes-to-failure when compared to baseline testing conducted by Rushing and Tingle (2007).

The discussion in section 4.2.1 regarding follow-up investigations and testing by Garcia et al. (2015b) supports the assumption that premature failure of the F-15E item was likely caused by the non-filletted corners in the locking bar channel. Although mat breakage was premature in the F-15E item, the data collected were valuable for ensuring quality control in AM2 production and for future joint optimization studies that could improve end connector performance.

4.2.3 C-17 item

The C-17 test item was trafficked until 308 passes were completed and eight (8) panels had failed. All damage and failures were typical and similar to those observed by Rushing and Tingle (2007), Rushing et al. (2008), Rushing and Mason (2008), and Garcia and Rushing (2013) in AM2 when trafficked over weak subgrade conditions. However, results represent about an 80 percent reduction in terms of passes-to-failure when compared to baseline testing conducted by Rushing and Tingle (2007). All panel failures were either by breakage of the upper underlap or lower overlap rail. The discussion in sections 4.2.1 and 4.2.2 support the conclusion that the C-17 item failed prematurely because of a non-filletted end connector design.

5 Permanent deformation

5.1 Results

To show only the changes that occurred because of trafficking, the pre-traffic data were subtracted from all subsequent data collected after trafficking began to normalize the data. The discussions that follow are based on normalized data.

5.1.1 F-15E-V item

Plots of the centerline profile data on the subgrade and mat surface, as determined from robotic total station recordings, are shown in Figure 5.1 and Figure 5.2.

Figure 5.1. Subgrade centerline of the F-15E-V item after 1,008 passes.

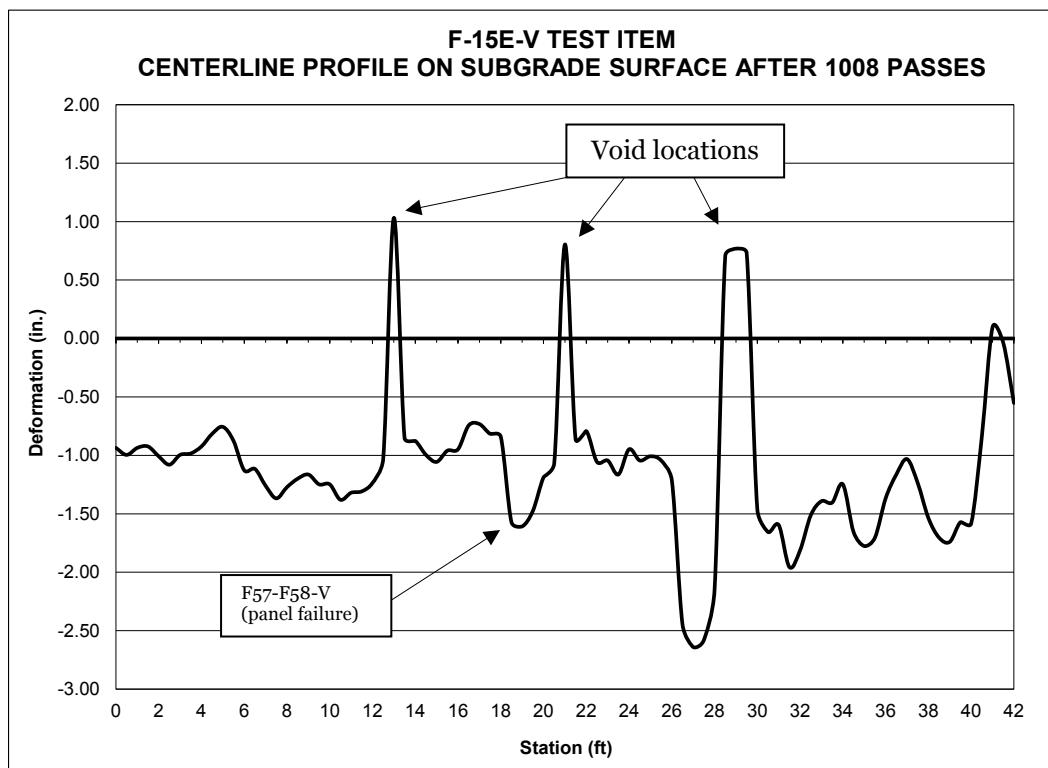
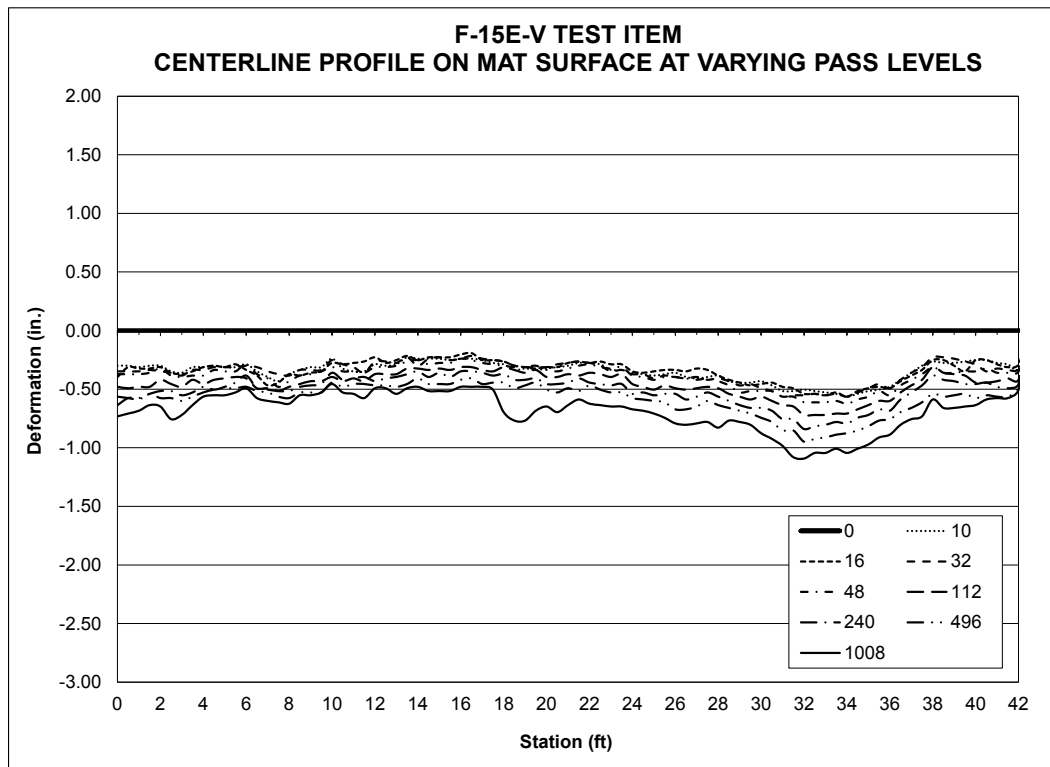


Figure 5.2. Centerline profile on the mat surface of the F-15E-V item.



In Figure 5.1, peaks observed at stations 13, 21, and 29 were the locations of voids F40-V, F64-V, and F88-V, respectively, along the centerline. The positive values are a result of rearrangement of material into the excavated void area during traffic. The initial depth of the voids was 2 in., but the depth decreased throughout traffic with the rearrangement of particles. These were ignored when determining the maximum roughness value. Stations 19 (location of void F57-F58-V) and 27 were areas of panel end connector rail failure and are represented as deep depressions in the subgrade. These were disregarded when analyzing the profile since they were associated with mat breakage and not necessarily with the system's ability (or inability) to prevent excessive roughness. Plots of the average cross-section elevation data, collected along lines A1, A2, and A3, are shown in Figure 5.3 through Figure 5.5

Figure 5.3. Average deformation on the subgrade of the F-15E-V item.

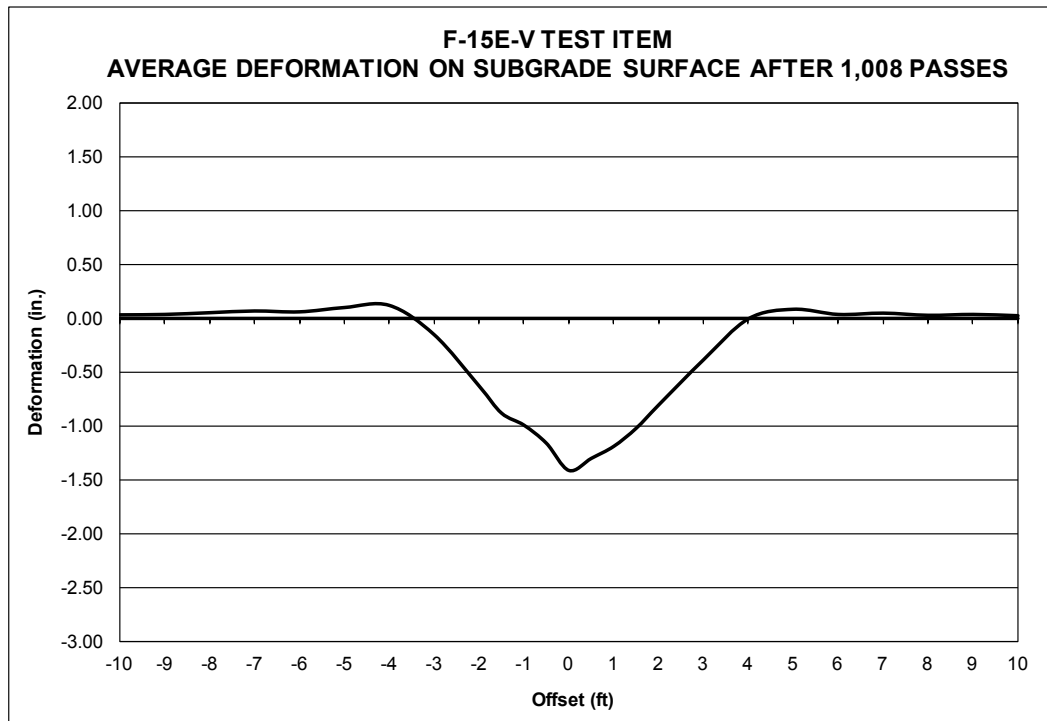


Figure 5.4. Average deformation on the loaded mat surface of the F-15E-V item.

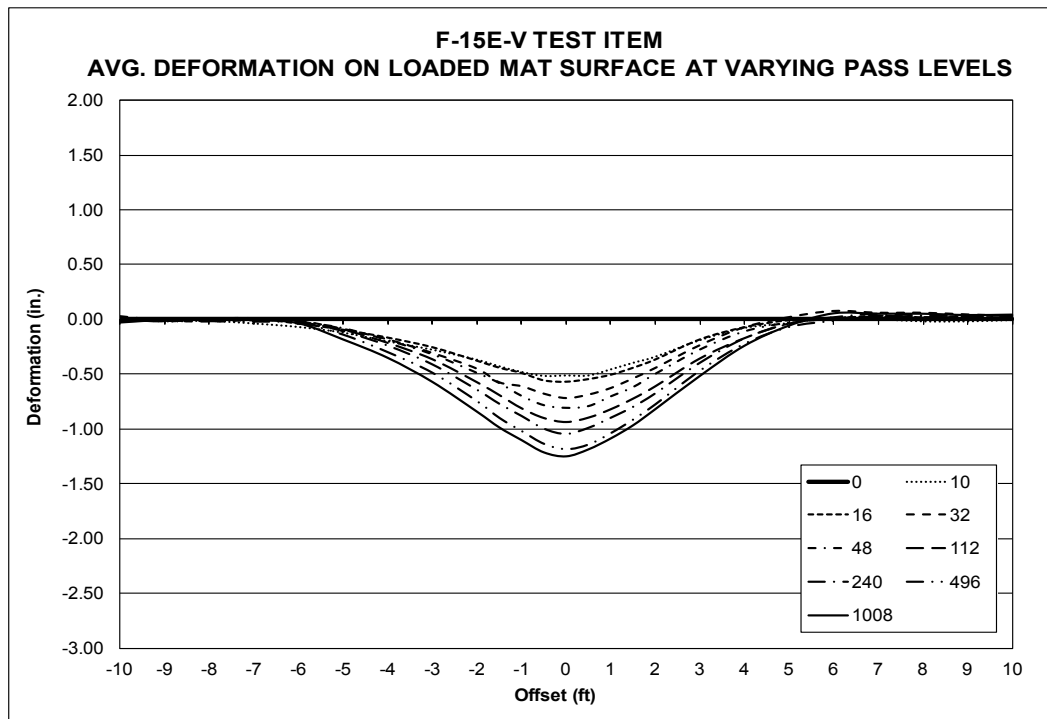
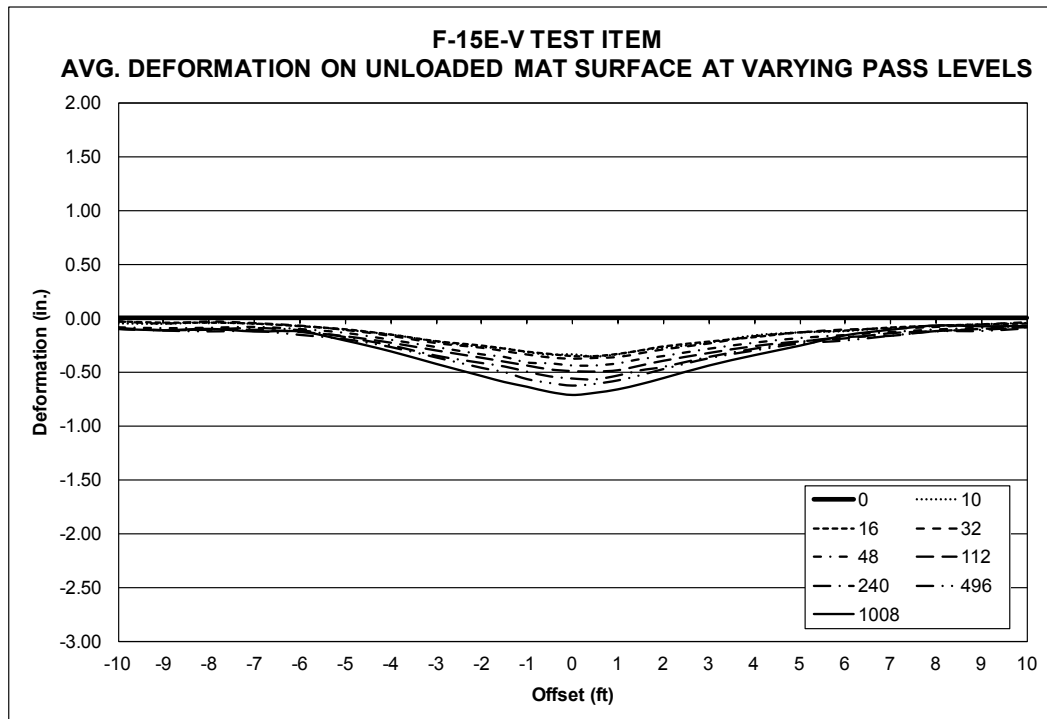


Figure 5.5. Average deformation on the unloaded mat surface of the F-15E-V item.



5.1.2 F-15E item

Plots of the centerline profile data, as determined from robotic total station recordings are shown in Figure 5.6 and Figure 5.7. Stations where panel failures occurred were disregarded when analyzing the profiles. An example of this is station 18 in Figure 5.6. Plots of the average cross-section elevation data, collected along lines A1, A2, and A3, are shown in Figure 5.8 through Figure 5.10.

Figure 5.6. Subgrade centerline profile of the F-15E item after 476 passes.

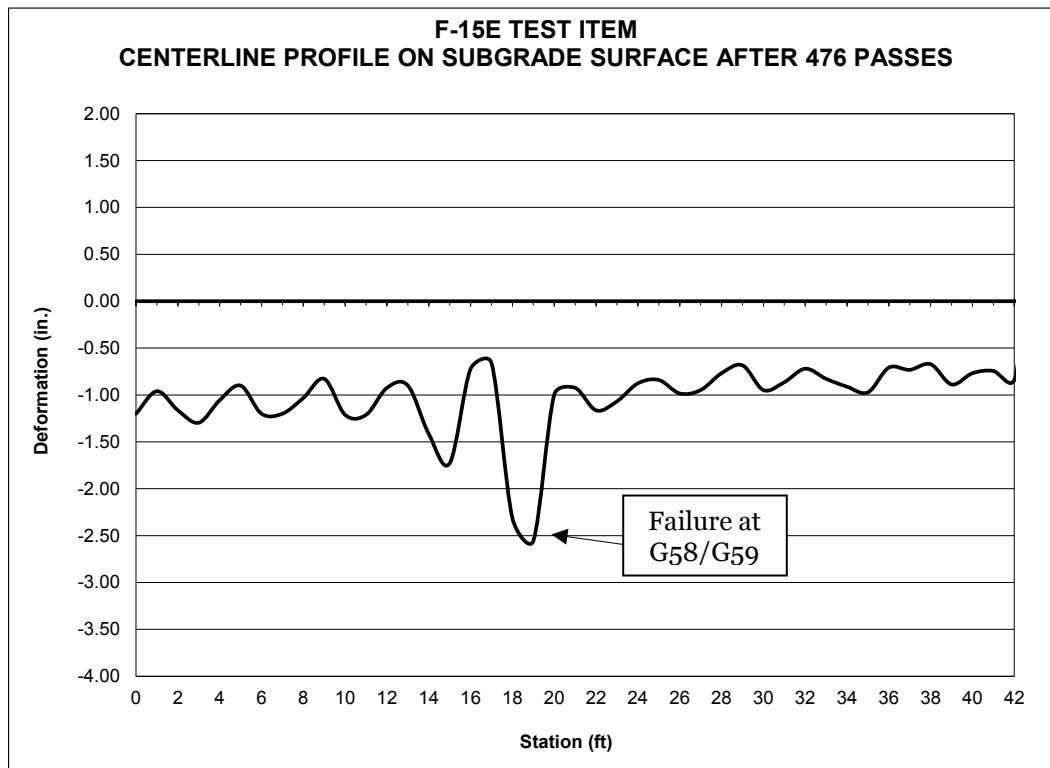


Figure 5.7. Centerline profile on the mat surface of the F-15E item.

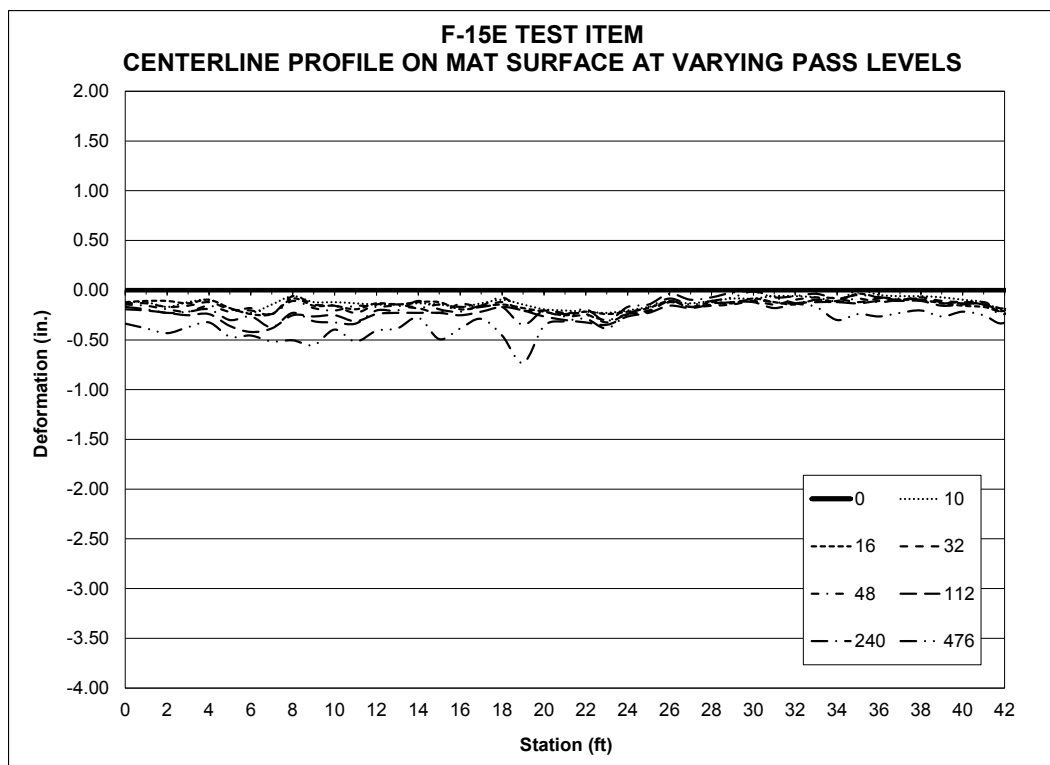


Figure 5.8. Average deformation on the subgrade of the F-15E item.

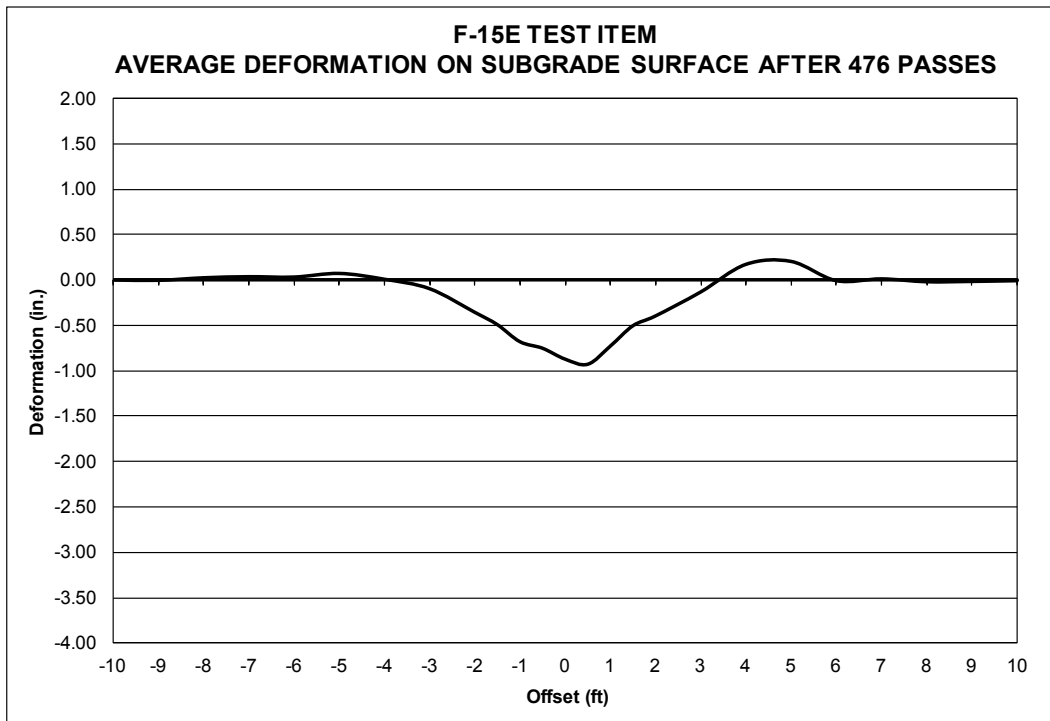


Figure 5.9. Average deformation on the loaded mat surface of the F-15E item.

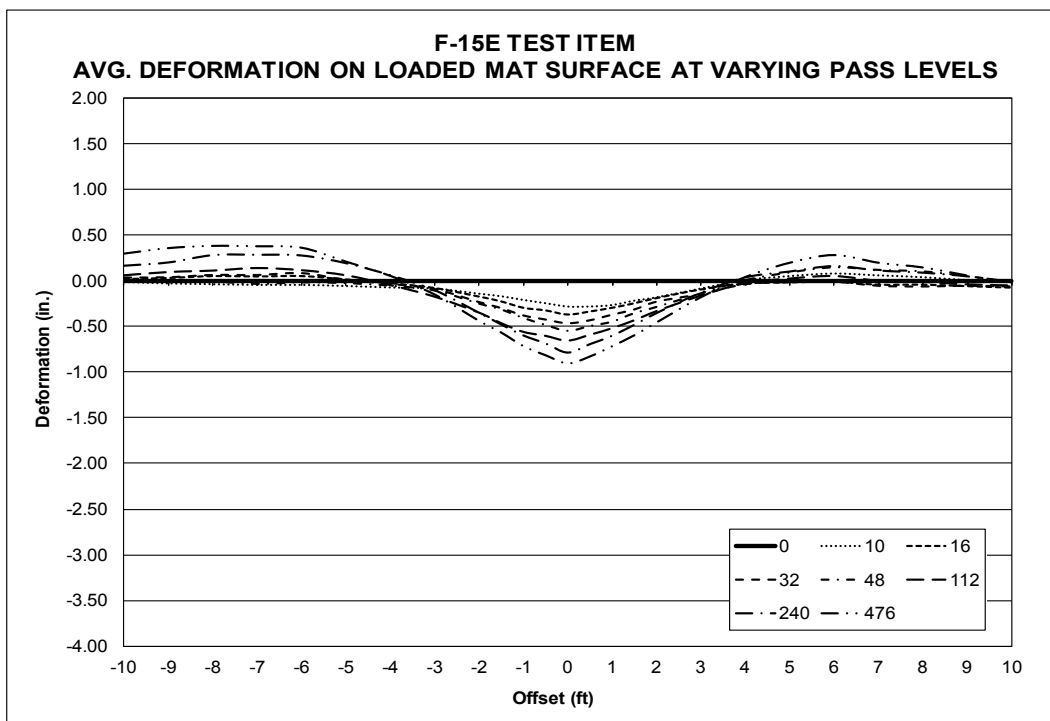
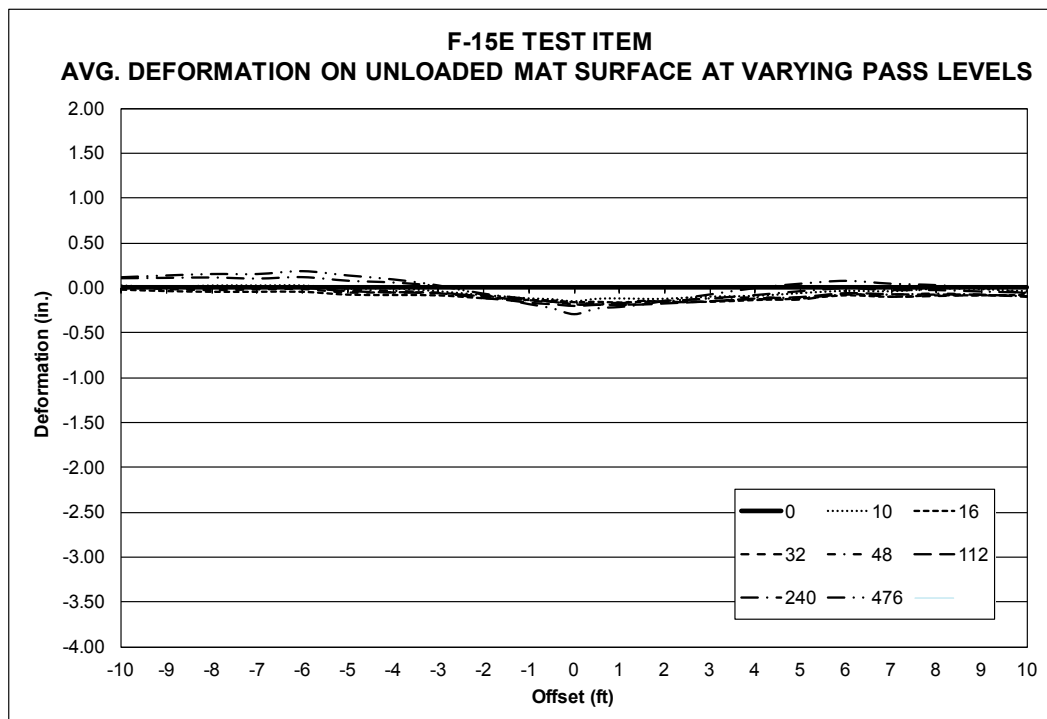


Figure 5.10. Average deformation on the unloaded mat surface of the F-15E item.



5.1.3 C-17 item

Plots of the centerline profile data, as determined from robotic total station recordings, are shown in Figure 5.11 and Figure 5.12. When determining the maximum roughness value in each item, boundary conditions were ignored (i.e., first and last two stations along the centerline). This was done because of the different properties at the interface of the test section subgrade and the surrounding material (much stronger). Plots of the average cross-section elevation data, collected along lines A1, A2, and A3, are shown in Figure 5.13 through Figure 5.15.

Figure 5.11. Subgrade centerline profile of the C-17 item after 308 passes.

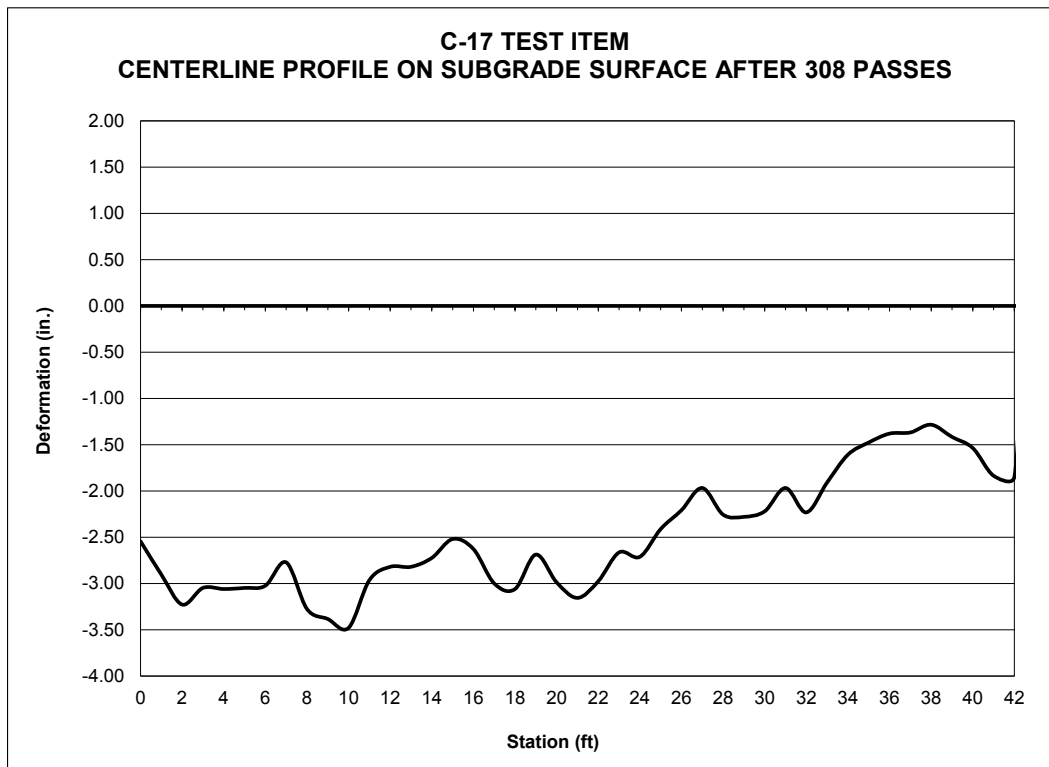


Figure 5.12. Centerline profile on the mat surface of the C-17 item.

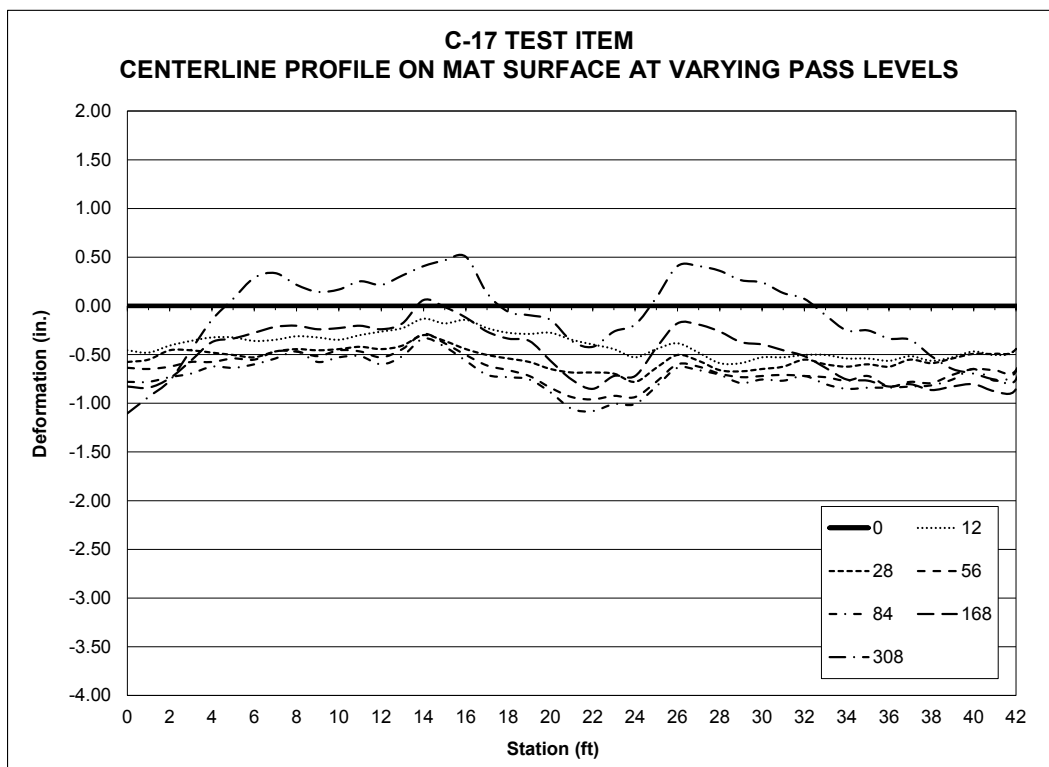


Figure 5.13. Average deformation on the subgrade of the C-17 item.

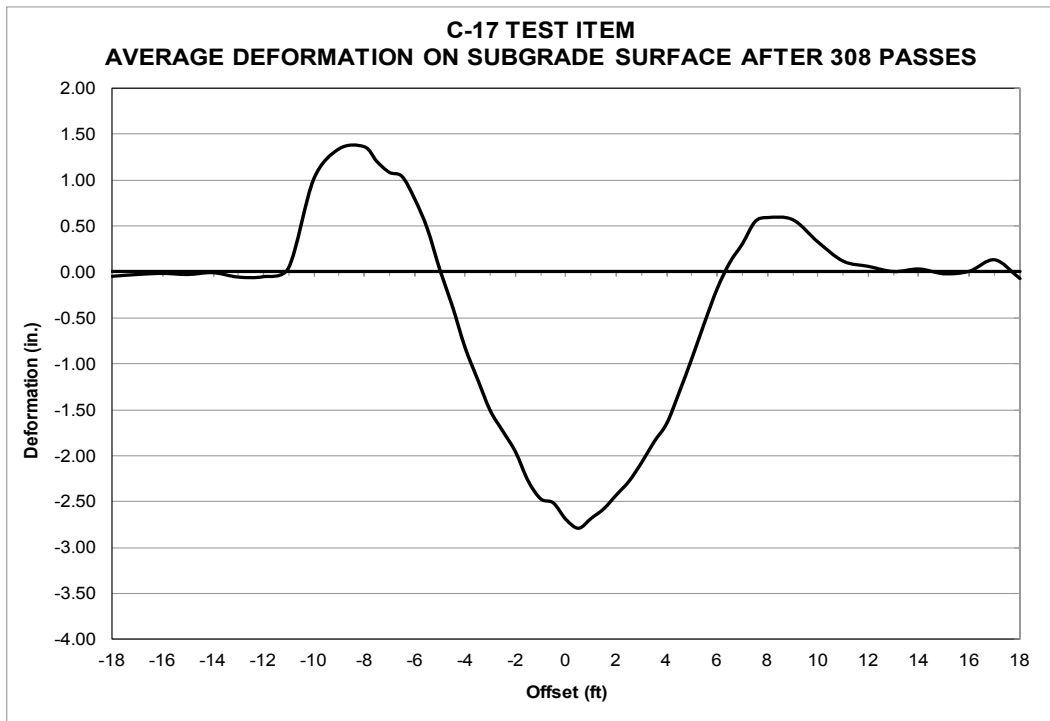


Figure 5.14. Average deformation on the loaded mat surface of the C-17 item.

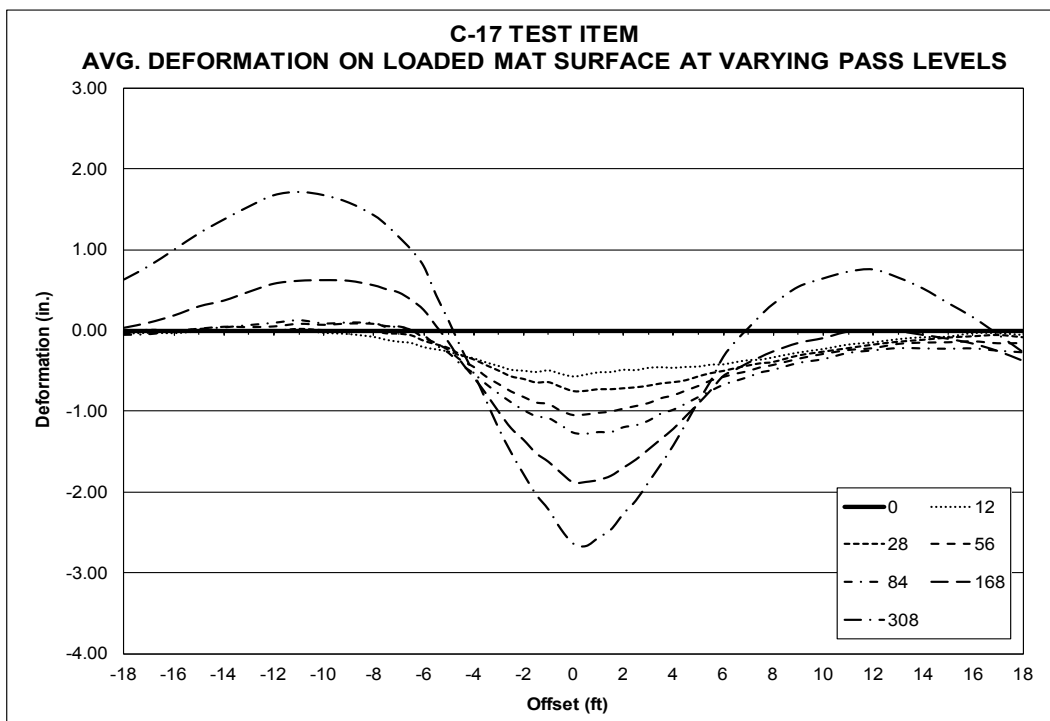
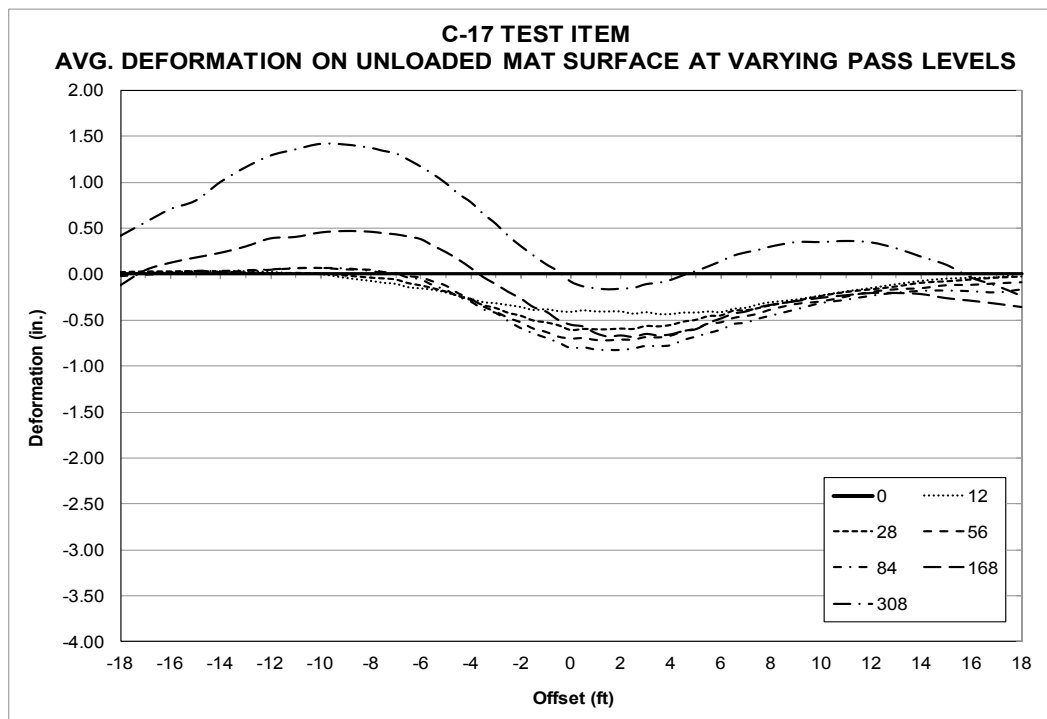


Figure 5.15. Average deformation on the unloaded mat surface of the C-17 item.



5.1.4 Summary

Table 5.1 summarizes maximum deformation values measured from data collected along the centerline profile and cross sections on all test items. Each of these values was compared to the failure criteria.

Table 5.1. Permanent deformation values for all test items.

Test Item	F-15E-V		F-15E		C-17	
Pass Number	496	1008	240	476	168	308
Subgrade Profile Max Abrupt Change in Elevation (in.)	-	0.53	-	0.40	-	0.20
Mat Surface Profile Max Abrupt Change in Elevation (in.)	0.13	0.19	0.14	0.16	0.54	0.60
Subgrade Permanent Deformation (in.)	-	1.54	-	1.11	-	3.85
Loaded Deformation on Mat Surface (in.)	1.21	1.32	1.02	1.25	2.20	3.91
Unloaded Deformation on Mat Surface (in.)	0.50	0.53	0.29	0.43	0.85	1.18

5.2 Void measurements in the F-15E-V item

In an attempt to monitor the progression of deformation where voids were excavated, observation holes were drilled in several panels at the positions where voids were located. Figure 5.16 shows the variation of the depth of the voids underneath the mat during traffic. After removing the mats, the voids were visually inspected to determine the extent of movement of material in those specific areas. It was observed that the diameter of the voids reduced and that material filled in the excavated areas, making the center of the voids nearly level and uniform with the subgrade surface. Figure 5.17 shows pretest and posttest photographs of voids F52-VW, F52-VE, and F88-V.

Figure 5.16. Void depth beneath the mat throughout traffic of the F-15E-V item.

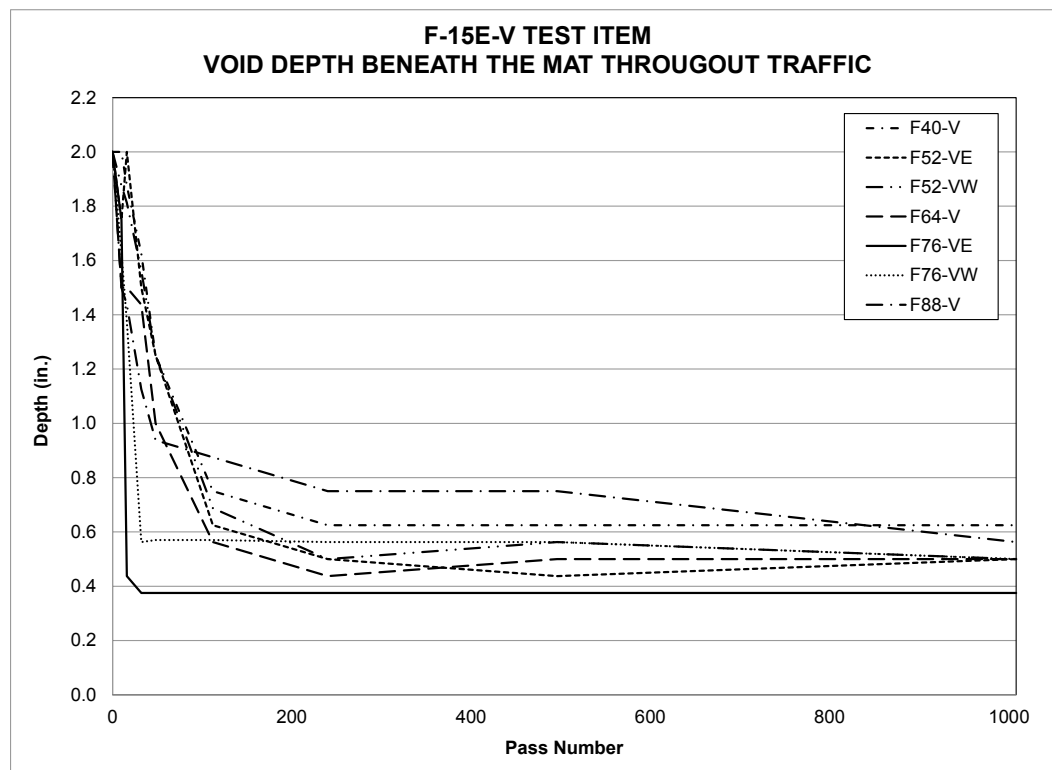
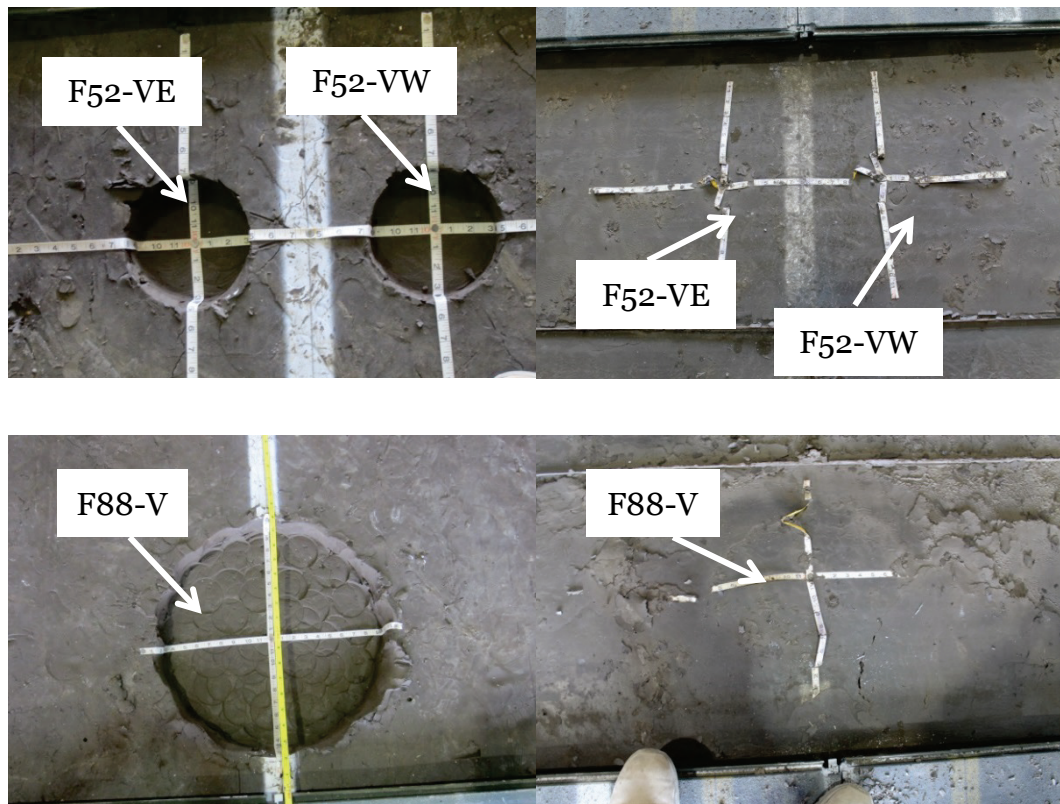


Figure 5.17. Pretest (a,c) and posttest (b,d) voids.



5.3 Analysis

The centerline profiles for the post-traffic subgrade and the surface of the mat at various traffic intervals were analyzed to determine whether the roughness criteria were exceeded. The permanent deformation on the subgrade, the loaded mat surface, and the unloaded mat surface was analyzed to determine whether the deformation criteria were exceeded.

5.3.1 F-15E-V item

5.3.1.1 Centerline profile

The values after 1,008 passes were below the 1.25-in.-deep maximum value established for roughness for F-15E aircraft traffic. Therefore, the system performed adequately to prevent excessive roughness from occurring along the profile. Similar behavior was also documented in previous brickwork pattern tests over a CBR of 6 (Rushing and Tingle 2007; Rushing and Torres 2007).

5.3.1.2 Cross sections

The failure criterion of 1.25 in. was exceeded on the subgrade and loaded mat surface after 1,008 passes. In previous tests over a CBR of 6 using the brickwork pattern, the deformation limit on the subgrade surface was exceeded after 1,792 passes (Rushing and Tingle 2007). On the unloaded mat surface, the authors reported a deformation of 0.28 in. at 768 passes, which increased to 0.36 in. after 1,280 passes. It seems the systems performance in terms of permanent deformation also reduced, further evidence of the discussion in section 4.2.1.

5.3.2 F-15E item

5.3.2.1 Centerline profile

The maximum values after 476 passes for the subgrade and mat surface were below the 1.25-in.-deep maximum value established for roughness for F-15E aircraft traffic. The system performed adequately to prevent excessive roughness from occurring along the profile, which is typical of the AM2 airfield mat on all subgrade conditions.

5.3.2.2 Cross sections

The permanent deformation on the loaded mat surface reached 1.25 in. after 476 passes. The failure criterion was met and results show a higher rate of increase in subgrade deformation when compared to results from Rushing and Tingle (2007).

5.3.3 C-17 item

5.3.3.1 Centerline profile

The values after 308 passes for the subgrade and mat surface were below the 3.0-in.-deep maximum value established for roughness for C-17 aircraft traffic. Therefore, the system performed adequately to prevent excessive roughness from occurring along the profile.

5.3.3.2 Cross sections

The failure criterion of 3.0 in. was exceeded on the subgrade and loaded mat surface. Rushing and Tingle (2007) reported similar behavior after 2,520 passes were applied where 3.25 in. of deformation were measured on the subgrade surface. Note that data in this test were affected by the

level of mat breakage at the centerline (i.e., rail breakage), which gives an unrealistic measure of the deformation at these stations.

6 Elastic Deflection

6.1 Results

Examples of the raw data as collected are shown in Figure 6.1 and Figure 6.2. These data were collected dynamically at scheduled pass intervals throughout trafficking. The data were processed by evaluating the elevation measurements within 3 in. from the centerline, shown as boundaries in Figure 6.1 and depicted as elevations in Figure 6.2. Calculations determined the average elevation of points within ± 3 in. of each centerline profile elevation location in terms of northing. The calculated average elevation corresponding to each station was then subtracted from measurements taken on the unloaded mat surface (i.e., centerline profile) at the same location. For example, the average of dynamic deflections at each station for Passes 17 through 32 was subtracted from the unloaded centerline profile recordings at each station collected at Pass 16. The difference in the loaded and unloaded measurements is the elastic deflection, or rebound, of the mat and subgrade as the test wheel moved over the surface. The average elastic deflection at each station for each data collection interval is shown in Figure 6.3 and Figure 6.4 for the F-15E-V and F-15E items, respectively. For the F-15E-V item, the elastic deflection increased to approximately 0.85 in. For the F-15E item, the elastic deflection increased to approximately 0.75 in.

6.2 Analysis

Historically, elastic deflection was used to monitor performance of mat systems, but was not used for mat system fatigue failure criteria. The elastic deflection measurements were the sum of the gap between the bottom surface of the mat and the top surface of the subgrade when the mat was unloaded (elastic deflection of the mat) and the elastic deflection of the subgrade. In the F-15E-V item, the elastic deflection increased to 0.8 in. after 50 passes and afterward generally remained constant at approximately 0.85 in. The constant measurements obtained from this test seem to indicate that the distance between the mat and the subgrade stayed relatively constant, and that the mat surface moved downward with the permanent deformation in the subgrade. In the F-15E item, the elastic deflection measurements generally increased throughout traffic until approximately 0.75 in. was reached. Previous tests demonstrated this

behavior, where an increase in elastic deflection was noted as the test progressed.

Figure 6.1. Elastic deflection measurements' wander distribution on F-15E-V item.

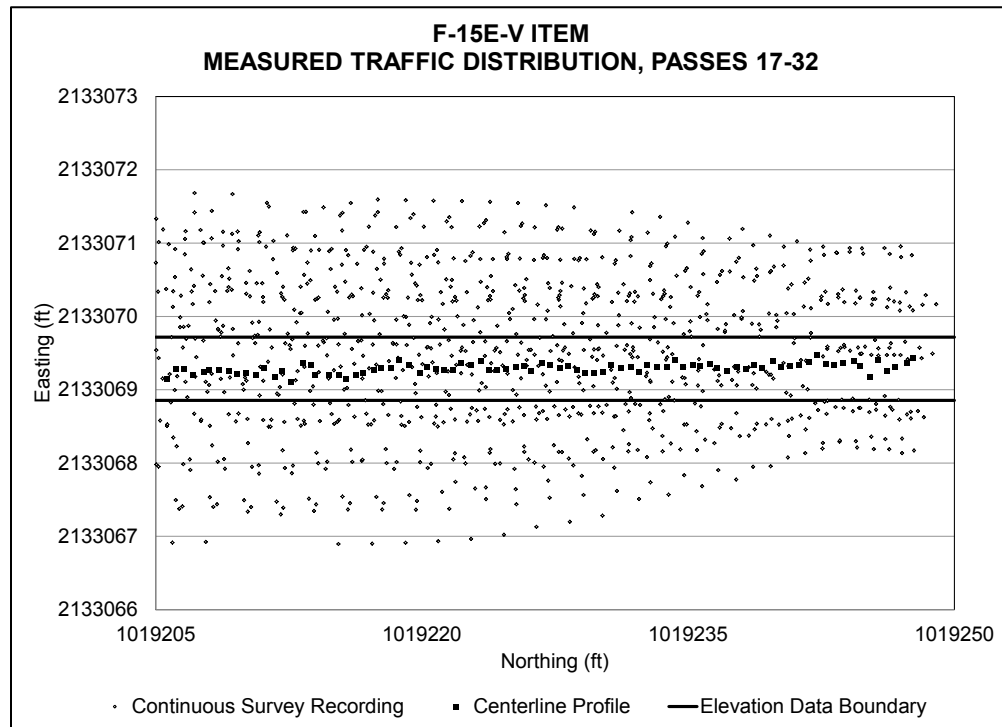


Figure 6.2. Elastic deflection elevation distribution on F-15E-V item.

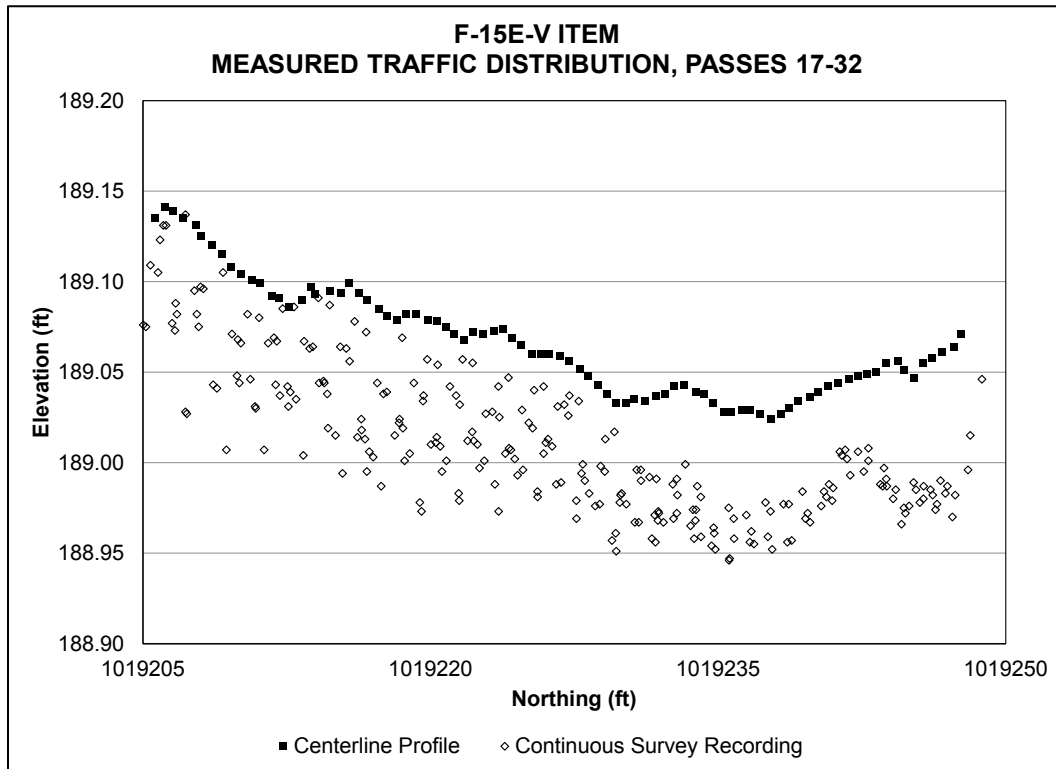


Figure 6.3. Elastic deflection on F-15E-V item mat surface at various pass levels.

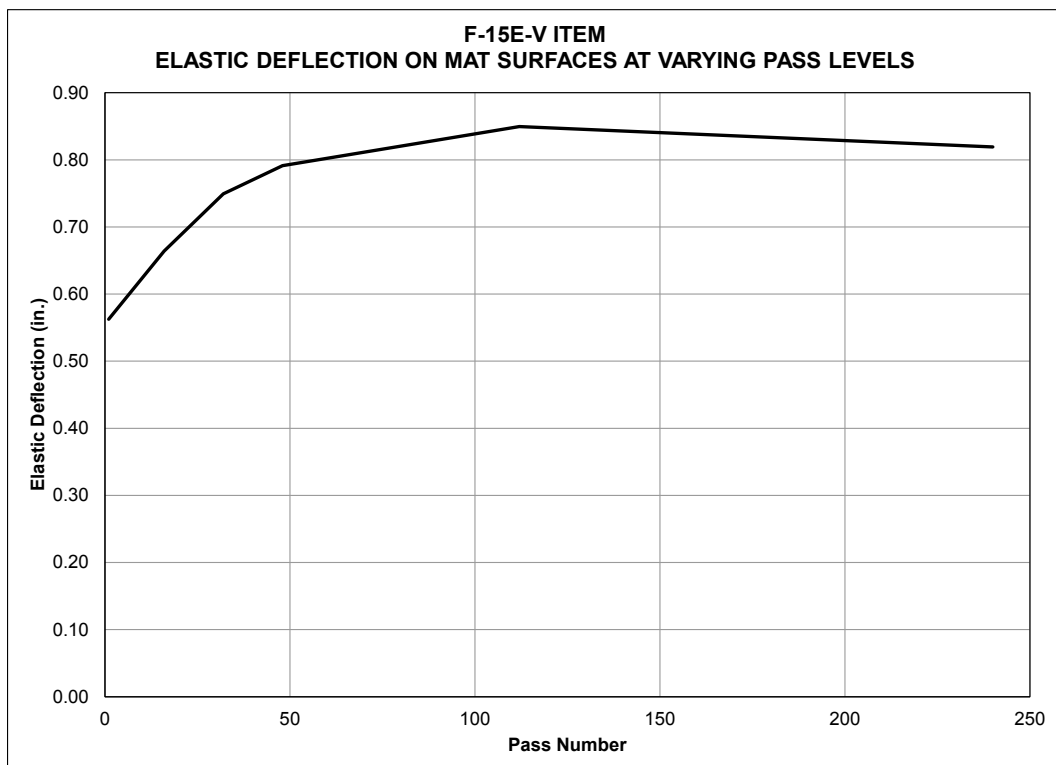
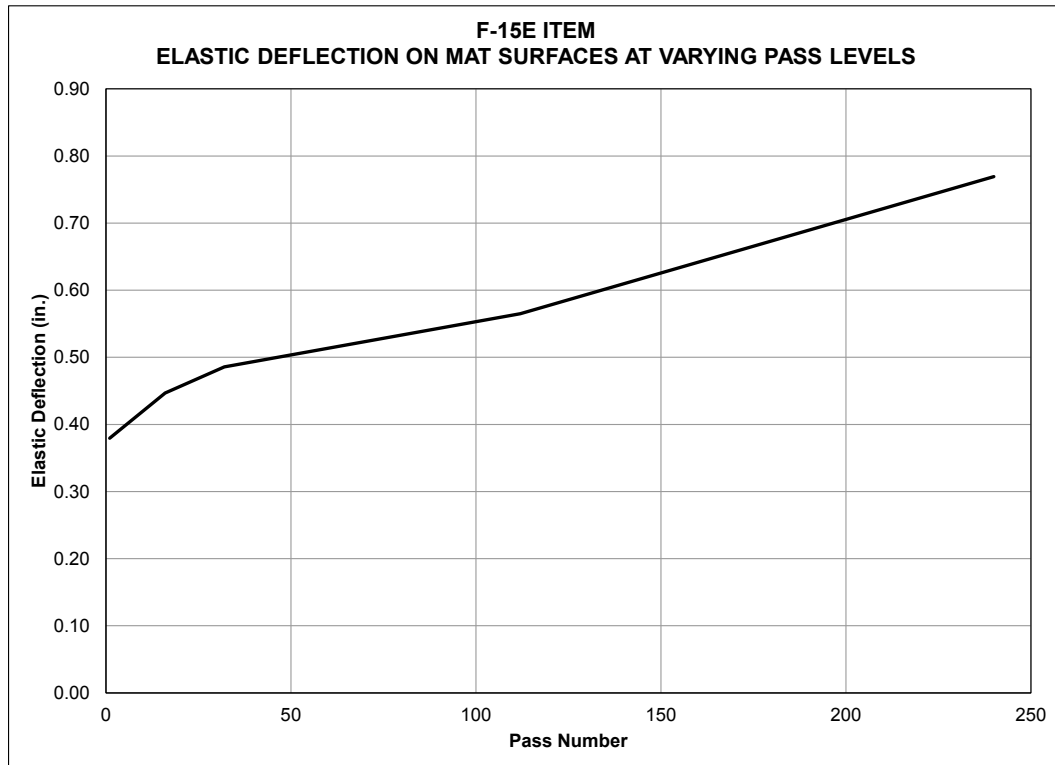


Figure 6.4. Elastic deflection on F-15E item mat surface at various pass levels.



7 Strain Data

7.1 Results

7.1.1 F-15E-V item

The strain gauge layouts for the F-15E-V instrumented panel joints are shown in Figure 7.1. The various combinations of panel movements and panel-to-panel resistance are illustrated in Figure 7.2 for the recorded compressive or tensile strain. Panel movement at the panel-to-panel end joints is the primary factor determining whether a strain gauge measured compressive or tensile strain. Only the locking bar transfers the vertical shear force across the joint for the compressive strain situations, whereas both the prongs and the locking bar transfer this force across the joint in tensile strain situations. This can be seen in Figure 7.3 by comparing the magnitude of the peak strains for passes 1 and 2 versus passes 9 and 10; passes 3 and 4 versus passes 7 and 8; and, pass 5 versus pass 6 for the F45-F46 joint.

Figure 7.1. F-15E-V item strain gauge layouts.

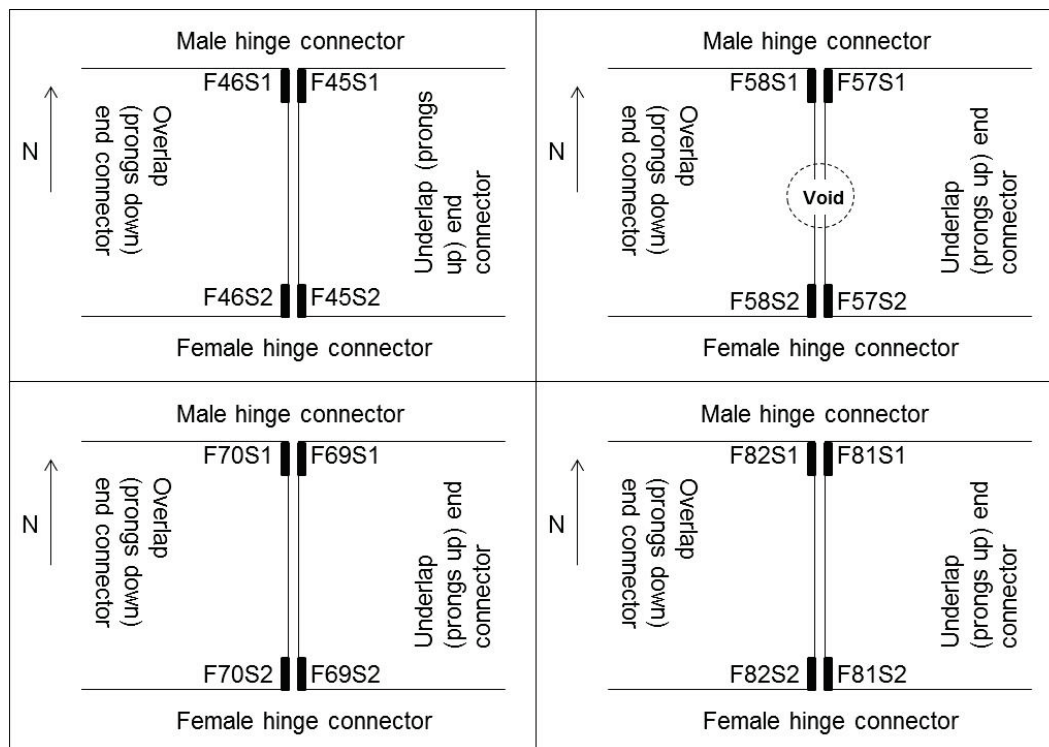
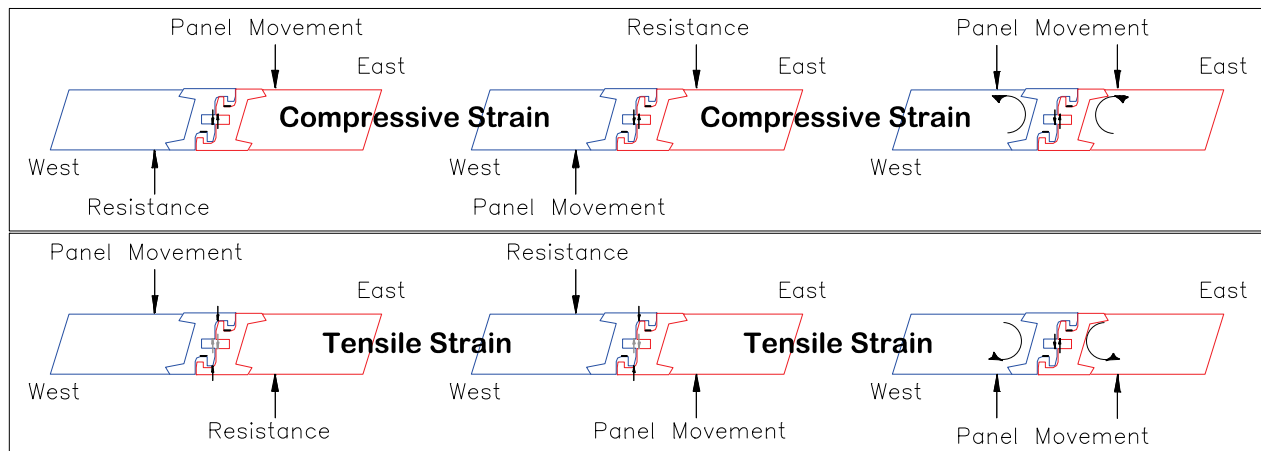


Figure 7.2. Panel movement for compressive and tensile strains.



The strain gauge measurement range was approximately $\pm 20,000$ microstrains. Measured values outside this range were indicative of gauge failure. Gauge failures correlated well with the observed mat break-age results, validating that the strain gauge range was appropriate.

Pass 1 (northbound) and pass 2 (southbound) subset of the same data is shown in Figure 7.4. During pass 1 the load cart wheel was centered approximately 18 in. east of the joint on Panel F45. The wheel was located at the F45 south/female hinge edge first, deflecting it downward, evidenced by the compressive strains recorded for F45S2 and F46S2. At the same time the north edge of the F45 panel was being forced upward, evidenced by an increase (tensile strain direction) in the F45S1 and F46S1 strain readings. The compressive-tensile strain reading sequence was reversed during pass 2 for the F45S1-F46S1 and F45S2-F46S2 gauge pairs.

Strain magnitudes were generally higher closest to the joint during the early load cart passes, particularly for compressive strains. However, deformation of the mats and subgrade as the number of traffic passes increased created much more unpredictability in the panel movement, creating more exceptions to the theory that load applied closer to the joint yields higher magnitude strain. This observation is illustrated by the F45-F46 joint strains for passes 697-716 in Figure 7.5.

Figure 7.3. F-15E-V item F45-F46 panel joint strains for passes 1-10.

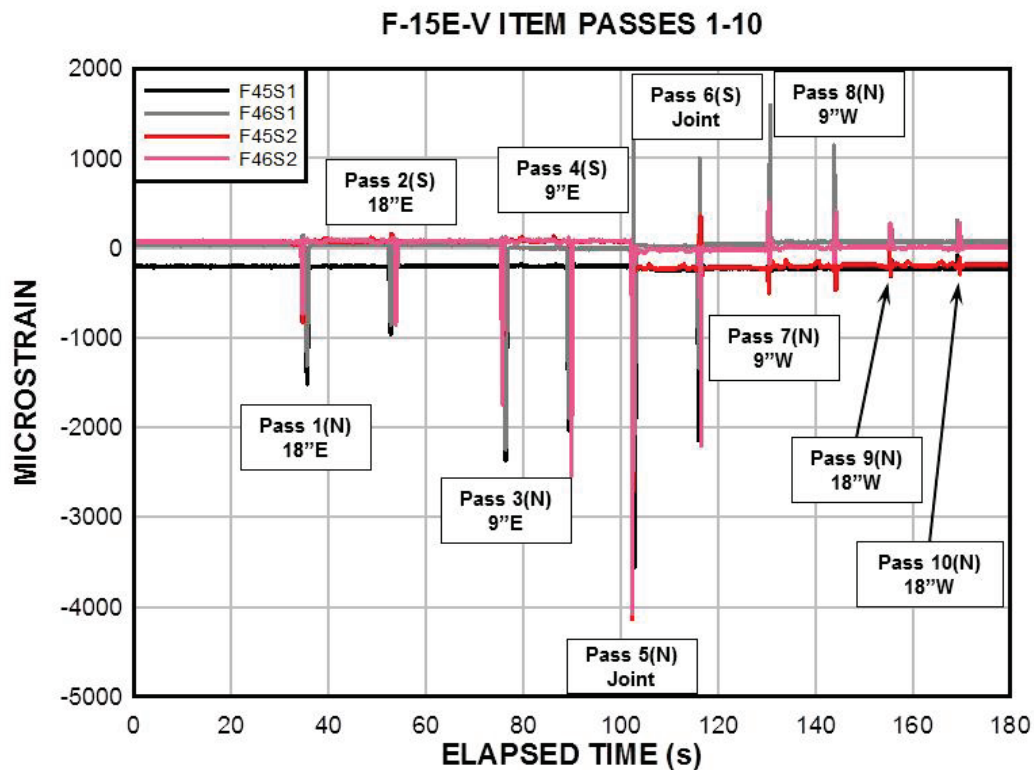


Figure 7.4. F-15E-V item F45-F46 panel joint strains for passes 1-2.

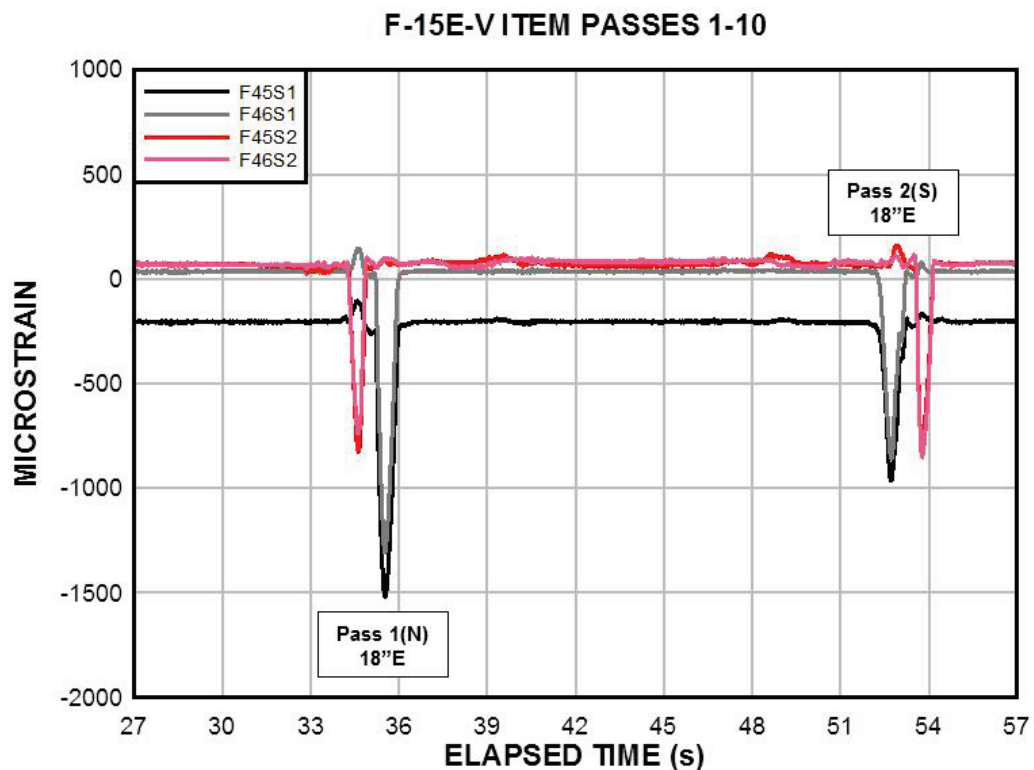
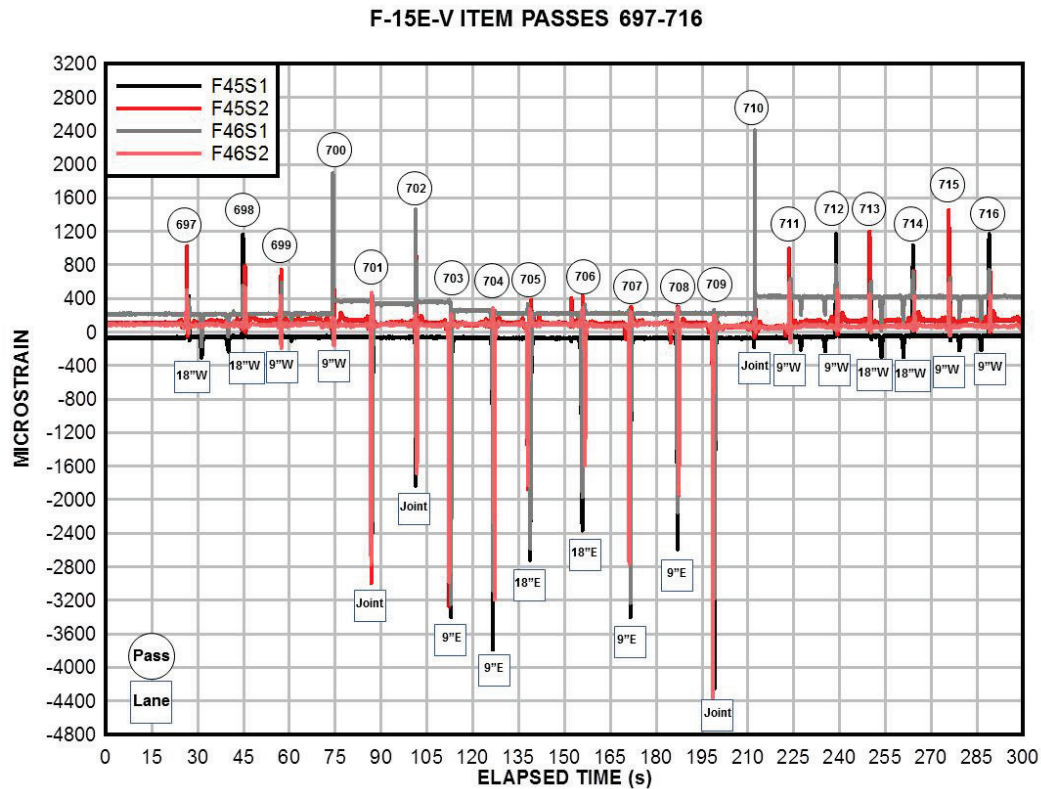


Figure 7.5. F-15E-V item F45-F46 panel joint strains for passes 697-716.



From the raw data, the maximum tensile strains and the absolute value of the maximum compressive strains were captured for each gauge throughout. The maximum values recorded for each gauge and traffic pass range are tabulated in Appendix A. Each of these plots shows data for joining panels in each test item. Table 7.1 shows the average of these values, between 0 and about 20,000, and lists compressive or tensile for the highest average along with the percent difference between them. The compressive strain average was significantly higher than the tensile strain average for 14 of the 15 gauges, indicative of the load sharing between the locking bar and prongs when tensile strains are occurring at the gauge locations.

Table 7.1. F-15E-V item average maximum strains.

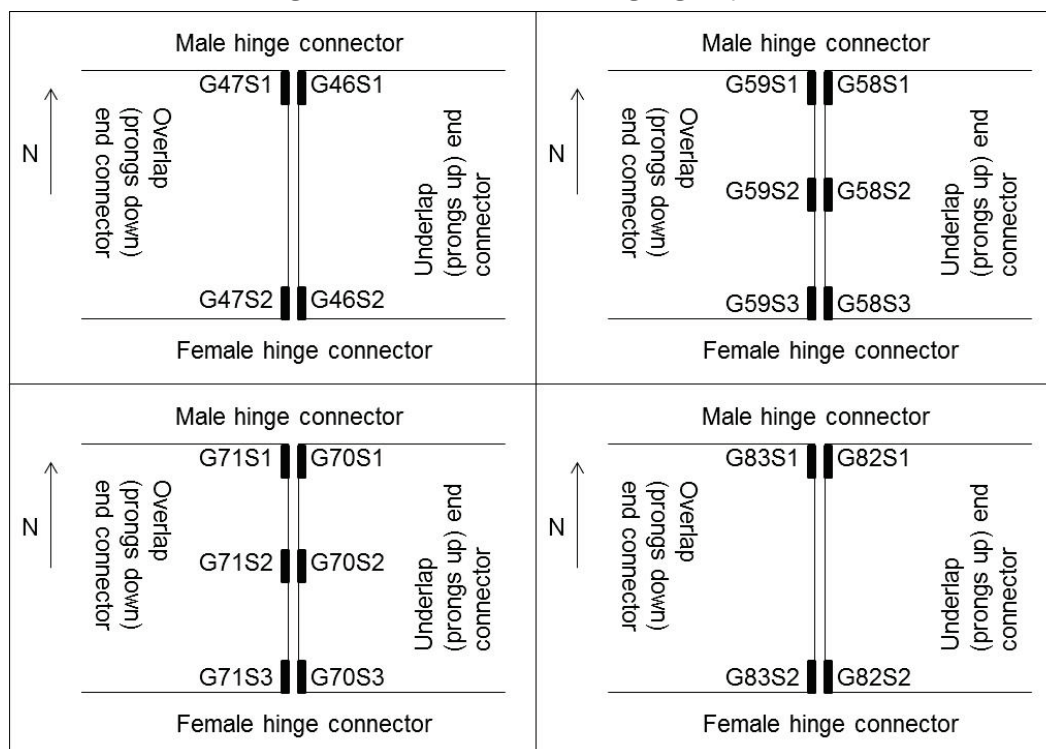
Panel Joint	Gauge	Stress	Max Strain ($\mu\epsilon$)	Average of Values >0 and <20,000 ($\mu\epsilon$)	Highest Average % Difference
F45-F46	F45S1	Compression	4,660	4,055	Compressive
		Tension	1,672	979	314%
	F45S2	Compression	4,677	4,126	Compressive
		Tension	1,945	1,207	242%
	F46S1	Compression	4,955	3,494	Compressive
		Tension	3,123	1,771	97%
	F46S2	Compression	4,751	4,277	Compressive
		Tension	944	735	482%
F57-F58	F57S1	Compression	3,167	2,876	Compressive
		Tension	3,064	1,084	165%
	F57S2	Compression	4,240	3,744	Compressive
		Tension	2,085	1,224	206%
	F58S1	Compression	4,945	3,076	Compressive
		Tension	3,076	1,818	69%
	F58S2	Compression	Bad Data		
		Tension	Bad Data		
F69-F70	F69S1	Compression	4,312	3,791	Compressive
		Tension	1,385	879	331%
	F69S2	Compression	3,712	2,966	Compressive
		Tension	1,371	947	213%
	F70S1	Compression	3,731	2,709	Compressive
		Tension	2,521	1,563	73%
	F70S2	Compression	3,787	2,946	Compressive
		Tension	2,892	1,835	61%
F81-F82	F81S1	Compression	3,237	2,621	Compressive
		Tension	2,159	686	282%
	F81S2	Compression	20,791	2,929	Compressive
		Tension	21,793	1,237	137%
	F82S1	Compression	2,763	1,833	Tensile
		Tension	2,746	1,867	2%
	F82S2	Compression	2,045	1,247	Compressive
		Tension	978	436	186%

7.1.2 F-15E item

The strain gauge layouts for the F-15E instrumented panel joints are shown in Figure 7.6. The higher compressive versus tensile strain levels can be seen in Figure 7.7 by comparing the magnitude of the peak strains for passes 1 and 2 versus passes 9 and 10, passes 3 and 4 versus passes 7

and 8, and pass 5 versus pass 6 for the G46-G47 panel joint. The traffic pattern shown in Figure 3.19 is the mirror image of Figure 3.19 (i.e., pass 1 started west of the centerline).

Figure 7.6. F-15E item strain gauge layouts.



The strain gauge measurement range was approximately $\pm 20,000$ microstrains. Measured values outside this range were indicative of gauge failure and gauge failures correlated well with the observed mat breakage results, validating that the strain gauge range was appropriate. The pass 1 and pass 2 subset of the data in Figure 7.7 is shown in Figure 7.8. During these passes, the load cart wheel was centered approximately 18 in. west of the joint on Panel G47. The wheel contacted the G47 south/female hinge edge first deflecting it downward, evidenced by tensile strains recorded for G46S2 and G47S2. At the same time the north edge of G47 was being forced upward, evidenced by tensile strains in the G46S1 and G47S1 strain readings. The compressive-tensile strain reading sequence was reversed during pass 2 for the G46S1-G47S1 and G46S2-G47S2 gauge pairs.

Figure 7.7. F-15E item G46-G47 panel joint strains for passes 1-10.

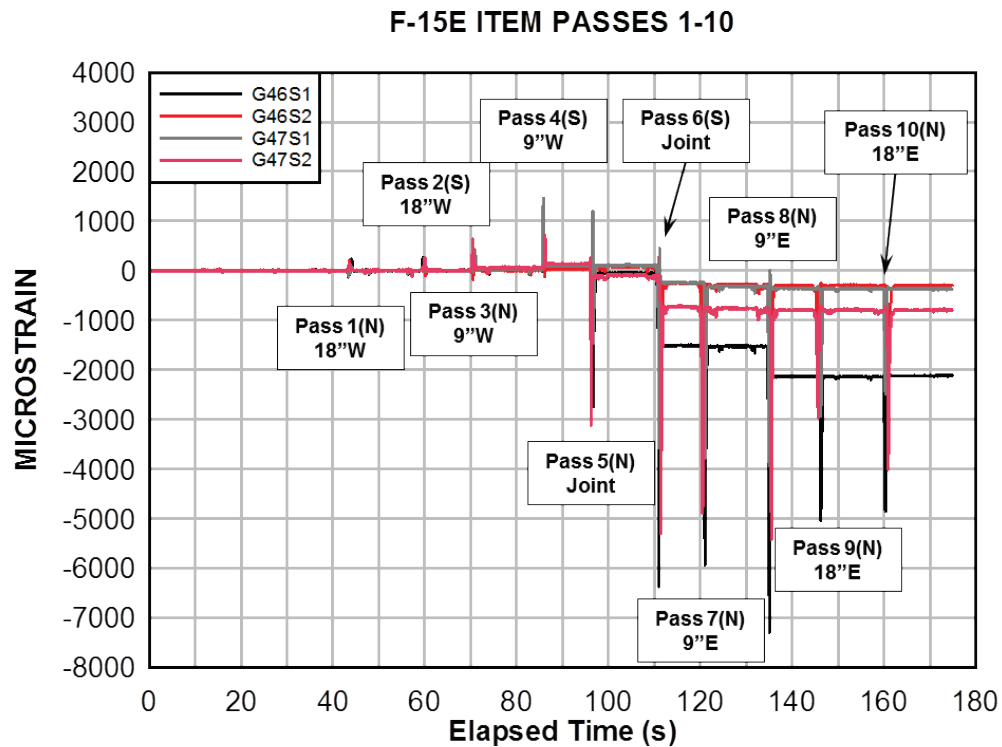
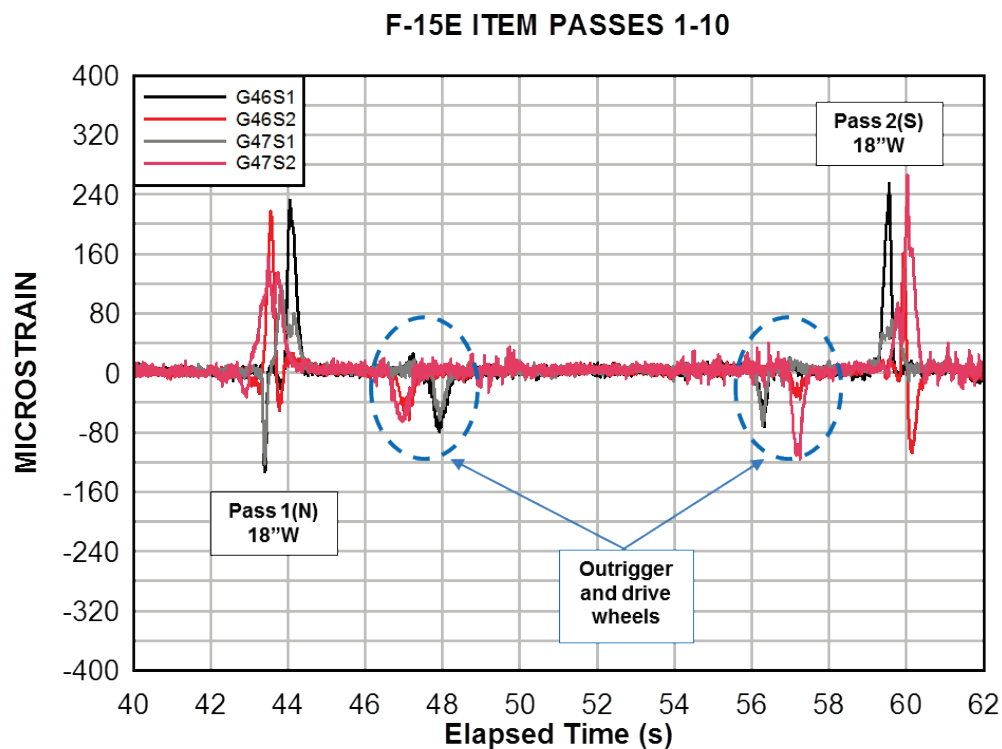
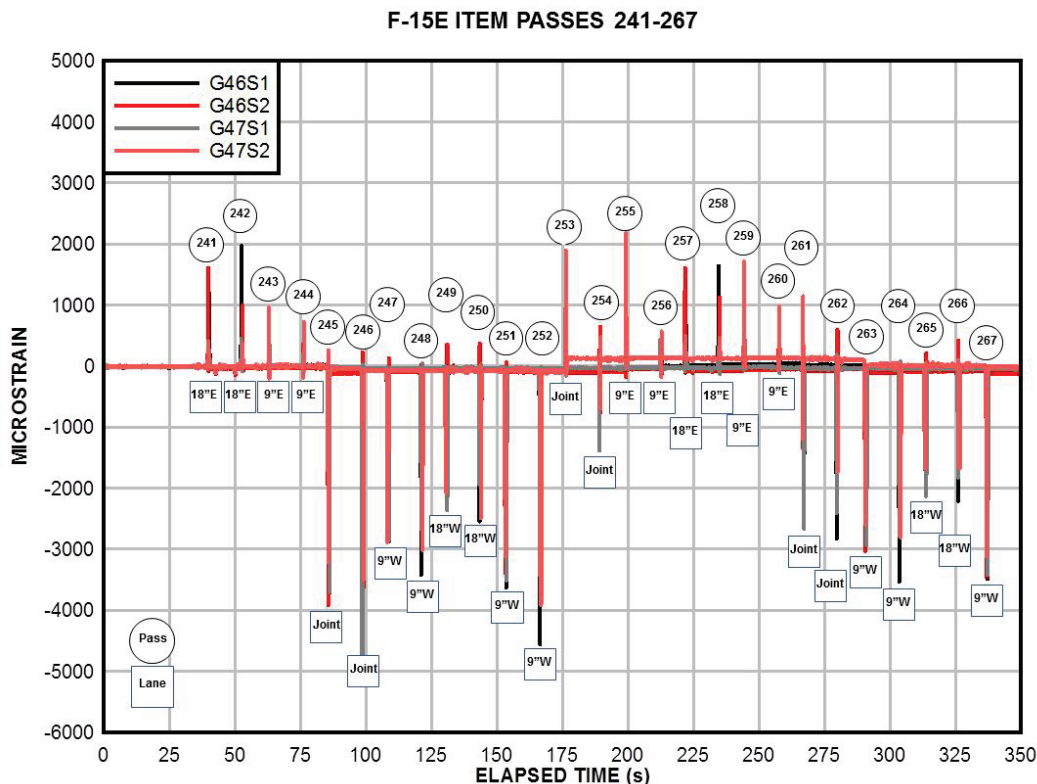


Figure 7.8. F-15E item G46-G47 panel joint strains for passes 1-2.



Strain magnitudes were generally higher closest to the joint during the early load cart passes, particularly for compressive strains. However, deformation of the mats and subgrade as the number of traffic passes increased created much more unpredictability in the panel movement, creating more exceptions to the theory that load applied closer to the joint yields higher magnitude strain. This observation is illustrated by the G46-G47 joint strains for passes 241-267 in Figure 7.9.

Figure 7.9. F-15E item G46-G47 panel joint strains for passes 241-267.



The maximum compressive and tensile strain values recorded for each gauge and traffic pass range are tabulated in Appendix B. Table 7.2 shows the average of these values, between 0 and about 20,000, and lists compressive or tensile for the highest average along with the percent difference between them. The compressive strain average was significantly higher than the tensile strain average for all working gauges, indicative of the load sharing between the locking bar and prongs when tensile strains are occurring at the gauge locations.

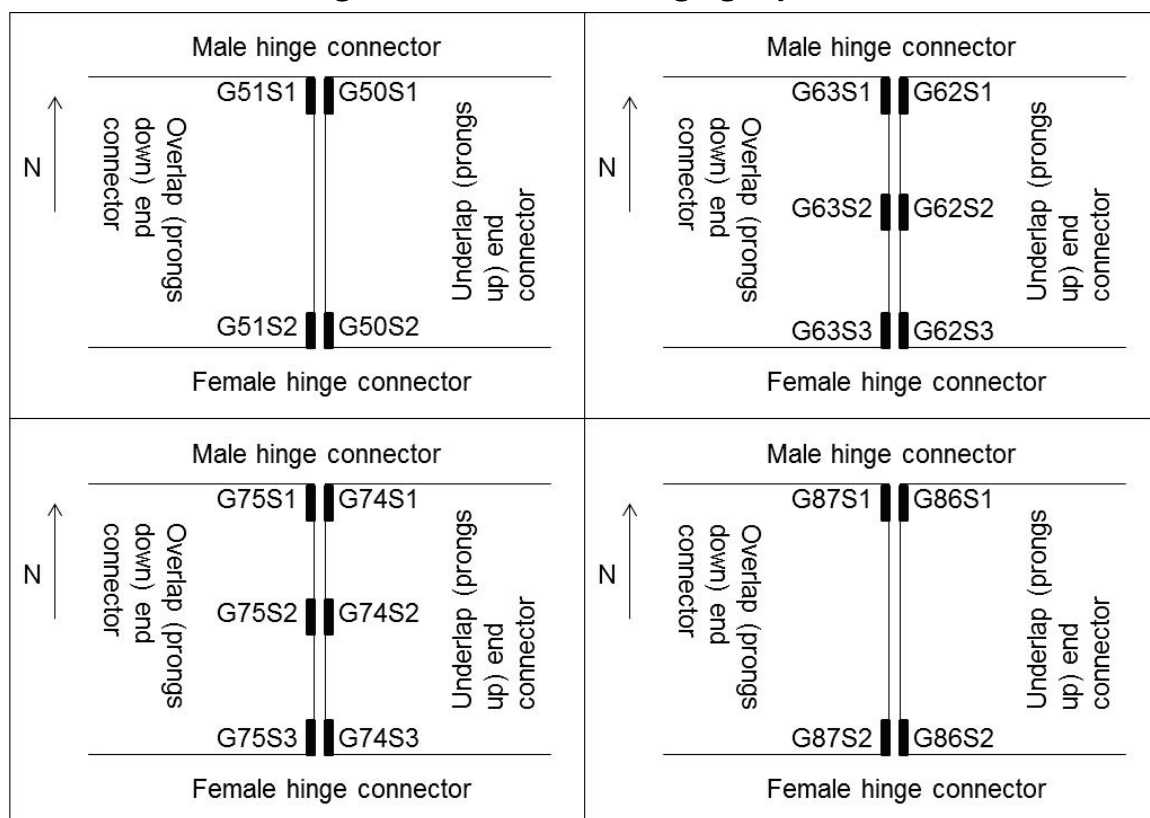
Table 7.2. F-15E item average maximum strains.

Panel Joint	Gauge	Stress	Max Strain (µε)	Average of Values >0 and <20,000 (µε)	Highest Average % Difference
G46-G47	G46S1	Compression	20,880	5,682	Compressive
		Tension	21,927	1,498	279%
	G46S2	Compression	20,734	4,305	Compressive
		Tension	21,771	1,101	291%
	G47S1	Compression	6,449	3,939	Compressive
		Tension	3,711	1,712	130%
	G47S2	Compression	5,418	3,991	Compressive
		Tension	3,514	1,668	139%
G58-G59	G58S1	Compression	20,829	2,742	Compressive
		Tension	21,921	562	388%
	G58S2	Compression	20,826	3,044	Compressive
		Tension	21,907	1,438	112%
	G58S3	Compression	20,738	5,892	Compressive
		Tension	21,778	453	1201%
	G59S1	Compression	20,784	3,968	Compressive
		Tension	2,960	1,862	113%
	G59S2	Compression	20,860	5,086	Compressive
		Tension	3,585	1,351	276%
	G59S3	Compression	5,197	2,737	Compressive
		Tension	1,988	578	373%
G70-G71	G70S1	Compression	7,635	5,760	Compressive
		Tension	3,493	1,497	285%
	G70S2	Compression	5,868	4,825	Compressive
		Tension	2,272	1,076	348%
	G70S3	Compression	10,468	6,899	Compressive
		Tension	1,626	1,057	553%
	G71S1	Compression	5,647	3,916	Compressive
		Tension	1,855	1,337	193%
	G71S2	Compression	4,419	3,301	Compressive
		Tension	682	331	898%
	G71S3	Compression	Bad Data		
		Tension	Bad Data		
G82-G83	G82S1	Compression	6,576	5,392	Compressive
		Tension	3,093	1,179	358%
	G82S2	Compression	7,126	5,607	Compressive
		Tension	1,770	1,147	389%
	G83S1	Compression	3,668	2,650	Compressive
		Tension	3,021	1,974	34%
	G83S2	Compression	5,909	5,296	Compressive
		Tension	1,606	896	491%

7.1.3 C-17 item

The strain gauge layouts for the C-17 instrumented panel joints are shown in Figure 7.10. Wheel locations relative to the instrumented joints during one pattern (i.e., 28 passes) are shown in Figure 7.11. These locations are also in Table 7.3, which includes the calculated percentage of the total loaded tire widths east and west of the instrumented panel joints. The LF/LR and CF/CR, as noted in Figure 7.11, are treated as one single, tandem load distribution.

Figure 7.10. C-17 item strain gauge layouts.



The loads and movements on the panels are much more complicated and unpredictable for the 6-wheel C-17 load cart than the single wheel F-15E load cart. Adding to the complexity is the fact that there are significant wheel loads on the panels north and south of an instrumented joint, as illustrated in Figure 7.12 for the first pass of each 28-pass cycle. The male-female hinge connection (Figure 2.2b) provides essentially the same level of vertical load transfer regardless of which panel has the higher load.

Figure 7.11. C-17 wheel placement relative to instrumented joints.

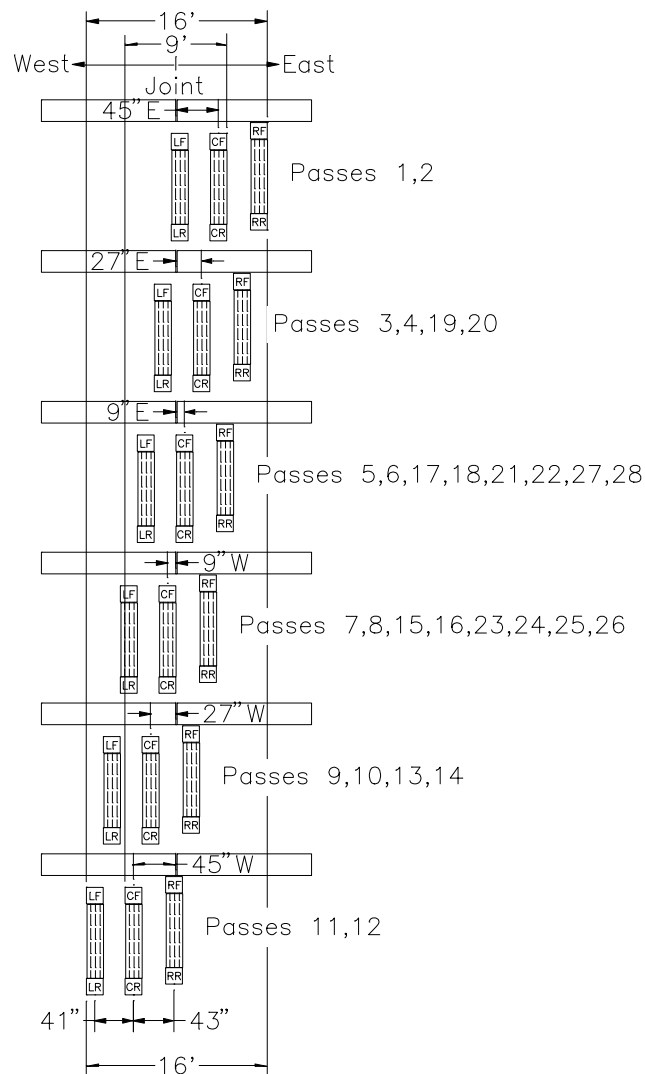
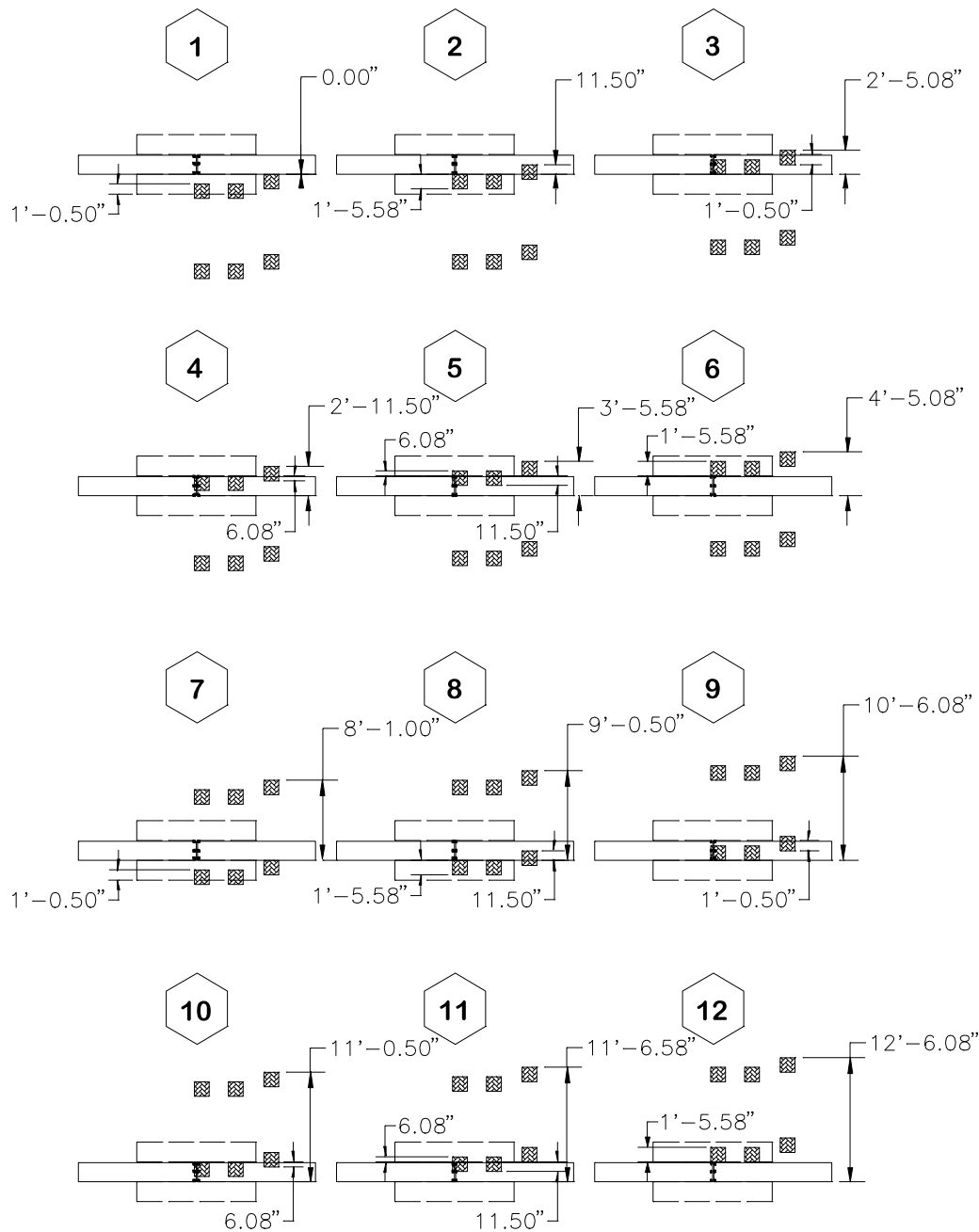


Table 7.3. C-17 wheel load distribution relative to instrumented joints.

Passes	Wheel Centerline Location Relative to Panel Joint (in.)						% of Total Loaded Tire Widths			
	LF/LR		CF/CR		RF/RR		LF/LR with CF/CR		RF/RR	
	East	West	East	West	East	West	East ^a	West ^a	East ^a	West ^a
1,2	4	—	45	—	88	—	86%	14%	100%	0
3,4,19,20	—	14	27	—	70	—	50%	50%	100%	0
5,6,17,18,21,22,25,26	—	32	9	—	52	—	50%	50%	100%	0
7,8,15,16,23,24,27,28	—	50	—	9	34	—	0	100%	100%	0
9,10,13,14	—	68	—	27	16	—	0	100%	100%	0
11,12	—	86	—	45	—	2	0	100%	39%	61%

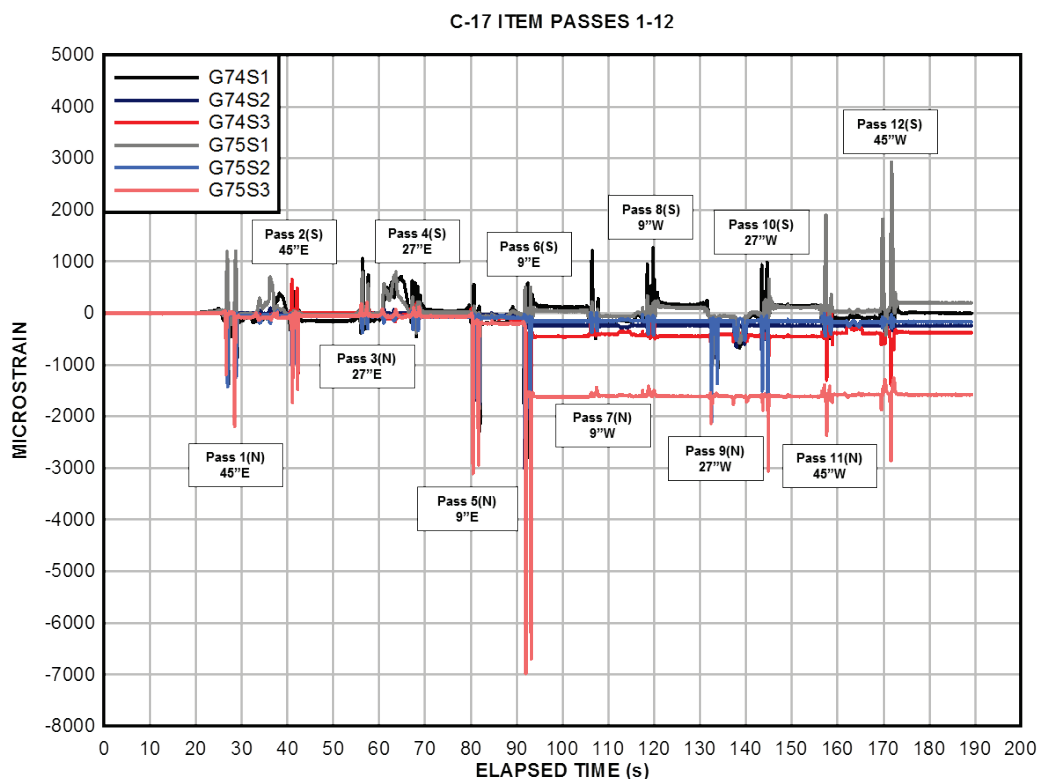
^a Relative to joint.

Figure 7.12. Northbound C-17 load cart wheel progression, pass 1.



The G74-G75 panel joint strains in Figure 7.13 for the first 12 C-17 passes do not show a clear correlation between strain magnitude and proximity to the joint. The strain gauge measurement range was approximately $\pm 20,000$ microstrain. Measured values outside this range were indicative of gauge failure and gauge failures correlated well with the observed mat breakage results validating that the strain gauge range was appropriate.

Figure 7.13. C-17 item G74-G75 panel joint strains for passes 1-12.



The pass 1 (northbound) and pass 2 (southbound) subset of the same data is shown in Figure 7.14. During these passes the load cart center wheels were centered approximately 45 in. east of the joint on Panel G74. Pass 2 panel movements predicted from the pass 1 strain data are not supported by the measured pass 2 strains, and vice versa. The unpredictability of the data was evident throughout the trafficking. The four highest strain magnitudes in the G74-G75 joint for passes 113-140 (Figure 7.15) occurred when the center wheels' line was 27 in. east, 45 in. west, 9 in. west and 9 in. east of the joint.

The maximum compressive and tensile strain values recorded for each gauge and traffic pass range are tabulated in Appendix C. Table 7.4 shows the average of these values, between 0 and about 20,000, and lists compressive or tensile strains for the highest average along with the percent difference between them. The compressive strain average was significantly higher than the tensile strain average for 18 of the 19 working gauges, indicative of the load sharing between the locking bar and prongs when tensile strains are occurring at the gauge locations.

Figure 7.14. C-17 item G74-G75 panel joint strains for passes 1-2.

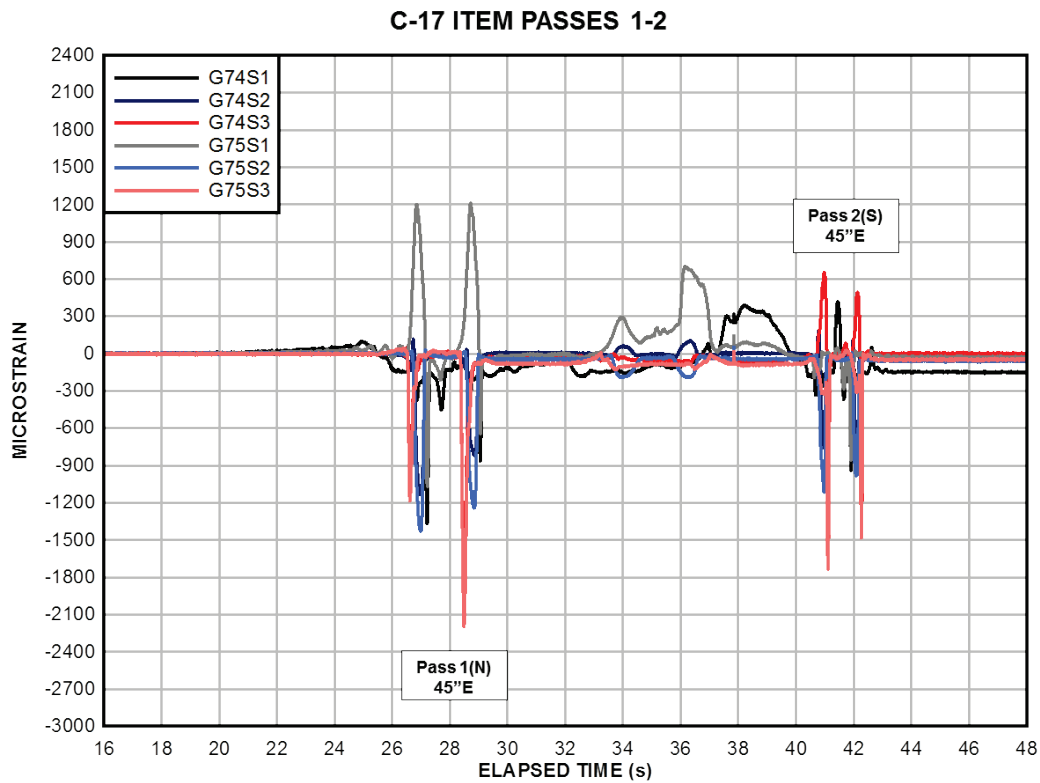


Figure 7.15. C-17 item G74-G75 panel joint strains for passes 113-140.

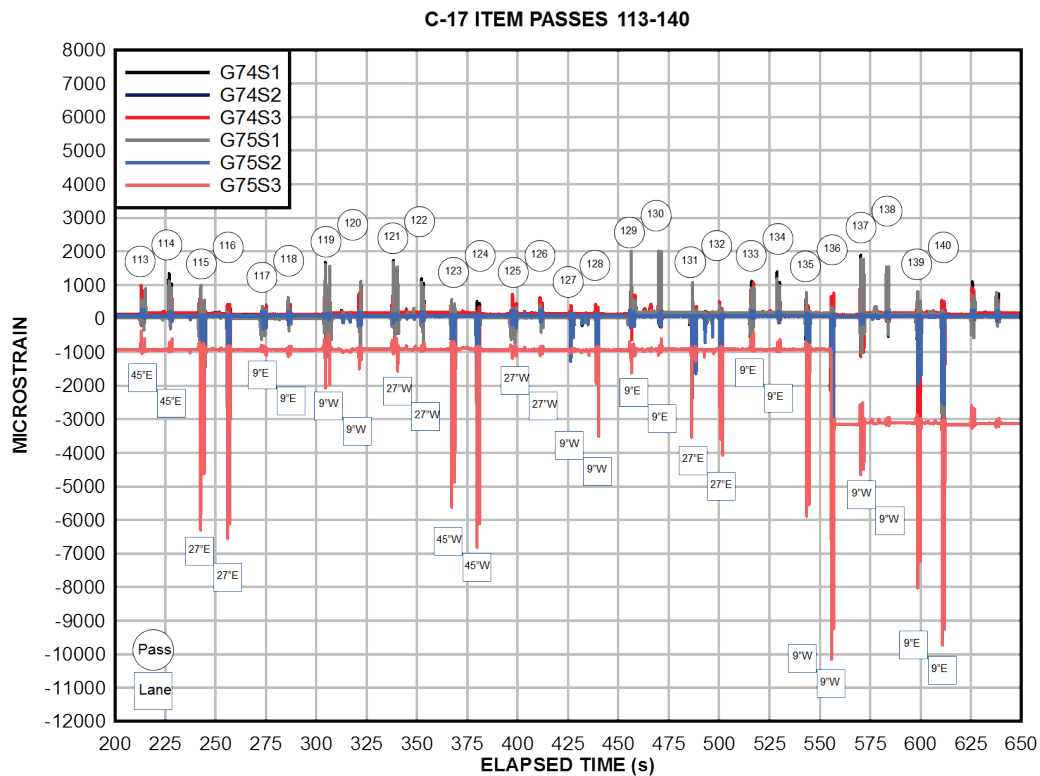


Table 7.4. C-17 item average maximum strains.

Panel Joint	Gauge	Stress	Max Strain ($\mu\epsilon$)	Average of Values >0 and <20,000 ($\mu\epsilon$)	Highest Average % Difference
G50-G51	G50S1	Compression	20,814	883	Compressive
		Tension	21,856	786	12%
	G50S2	Compression	20,677	6,660	Compressive
		Tension	21,715	532	1153%
	G51S1	Compression	20,759	1,904	Tensile
		Tension	21,827	2,785	46%
	G51S2	Compression	20,892	3,296	Compressive
		Tension	21,872	794	315%
G62-G63	G62S1	Compression	20,780	3,337	Compressive
		Tension	21,866	1,501	122%
	G62S2	Compression	20,780	2,717	Compressive
		Tension	21,859	1,322	106%
	G62S3	Compression	20,698	5,675	Compressive
		Tension	21,727	823	590%
	G63S1	Compression	Bad Data		
		Tension	Bad Data		
	G63S2	Compression	5,866	2,879	Compressive
		Tension	6,679	1,228	135%
	G63S3	Compression	5,227	4,280	Compressive
		Tension	2,816	1,179	263%
G74-G75	G74S1	Compression	3,935	2,920	Compressive
		Tension	3,011	1,452	101%
	G74S2	Compression	3,233	2,585	Compressive
		Tension	426	312	729%
	G74S3	Compression	5,062	4,450	Compressive
		Tension	1,488	968	360%
	G75S1	Compression	3,977	3,013	Compressive
		Tension	2,928	2,083	45%
	G75S2	Compression	9,189	3,887	Compressive
		Tension	5,741	994	291%
	G75S3	Compression	10,155	6,243	Compressive
		Tension	3,745	837	646%
G86-G87	G86S1	Compression	4,164	3,112	Compressive
		Tension	4,226	2,132	46%
	G86S2	Compression	4,884	4,207	Compressive
		Tension	2,315	1,029	309%
	G87S1	Compression	4,109	3,446	Compressive
		Tension	3,043	1,803	91%
	G87S2	Compression	20,928	4,734	Compressive
		Tension	21,789	775	511%

7.2 Analysis

Strain gauges performed well in this test. They recorded data throughout the test and aided in linking a measured strain to rail failures.

7.2.1 F-15E-V item

Compressive strains were comparatively higher than tensile strains throughout the test, where tensile strains remained under 3,000 microstrain and compressive strains were normally between 3,000 and 5,000 microstrain.

The strain gauges for the upper underlap (UU) and lower overlap (LO) shown in Figure 3.8 measure local flexural strains for each prong. The prong thickness measurements for five full length mats not used during the testing, are shown in Table 7.5. The assumption was made that each prong behaves as a cantilever beam with a 0.2-in. nominal thickness and a middepth neutral axis. This assumption makes the strain magnitude, not the type (compressive or tensile), the key measurement. A measured UU or LO compressive strain also reflects an equal magnitude tensile stress on the opposite side of the prong with this assumed behavior.

Table 7.5. Prong thickness for five panels.

Prong	Thickness (in.)					Average
	1	2	3	4	5	
UU	0.202	0.213	0.202	0.193	0.188	0.200
LO	0.197	0.211	0.219	0.195	0.195	0.205
Overall Average						0.202
Standard Deviation						0.010

The material strength properties for 6061-T6 aluminum are shown with a corresponding engineering stress-strain curve in Figure 7.16a. The same data truncated to 10,000 microstrain is shown in Figure 7.16b. The majority of the maximum measured strains from Table 7.1 are in the elastic range with just 3 of 15 slightly into the plastic region.

The first strain gauge to fail was F81S2 after pass 216, and an upper prong break at this location was the first mat failure observed when trafficking paused after pass 240. The F81S2 peak magnitude strain data is shown in Figure 7.17. Strain amplitude is a key parameter in predicting material fatigue. Yahr (1997) validated Equation 1 below with 6061-T6 test data, where N is the predicted number of cycles to failure.

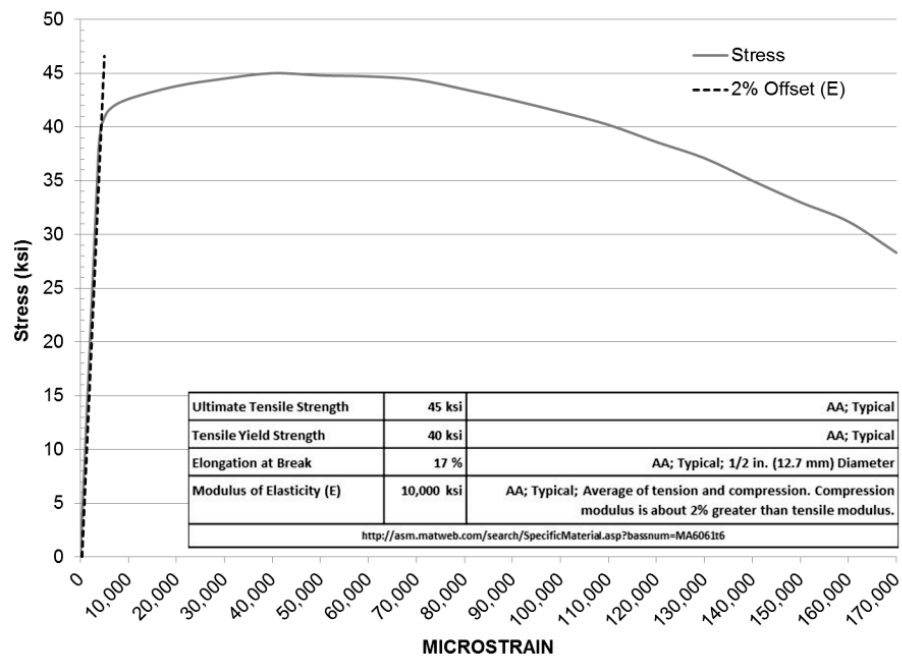
$$\text{Strain Amplitude} * E = \frac{2,100,000}{\sqrt{N}} + 14,000 \text{ psi} \quad (1)$$

The predicted passes/cycles using Figure 7.17 data (2,669 microstrain amplitude) as an approximation for the cyclic strain is 27,385, much higher than the 216 passes observed from the test. This is not surprising since the strain gauges were located approximately 1.5 in. away from the end of the prongs, the points that experience the highest stress and strain during trafficking. The fact that this strain gauge failed without recording a strain outside the elastic range is most likely indicative of a failure initiated by crack propagation from the end and base of the prong, transverse to the panel.

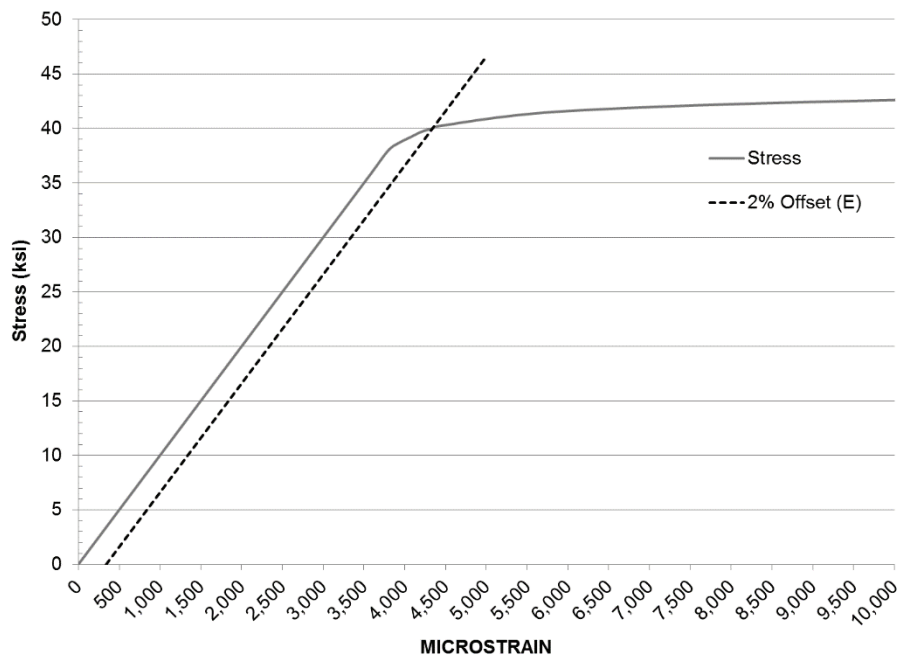
Figure 7.18a shows F81-F82 strains during the first traffic pass, 18 in. east of the joint. The vertical dashed lines represent the north and south hinge edges using the F81S1 and F81S2 strain peaks to establish the load cart speed, then calculating the time to travel the 2.5-in. distance from the hinge edges to each strain gauge location. The 9-in.-wide tire footprint has a 12.05-in. north-south dimension for a 35,235-lb load and 325-psi tire pressure. This 12.05-in. dimension equates to a 0.53-sec tire load duration footprint for pass 1, 18 in. east of the F81-F82 joint. Figure 7.18b shows tire load duration footprint locations, centered on the time when gauge F81S2 first measured a rising strain ①, peak strain was recorded ② and at the panel midpoint ③.

Figure 7.18 illustrates that load is transferred across the transverse joints well before the wheel hits the joint. The absence of an appreciable strain when the tire is centered on the panel confirms that the joints see the highest loads when the panels are eccentrically loaded. Each of these behaviors makes it difficult to accurately estimate an effective width for the cantilevered prongs and calculate a corresponding load or moment for a measured strain/stress.

Figure 7.16. (a) Material strength properties for 6061-T6 aluminum alloy and (b) same data truncated to 10,000 microstrain.



(a)



(b)

Figure 7.17. Strain amplitude for gauge F81S2.

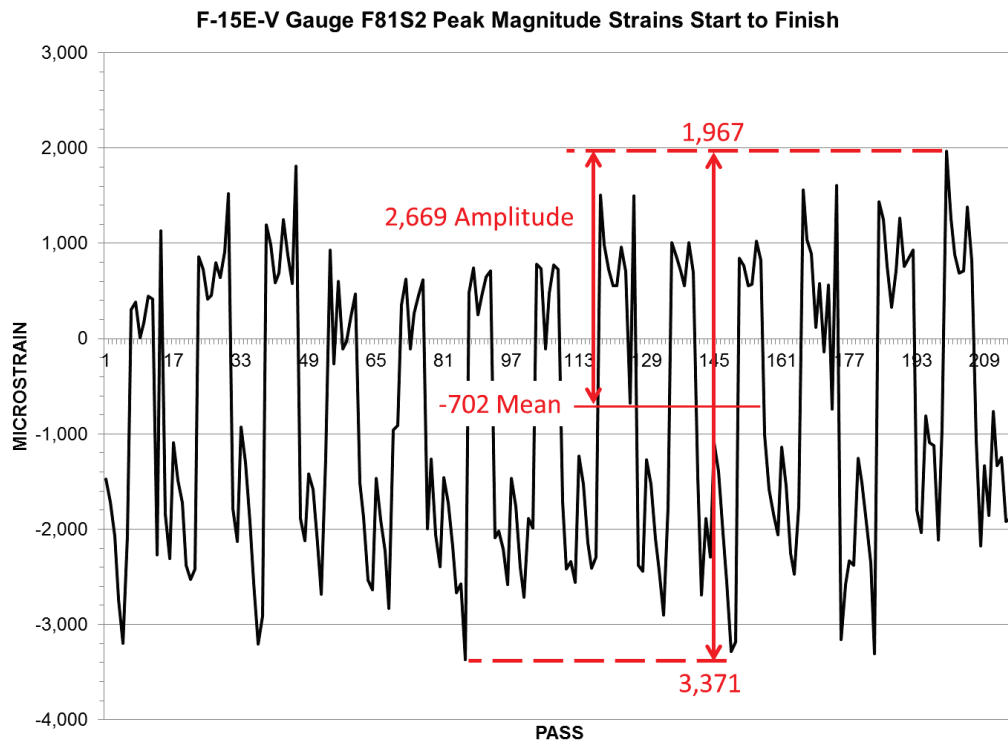
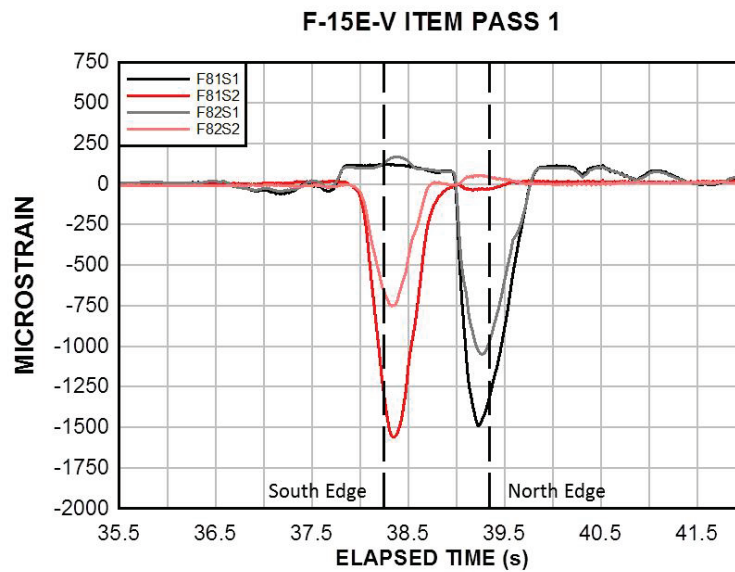
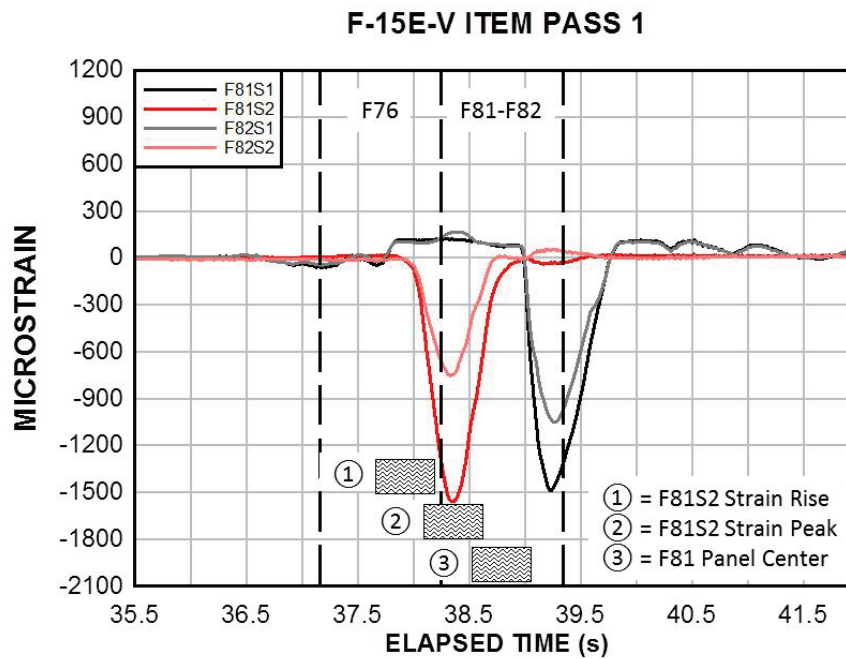


Figure 7.18. (a) F81-F82 joint strain data during pass 1 and (b) tire load footprint locations.



(a)



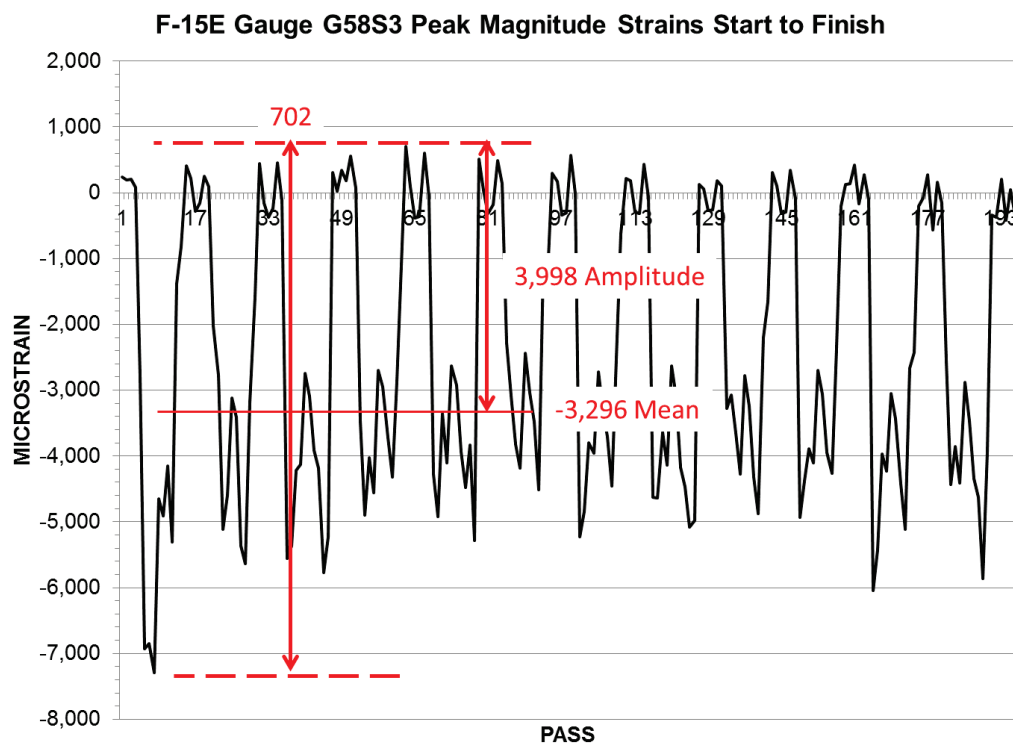
(b)

7.2.2 F-15E item

Compressive strains were comparatively higher than tensile strains throughout the test, where tensile strains remained under 5,000 microstrain and compressive strains remained under 10,000 microstrain.

Recall Figure 7.16 with material strength properties for 6061-T6 aluminum. Of the 19 maximum measured strains shown in Table 7.2, nine were in the plastic region. One of the first strain gauges to fail was G58S3 after pass 196, and an upper prong break at this location was the first mat failure observed when trafficking paused after pass 240. The G58S3 peak magnitude strain data are shown in Figure 7.19.

Figure 7.19. Strain amplitude for gauge G58S3.



From Equation 1 (Yahr 1997), the predicted passes/cycles using the Figure 7.19 data (3,998 microstrain amplitude) as an approximation for the cyclic strain is 6,634, much higher than the 196 passes observed from the test result. This is not surprising since the strain gauges were located approximately 1.5 in. away from the end of the prongs, the points that experience the highest stress and strain during trafficking.

Figure 7.20 shows a failure in the female hinge edge transferring load between G58 and G53. The highest G58S3 strains occurred in the first 16-pass cycle and then dropped by 18 to 35 percent before failing. Failure in the female hinge is the most likely cause for this reduction at the strain gauge, transferring more load to the underlying clay on subsequent passes.

Figure 7.20. Joint of Panels G58 and G53.

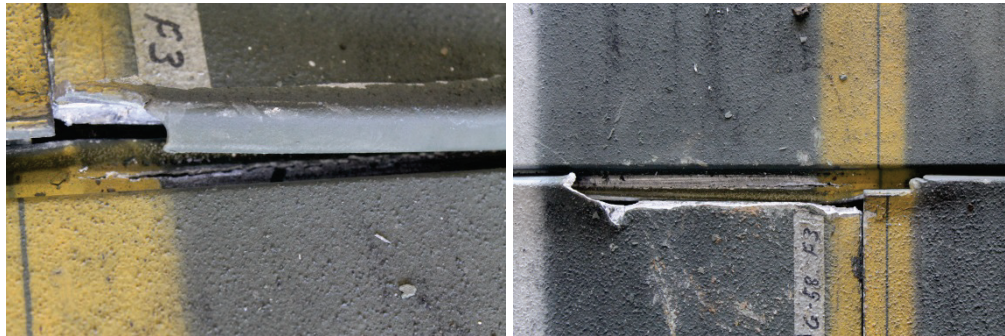
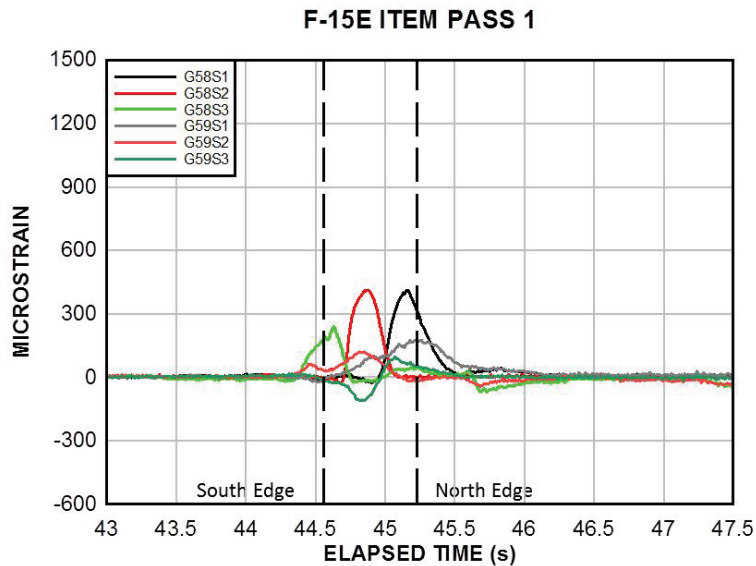


Figure 7.21a shows G58-G59 strains during the first traffic pass, 18 in. east of the joint. The vertical dashed lines represent the north and south hinge edges using the G58S1 and G58S3 strain peaks to establish the load cart speed, then calculating the time to travel the 2.5-in. distance from the hinge edges to each strain gauge location. The 9-in.-wide tire footprint has a 12.05-in. north-south dimension for a 35,235-lb load and 325-psi tire pressure. This 12.05-in. dimension equates to a 0.32-sec tire load duration footprint for pass 1, 18 in. east of the G58-G59 joint. Figure 7.21b shows tire load duration footprint locations, centered on the time when gauge F81S2 first measured a rising strain ①, peak strain was recorded ② and at the panel midpoint ③.

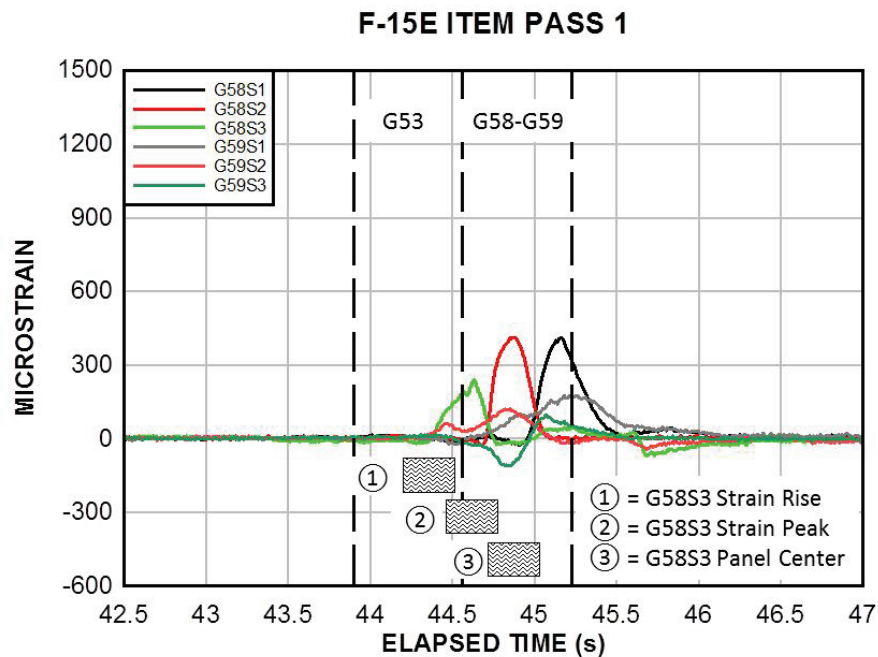
Figure 7.21 illustrates that load is transferred across the transverse joints well before the wheel hits the joint. The absence of an appreciable strain on the end gauges when the tire is centered on the panel confirms that the joint ends see the highest loads when the panels are eccentrically loaded. As expected, the center gauge records the peak strain when the wheel is centered on the panel. Each of these behaviors makes it difficult to accurately estimate an effective width for the cantilevered prongs and calculate a corresponding load or moment for a measured strain/stress.

Figure 7.21. (a) G58-G59 joint strain data during pass 1, and
(b) tire load footprint locations.



Pass	Peak Times		Delta (sec)	Speed (in./sec)	South Edge (sec)	North Edge (sec)
	G58S1 (sec)	G58S3 (sec)				
1	45.16	44.63	0.53	37.26	44.56	45.23

(a)

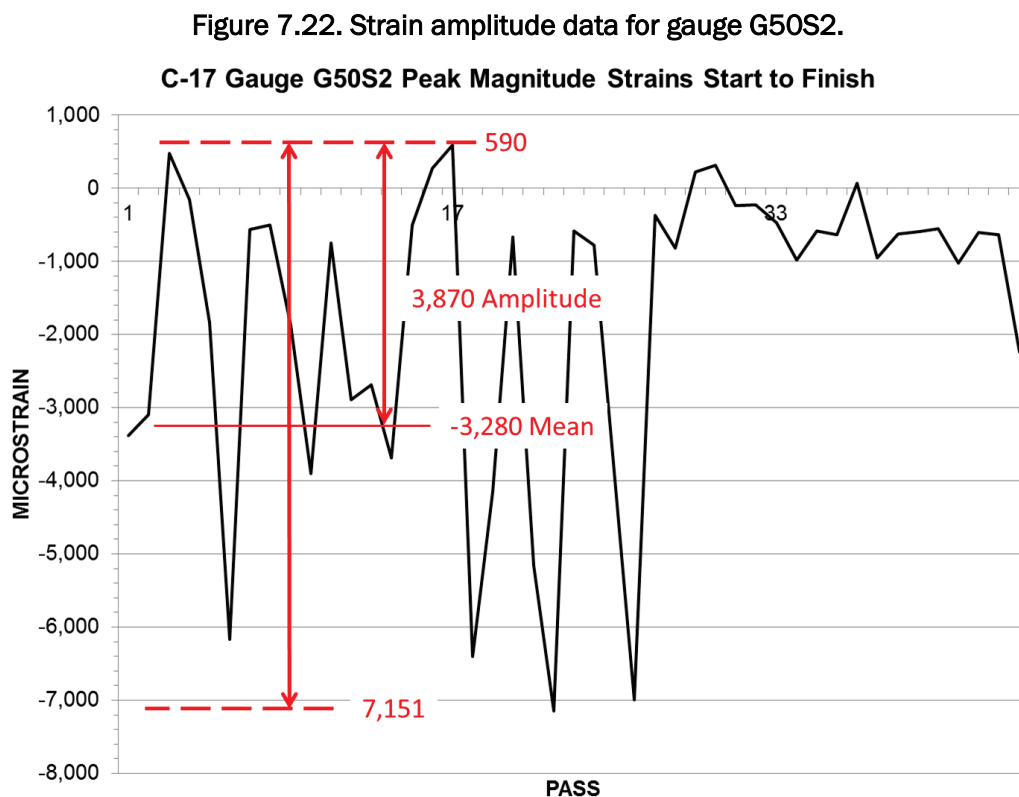


(b)

7.2.3 C-17 item

Compressive strains were comparatively higher than tensile strains throughout the test, where tensile strains remained under 5,000 microstrain and compressive strains remained under 8,000 microstrain.

Figure 7.16 shows material strength properties for 6061-T6 aluminum. Of the 19 measured strains shown in Table 7.4, nine were in the plastic region. One of the first strain gauges to fail was G50S2 after pass 45, and an upper prong break on this panel was the first mat failure observed when trafficking stopped after pass 168. The G50S2 peak magnitude strain data are shown in Figure 7.22



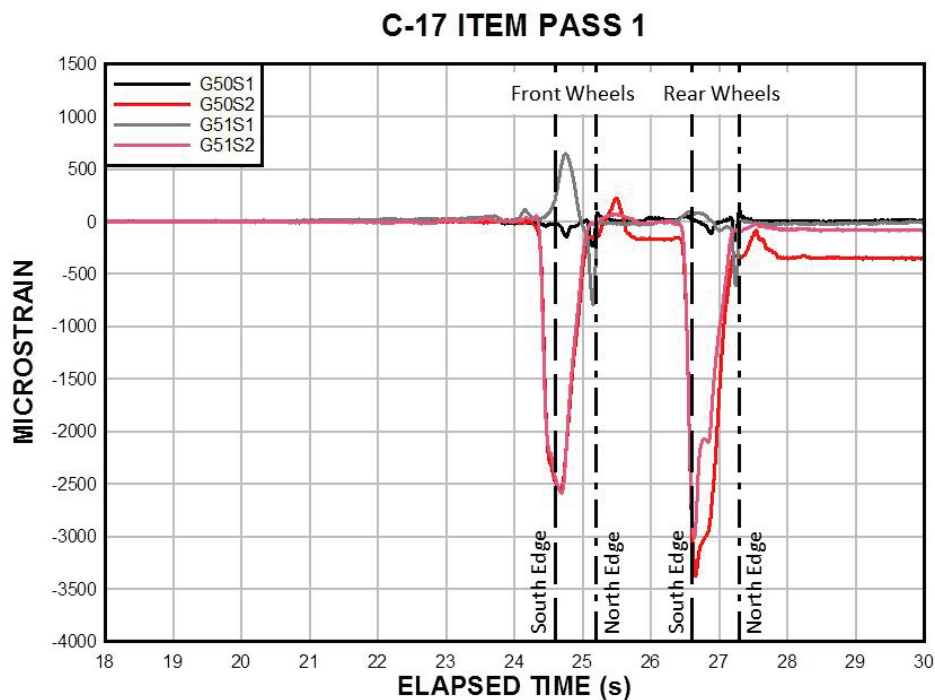
From Equation 1 (Yahr 1997), the predicted passes/cycles using the Figure 7.22 data (3,870 microstrain amplitude) as an approximation for the cyclic strain is 7,228, much higher than the 90 passes observed from the test result (45 passes, each with 2 loading cycles). This is not surprising since the strain gauges were located approximately 1.5 in. away from the end of the prongs, the points that experience the highest stress and strain

during trafficking. It is interesting to note that the measured strain magnitudes during the second 28-pass cycle were significantly lower than the first, yet the end result was a gauge failure and likely a material failure.

Figure 7.23 shows G50-G51 strains during the first traffic pass, 45 in. east of the joint. The vertical dashed lines represent the north and south hinge edges using the G50S1 and G50S2 strain peaks to establish front and rear wheel load cart speeds, then calculating the time to travel the 2.5-in. distance from the hinge edges to each strain gauge location.

The pronounced single data peak suggests that the offset lead and trailing two tires for each set of three wheels interact with the matting similar to a single axle of three wheels and a tire contact area larger than one wheel but less than two in line wheels. This graphic illustrates that load is transferred across the transverse joints well before the wheel hits the joint. It is not possible to determine accurate tire locations using the strain data or to accurately estimate an effective width for the cantilevered prongs and calculate a corresponding load or moment for a measured strain/stress.

Figure 7.23. G50-G51 joint strain data during pass 1.



Pass	Front Wheels		Back Wheels		Front	Back	Front	Back	Front Wheels	Back Wheels		
	Peak Times		Peak Times		Delta (sec)	Delta (sec)	Speed (in./sec)	Speed (in./sec)	South Edge (sec)	North Edge (sec)	South Edge (sec)	North Edge (sec)
	G50S1 (sec)	G50S2 (sec)	G50S1 (sec)	G50S2 (sec)								
1	25.14	24.66	27.23	26.65	0.48	0.58	41.15	34.05	24.60	25.20	26.59	27.29

8 Conclusions and Recommendations

The objectives of the effort described herein were to evaluate the AM2 brickwork pattern over a voided and non-voided subgrade with a CBR of 6. Two individual sections of matting were tested consecutively. The first consisted of one item with the mat placed over a subgrade with simulated voids and subjected to simulated F-15E traffic. The second section consisted of two items, one for simulated F-15E traffic and the other for simulated C-17 traffic. Permanent deformation and mat breakage were monitored, and strain data were recorded continuously. The results from the test section were compared to those documented in previous tests where AM2 was installed in a brickwork configuration. The information obtained from this evaluation will be used to validate the NAVAIR DIM model.

The following conclusions were derived from accelerated traffic testing of the AM2 airfield matting system conducted in July-August 2013.

8.1 Conclusions

- The AM2 brickwork pattern, when placed on a subgrade with voids, was able to sustain 240 passes before the first panel failure occurred. After 1,008 passes were reached, 4 panels failed and the permanent deformation criterion was exceeded, representing a reduction of 35 percent in terms of passes-to-failure when compared to baseline testing results. Due to information gathered after testing regarding a non-filleted corner in an area of high stress concentration at the end connector, it is difficult to conclude whether premature failure was a result of voids or a weak end connector design. Based on similar testing of AM2 on a voided subgrade, it is assumed that the latter case attributed significantly to performance.
- The AM2 brickwork pattern, when placed on a uniform subgrade, was able to sustain 240 passes of simulated F-15E traffic before the first panel failure. After 476 passes, 4 panels failed, and the deformation criterion was met, representing a reduction of 70 percent in terms of passes-to-failure when compared to baseline testing results.
- Results from the F-15E-V and F-15E items are conflicting since it was expected that the F-15E item would perform better and that voids on

the subgrade surface would have some effect on mat performance, even if not significant. An analysis of the repeatability of full-scale testing of AM2 and other airfield mat designs has been recommended by several researchers, including the authors of this report. Regardless, both items subjected to F-15E traffic failed prior to the baseline result of 1,500 passes. The information provided by Garcia et al. (2015b) verifies that the performance of all test items in this report was significantly affected by a weak end connector design. Although results may be skewed because of a manufacturing error, the data gathered are useful for conducting joint optimization studies and ensuring quality control practices by the AM2 producer.

- The AM2 brickwork pattern, when placed on a uniform subgrade, was able to sustain 308 passes of simulated C-17 traffic before failure due to mat breakage, representing a reduction of 80 percent in terms of passes-to-failure when compared to baseline testing results.
- The strain gauges placed in areas of high stress concentrations of the upper underlap and lower overlap end connector rails functioned as designed to monitor strains during trafficking. Gauge failures correlated well with observed mat breakage. Strain magnitude varied depending on the location and position of the aircraft simulator. For the test items subjected to F-15E traffic, an absence of appreciable strain when the tire is centered on the panel joints confirms that the end connector experiences the highest loads when the panels are eccentrically loaded. Compressive strains were generally higher, indicative of load sharing between the locking bar and rails.
- Caution should be used when attempting to apply standard metal fatigue models to airfield mat behavior under rolling wheel loads. Due to the complex nature of rolling wheel loads, basic fatigue models may not be applicable.

8.2 Recommendations

- Criteria established by NAWCADLKE-MISC-48J200-0011 (Naval Air Warfare Center 2006), although conservative, should continue to be used to avoid unexpected damage to the mat. Voids at or near joint locations should be avoided.

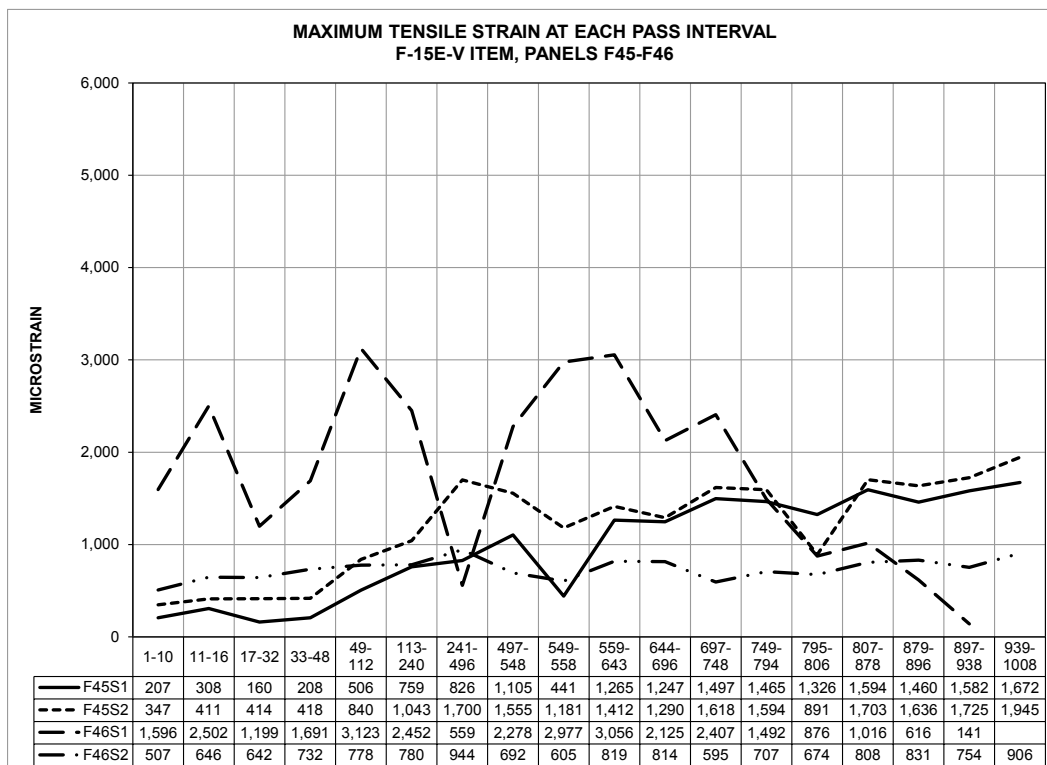
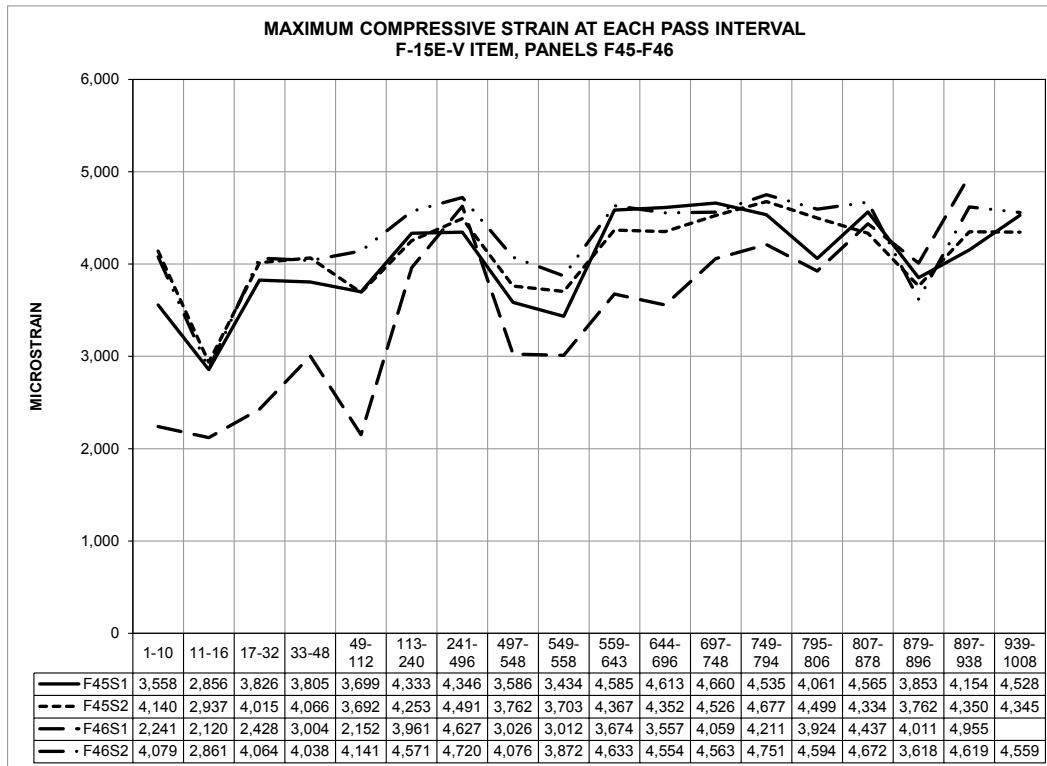
- Findings from this test are encouraging for performing joint optimization studies for the AM2 end connector. Strain data may be used to develop designs that improve load transfer.

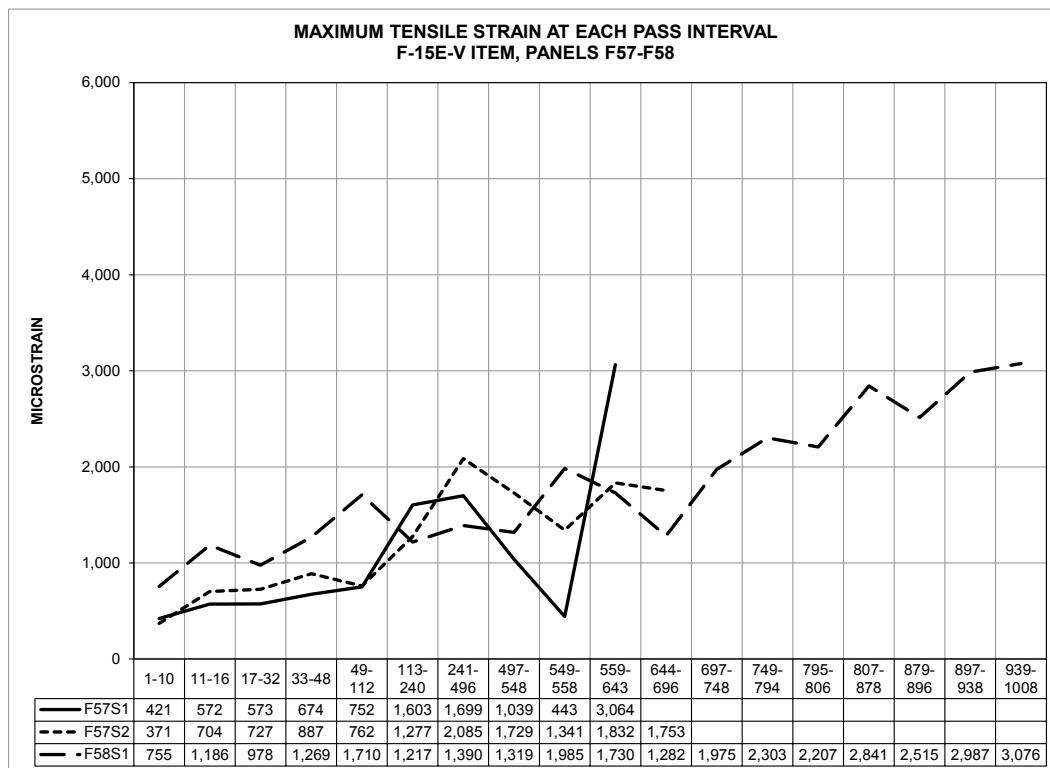
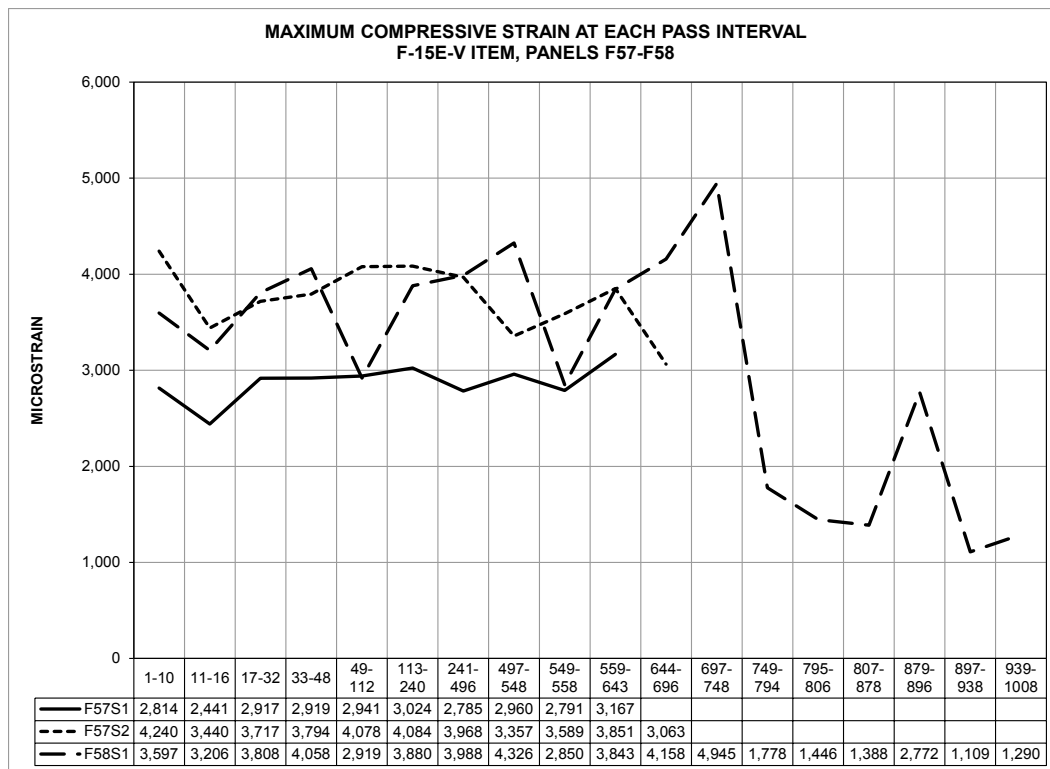
References

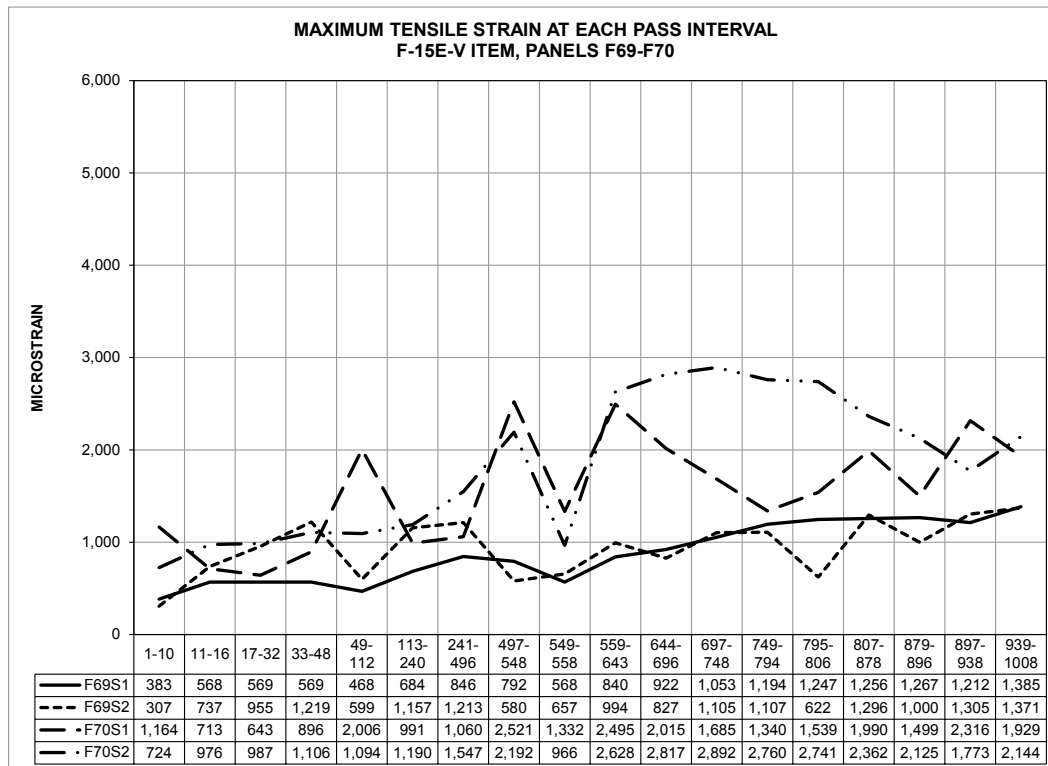
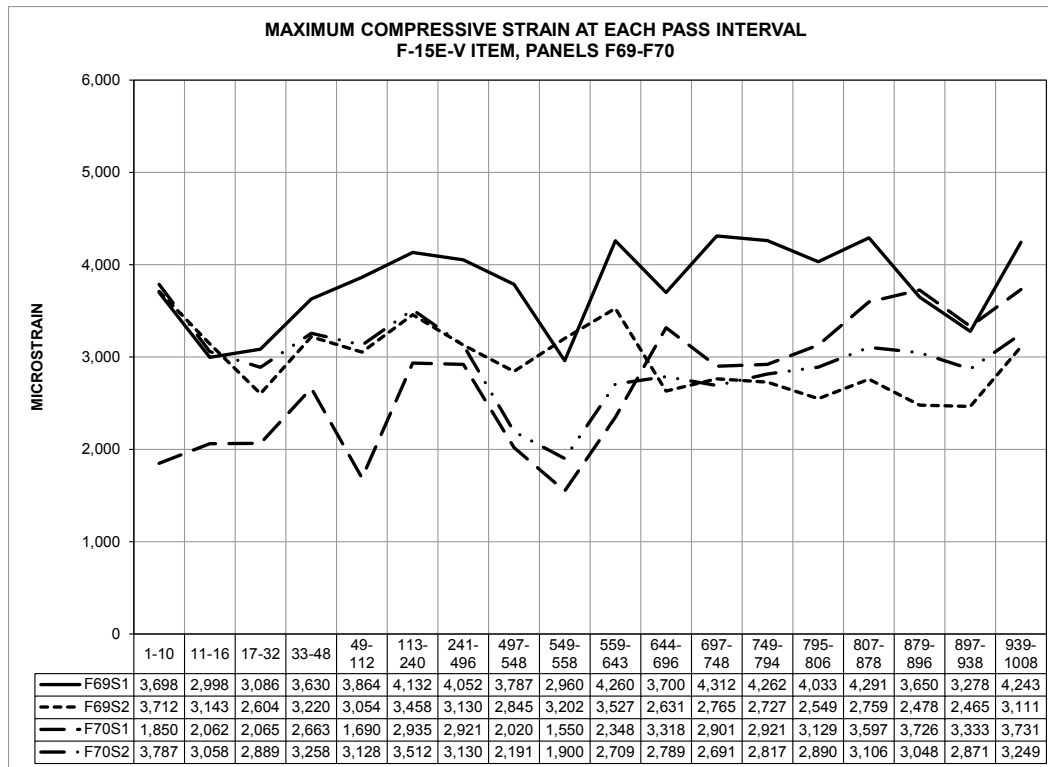
- ASTM International. 2007a. *Standard test method for California Bearing Ratio (CBR) of laboratory-compacted soils*. Standard D1883. West Conshohocken, PA: ASTM International.
- ASTM International. 2007b. *Standard test method for particle-size analysis of soils*. Standard D422. West Conshohocken, PA: ASTM International.
- ASTM International. 2008. *Standard test method for determination of water (moisture) content of soil by microwave oven heating*. Designation: D 4643-08. West Conshohocken, PA: ASTM International.
- ASTM International. 2009. *Standard test method for use of the dynamic cone penetrometer in shallow pavement applications*. Designation: D 6951. West Conshohocken, PA: ASTM International.
- ASTM International. 2010a. *Standard test method for in-place density and water content of soil and soil aggregate by nuclear methods (shallow depth)*. Standard D6938. West Conshohocken, PA: ASTM International.
- ASTM International. 2010b. *Standard test method for laboratory determination of water (moisture) content of soil and rock by mass*. Standard D2216. West Conshohocken, PA: ASTM International.
- ASTM International. 2011. *Standard practice for classification of soils for engineering purposes (Unified Soil Classification System)*. Standard D2487. West Conshohocken, PA: ASTM International.
- ASTM International. 2012. *Standard test methods for laboratory compaction characteristics of soil using modified effort (56,000 ft-lbf/ft³ (2,700 kN-m/m³))*. Standard D1557. West Conshohocken, PA: ASTM International.
- ASTM International. 2014. *Standard test methods for liquid limit, plastic limit, and plasticity index of soils*. Standard D4318. West Conshohocken, PA: ASTM International.
- Garcia, L. T., and T. W. Rushing. 2013. *AM2 sand subgrade sensitivity test*. ERDC/GSL TR-13-10. Vicksburg, MS: U.S. Army Engineer Research and Development Center.
- Garcia, L., T. W. Rushing, and Q. S. Mason. 2012. *Evaluation of webcore prototype AMX mat system*. ERDC/GSL TR-12-14. Vicksburg, MS: U.S. Army Engineer Research and Development Center.
- Garcia, L., T. W. Rushing, and Q. S. Mason. 2014a. *AM2 25 CBR subgrade sensitivity test*. ERDC TR-14-7. Vicksburg, MS: U.S. Army Engineer Research and Development Center.
- Garcia, L., T. W. Rushing, B. A. Williams, and C. A. Rutland. 2014b. *AM2 100 CBR subgrade sensitivity test*. ERDC TR-14-37. Vicksburg, MS: U.S. Army Engineer Research and Development Center.

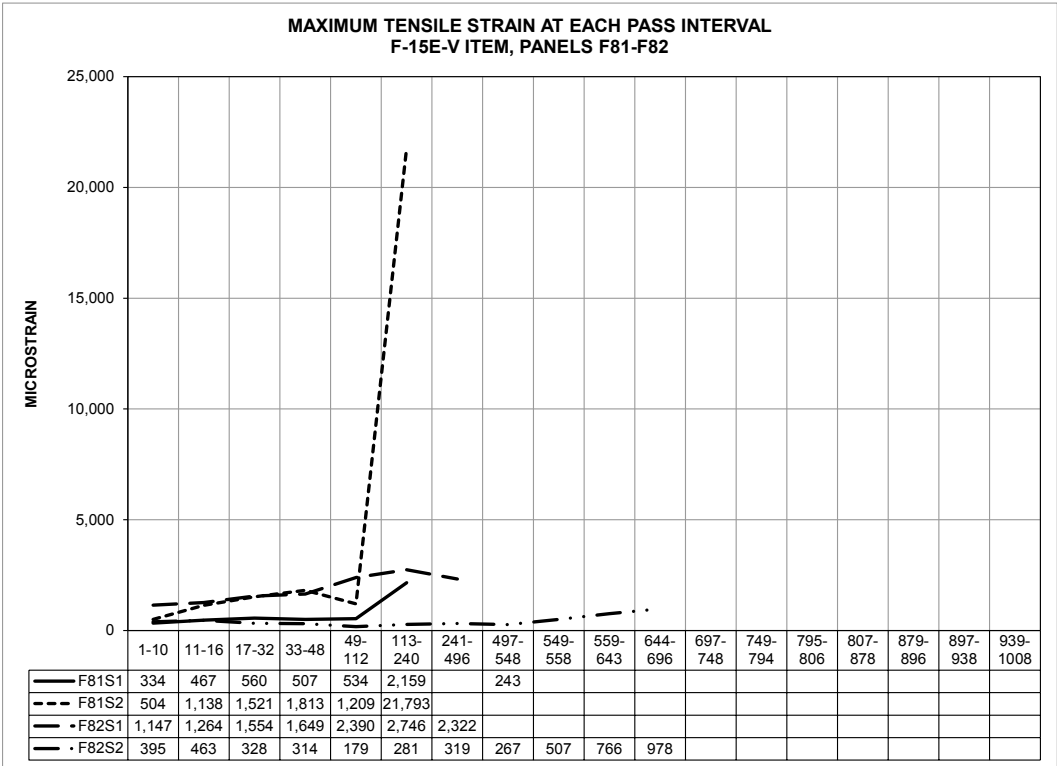
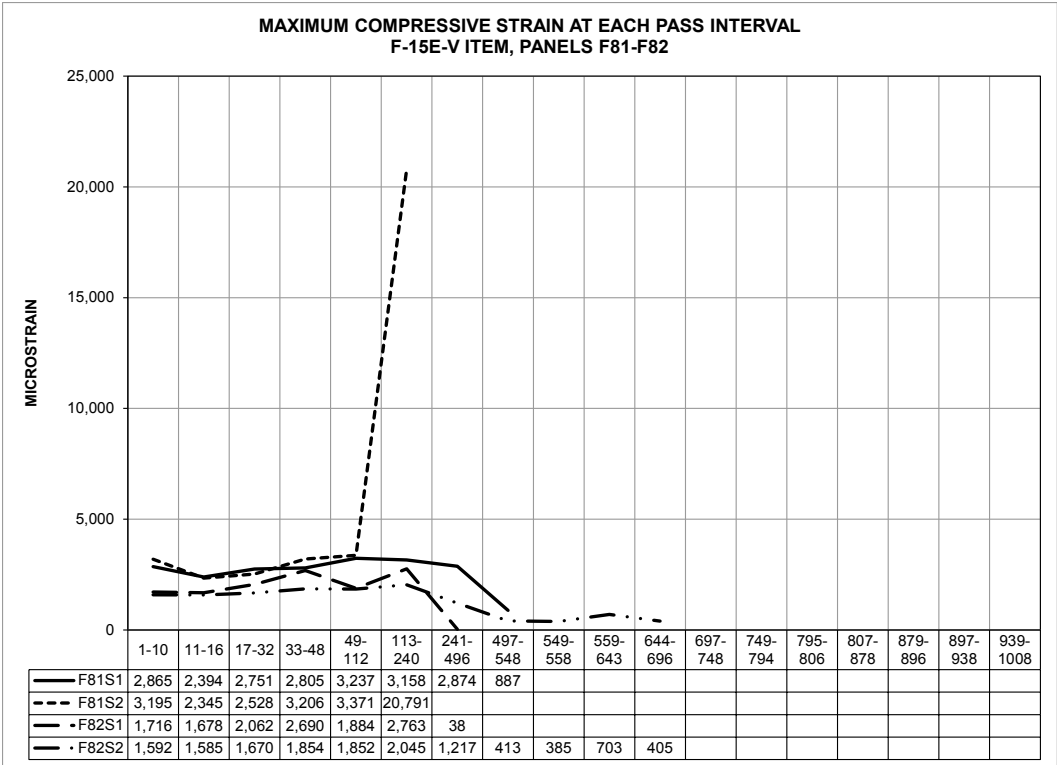
- Garcia, L., T. W. Rushing, and J. S. Tingle. 2015a. *AM2 brickwork pattern evaluation with refurbished matting*. ERDC TR-15-30. Vicksburg, MS: U.S. Army Engineer Research and Development Center.
- Garcia, L., T. W. Rushing, Q. Mason, J. S. Tingle, and C. A. Rutland. 2015b. *AM2 mat end connector modeling and performance validation*. ERDC TR-15-28. Vicksburg, MS: U.S. Army Engineer Research and Development Center.
- Garcia, L., W. Vanadit-Ellis, T. W. Rushing, J. S. Tingle, and C. A. Rutland. 2015c. *AM2 opposite lay evaluation*. ERDC TR-15-14. Vicksburg, MS: U.S. Army Engineer Research and Development Center.
- Naval Air Warfare Center. 2006. *Expeditionary airfield AM2 mat certification requirements*. NAWCADLKE-MISC-48J200-0011. Lakehurst, NJ: Naval Air Warfare Center, Aircraft Division.
- Rushing, T. W., and J. S. Tingle. 2007. *AM2 and M19 airfield mat evaluation for the rapid parking ramp expansion program*. ERDC/GSL TR-07-5. Vicksburg, MS: U.S. Army Engineer Research and Development Center.
- Rushing, T. W., and N. Torres. 2007. *Prototype mat system evaluation*. ERDC/GSL TR-07-29. Vicksburg, MS: U.S. Army Engineer Research and Development Center.
- Rushing, T. W., and Q. S. Mason. 2008. *AM2 15 CBR subgrade sensitivity test for the rapid parking ramp expansion program*. ERDC/GSL TR-08-25. Vicksburg, MS: U.S. Army Engineer Research and Development Center.
- Rushing, T. W., N. Torres, and Q. Mason. 2008. *AM2 10 CBR subgrade sensitivity test for the rapid parking ramp expansion program*. ERDC/GSL TR-08-13. Vicksburg, MS: U.S. Army Engineer Research and Development Center.
- Rushing, T. W., L. Garcia, and Q. S. Mason. 2011. *Large-scale 6-CBR prototype mat system evaluation for the AMX program*. ERDC/GSL TR-11-37. Vicksburg, MS: U.S. Army Engineer Research and Development Center.
- Rushing, T. W., L. Garcia, and Q. S. Mason. 2012. *Evaluation of faun aluminum mat systems*. ERDC/GSL TR-12-32, Vicksburg, MS: U.S. Army Engineer Research and Development Center.
- Rushing, T. W., L. Garcia, J. S. Tingle, P. G. Allison, and C. A. Rutland. 2014. *AM2 3-4 alternate lay pattern evaluation*. ERDC/GSL TR-14-38. Vicksburg, MS: U.S. Army Engineer Research and Development Center.
- U.S. Army Engineer Research and Development Center. 1995. *Standard test method for California Bearing Ratio of soils in place*. Designation: CRD-C654-95. Vicksburg, MS.
- Yahr, G. T. 1997. Fatigue design curves for 6061-T6 aluminum. *Journal of Pressure Vessel Technology* 119(2), 211-215.

Appendix A: F-15E-V Item Strain Gage Data Summary

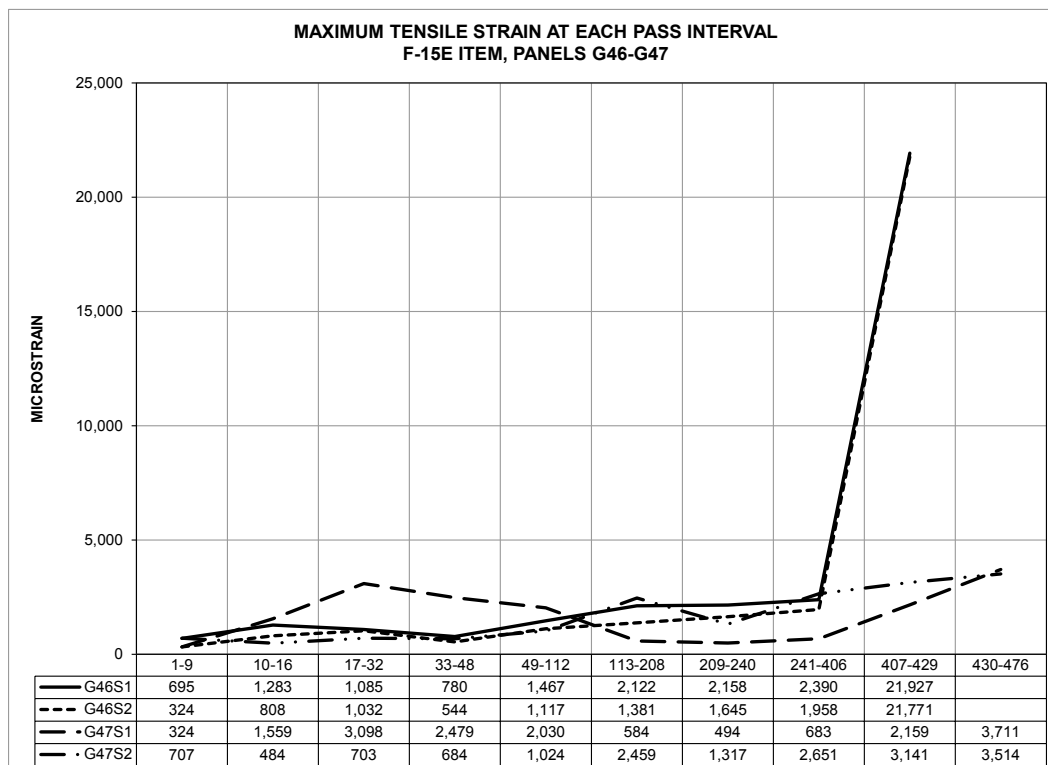
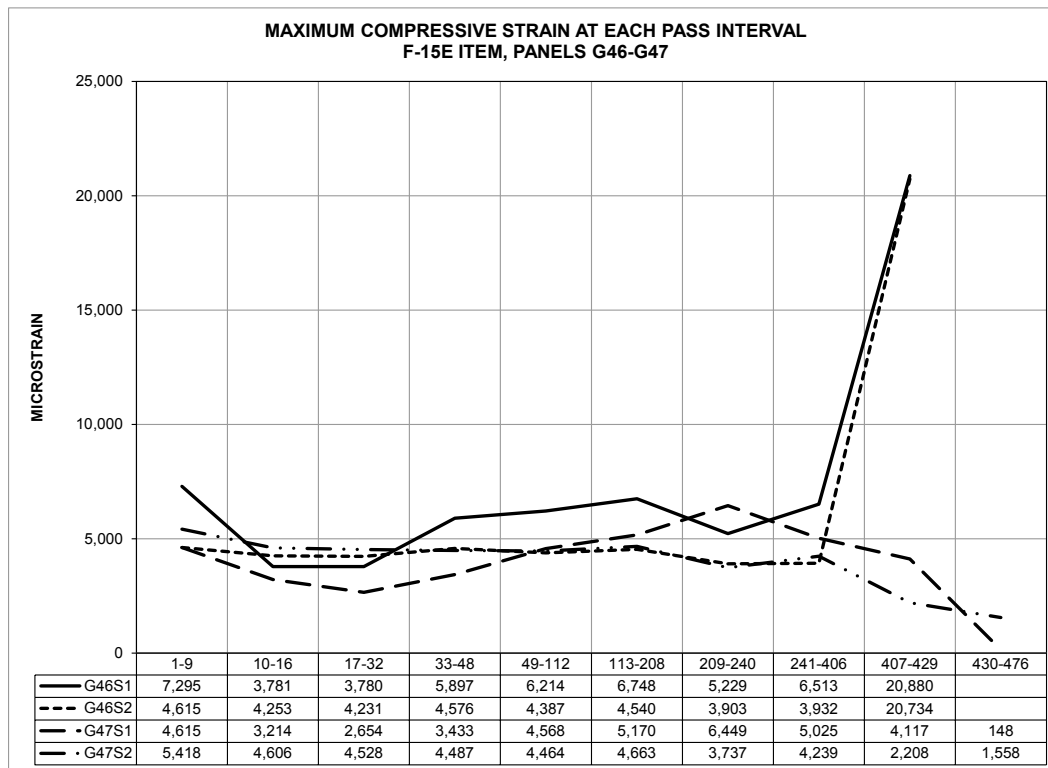


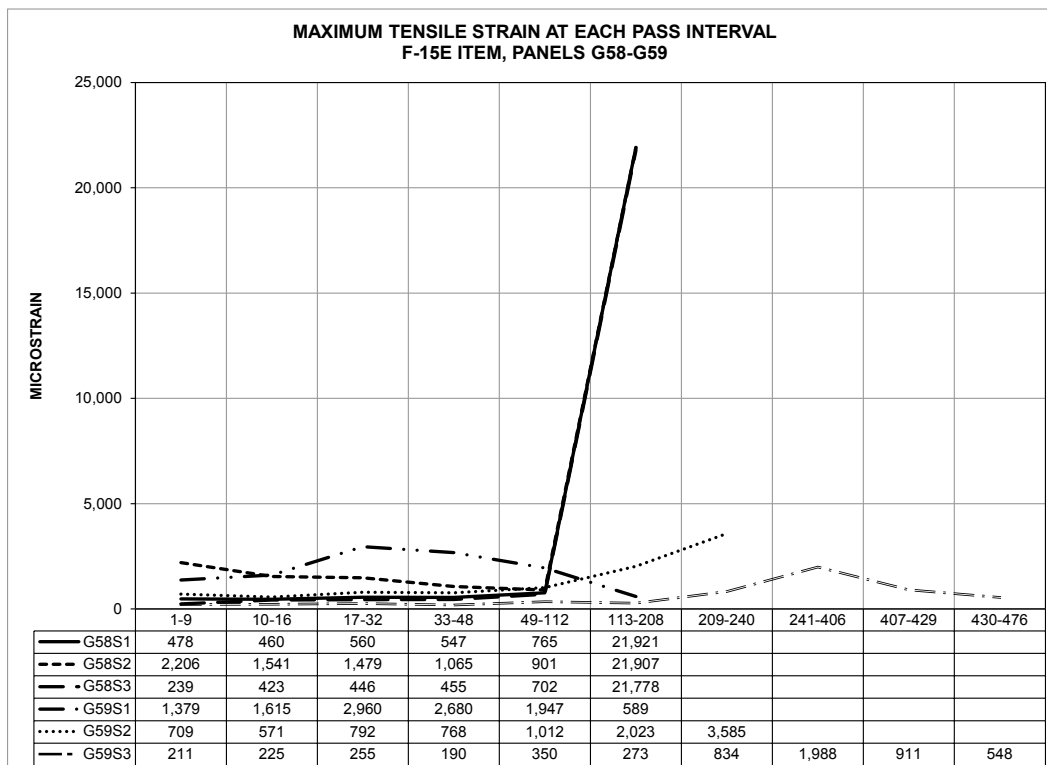
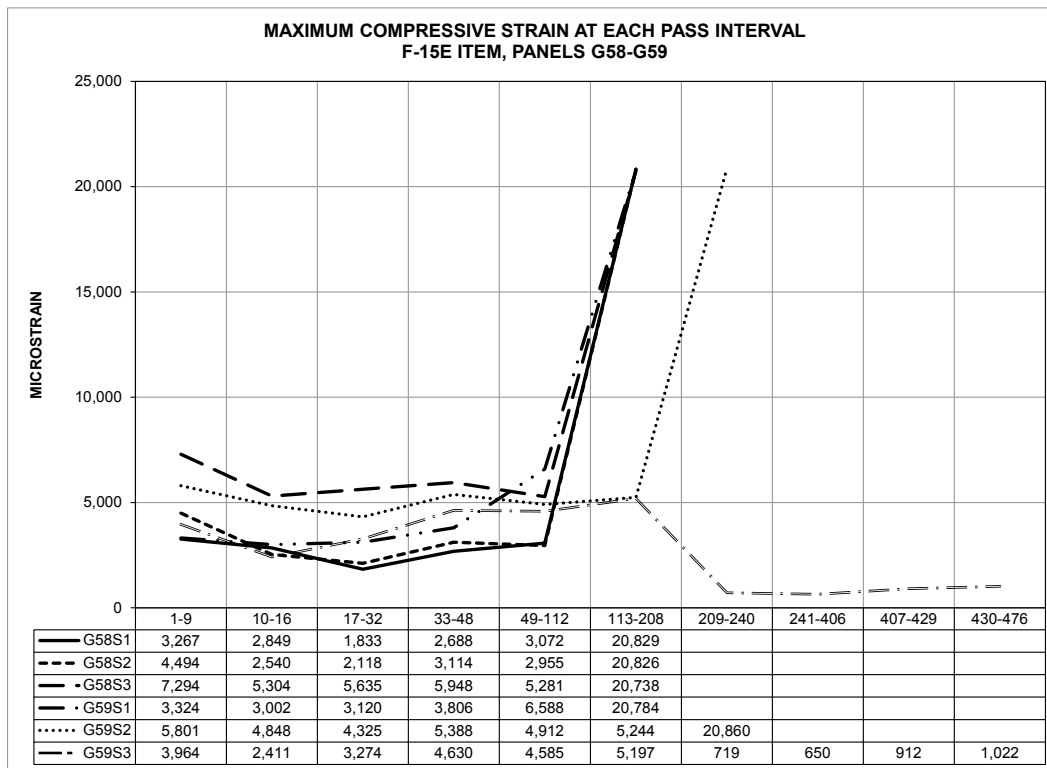


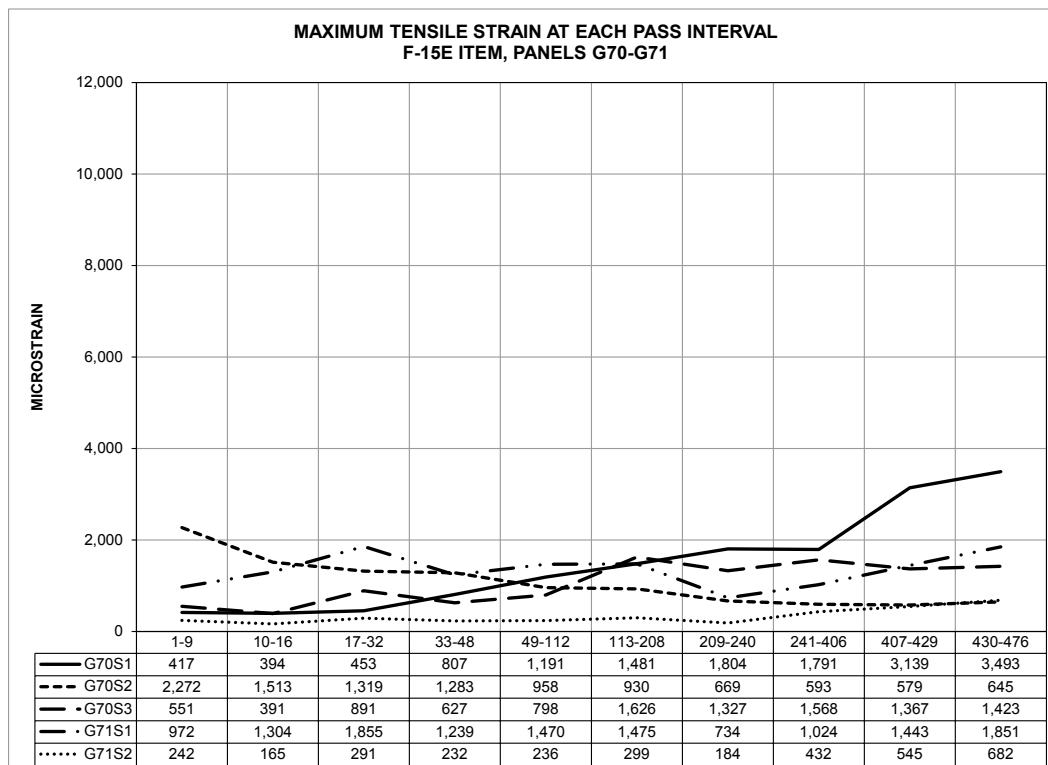
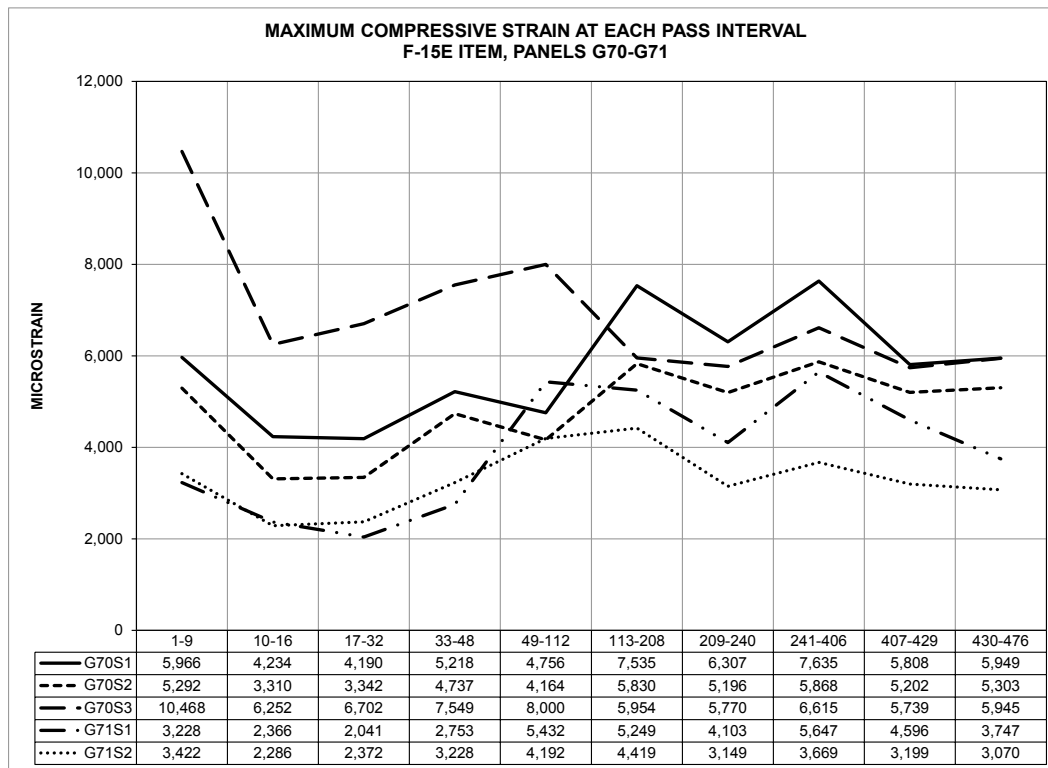


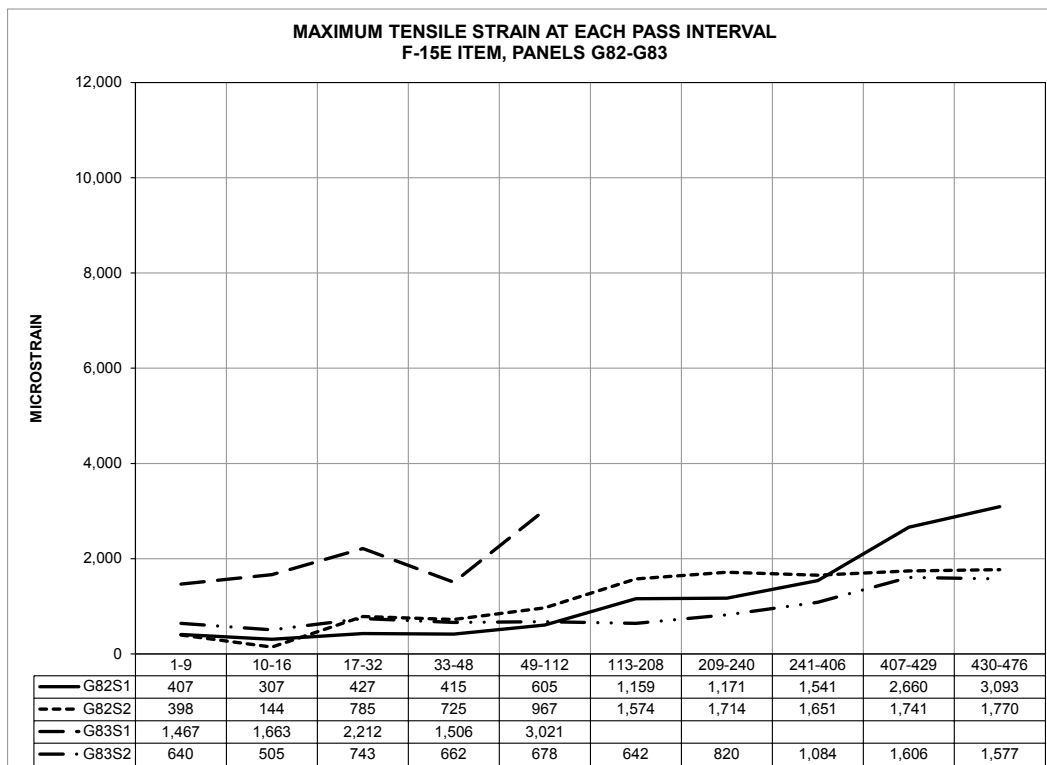
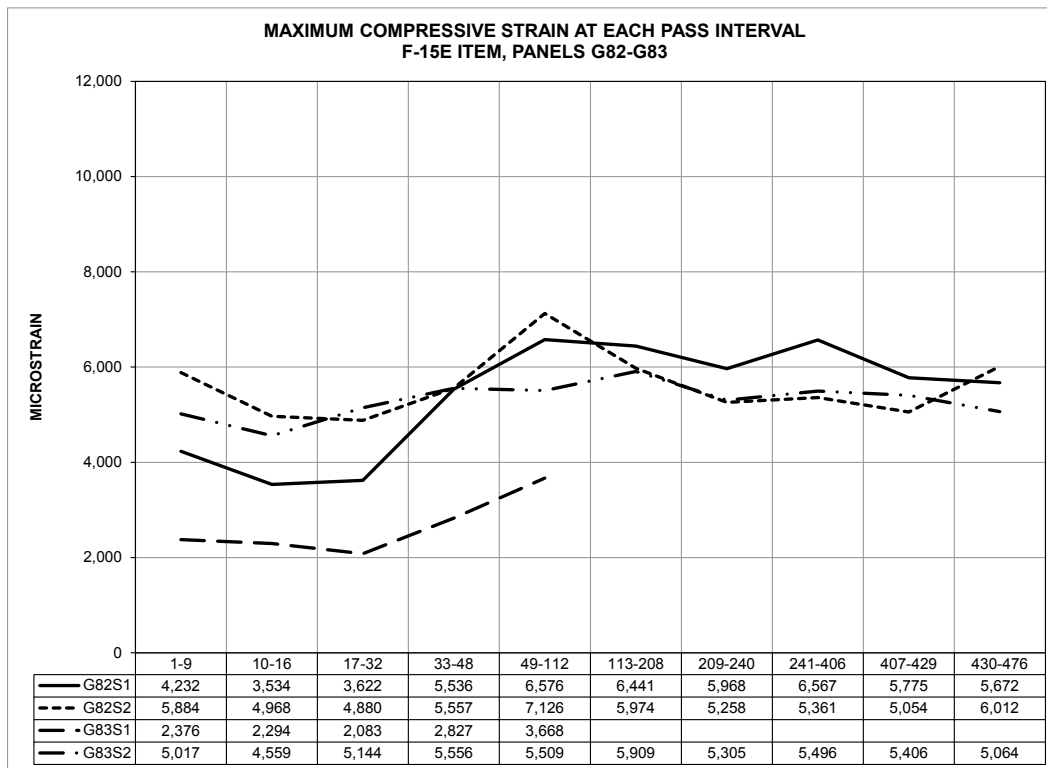


Appendix B: F-15E Item Strain Gage Data Summary

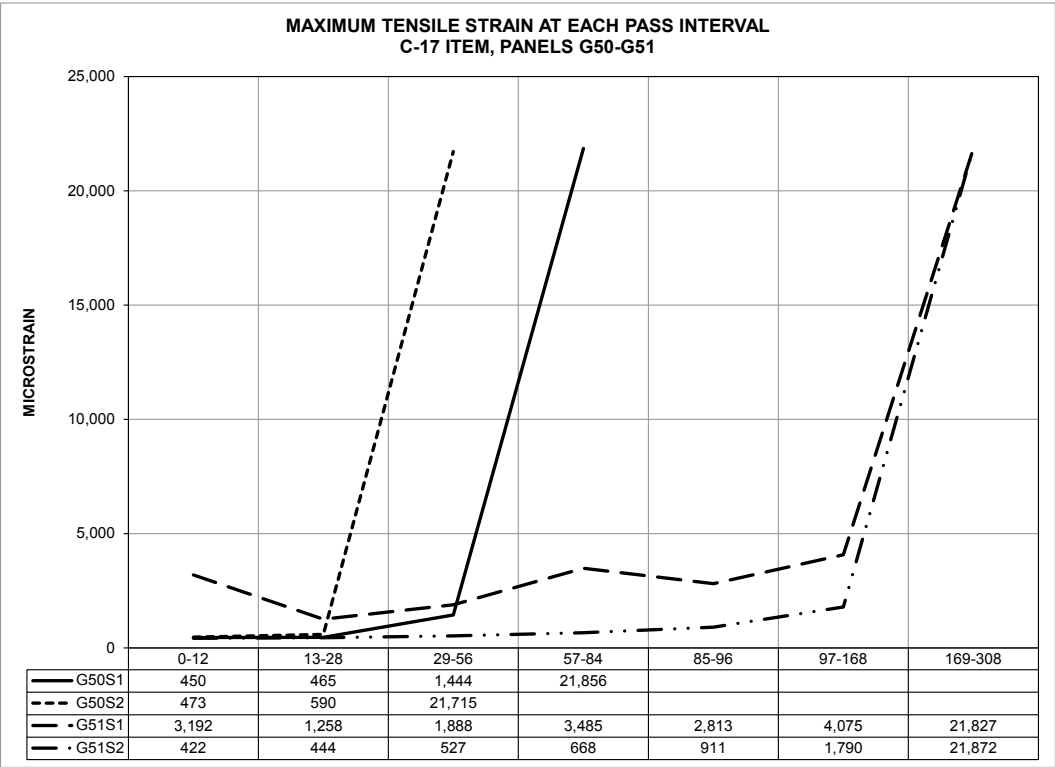
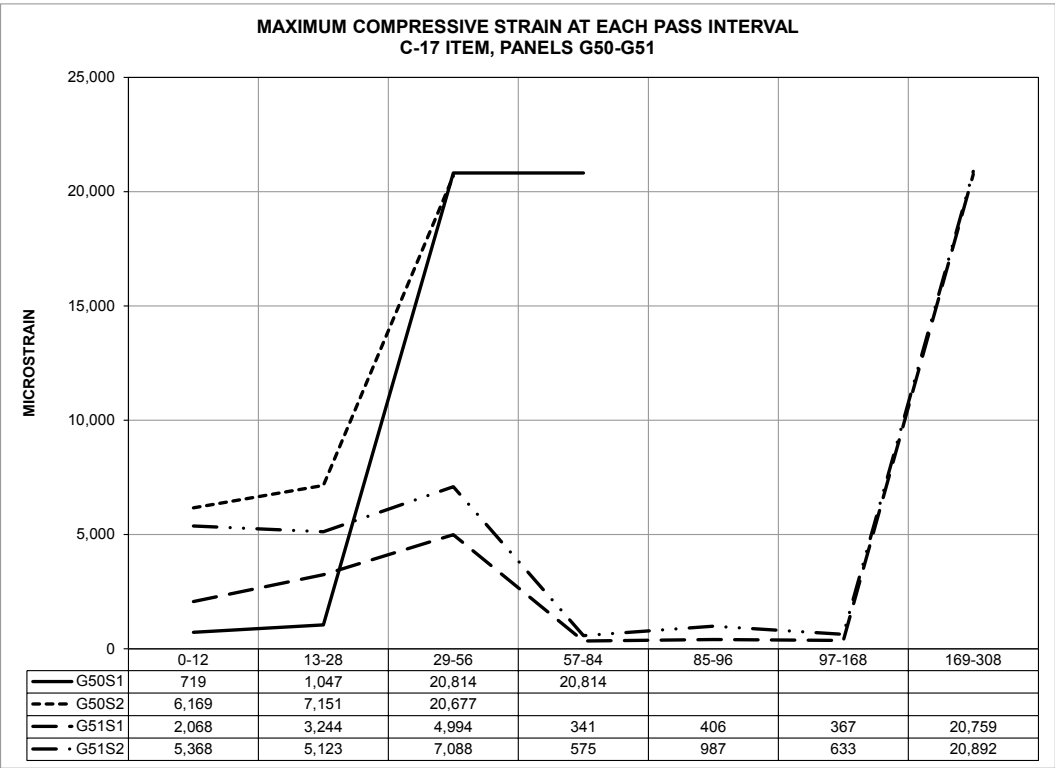


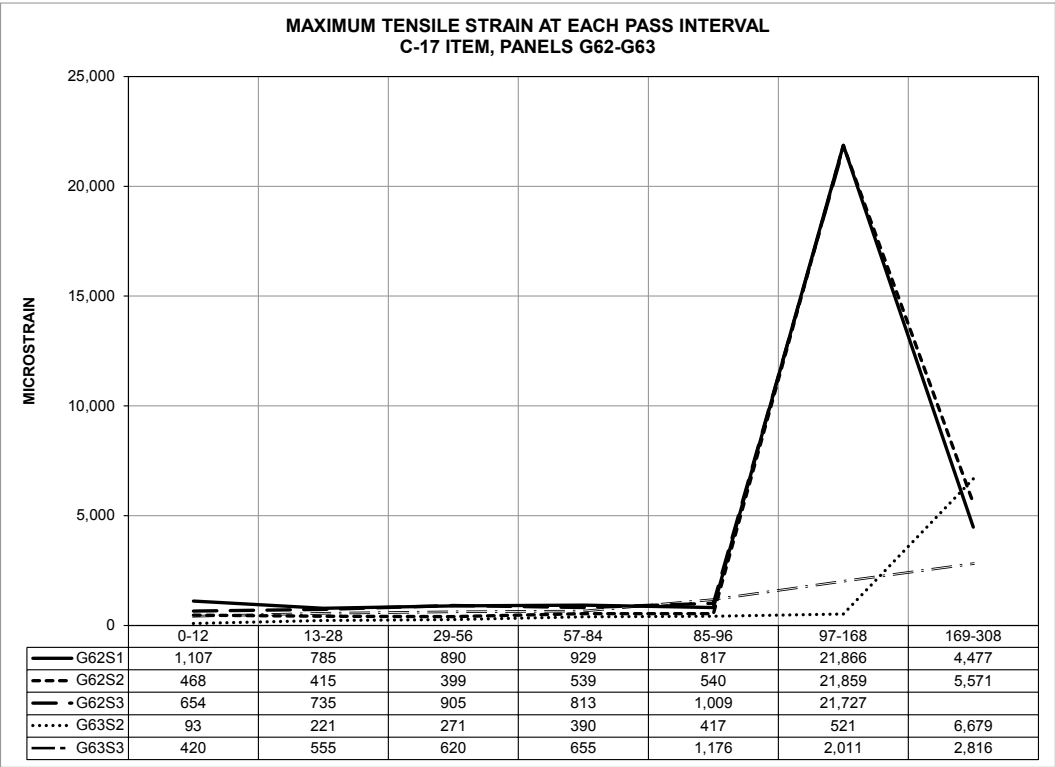
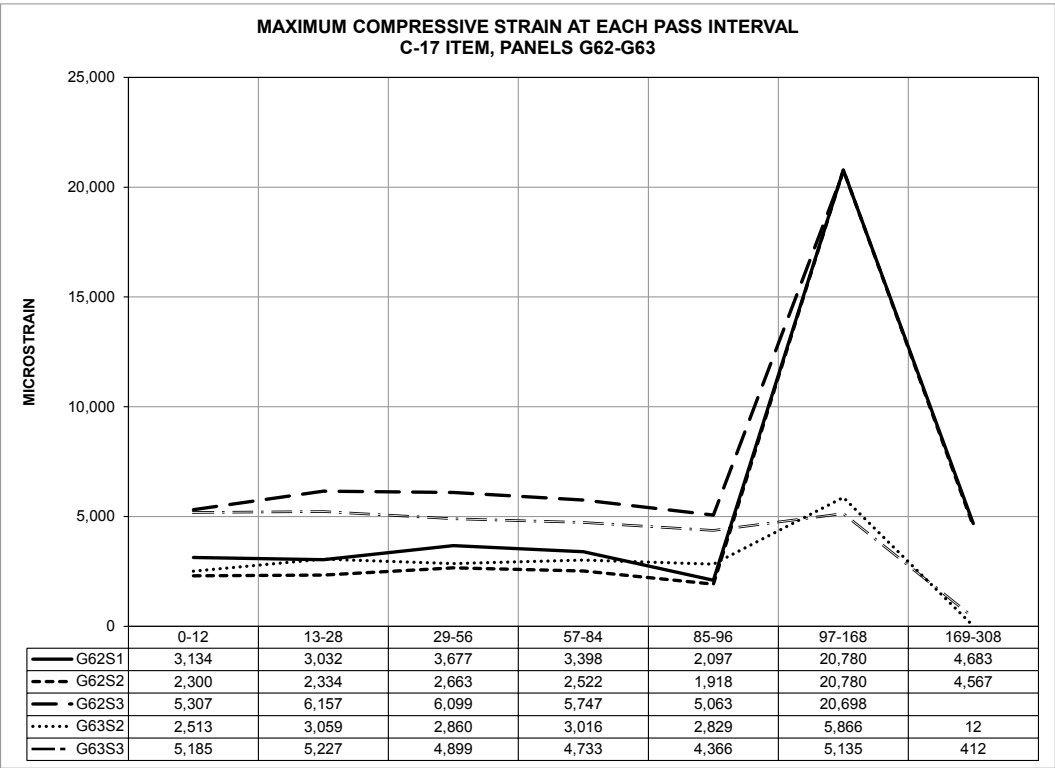


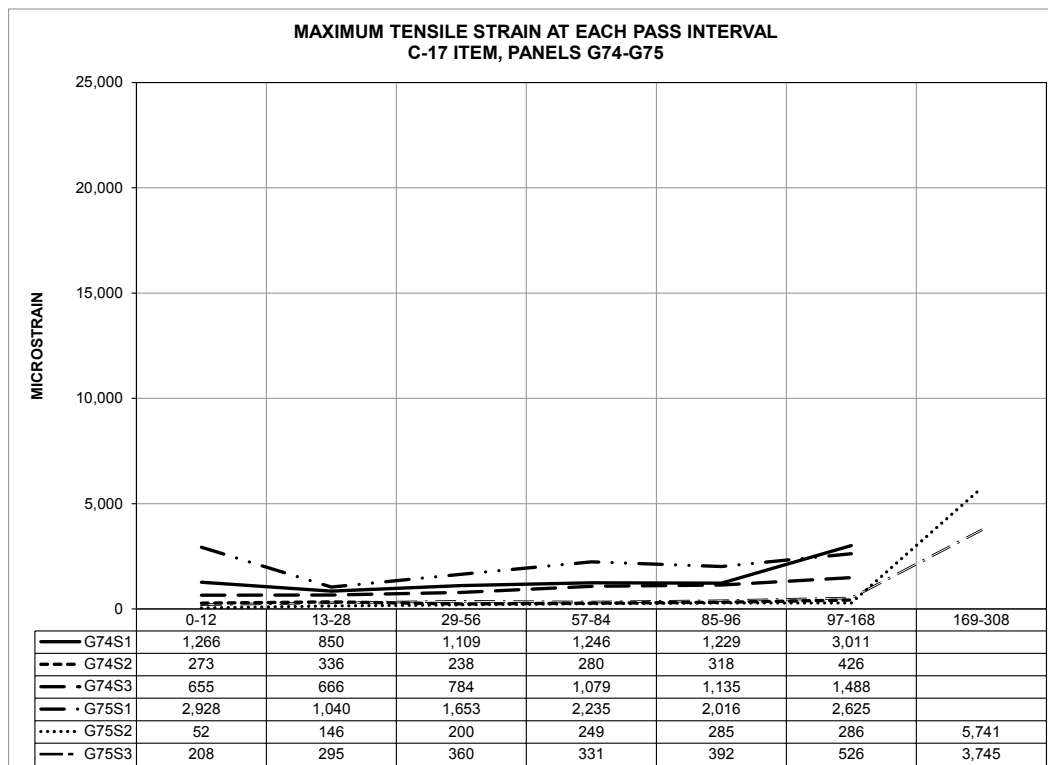
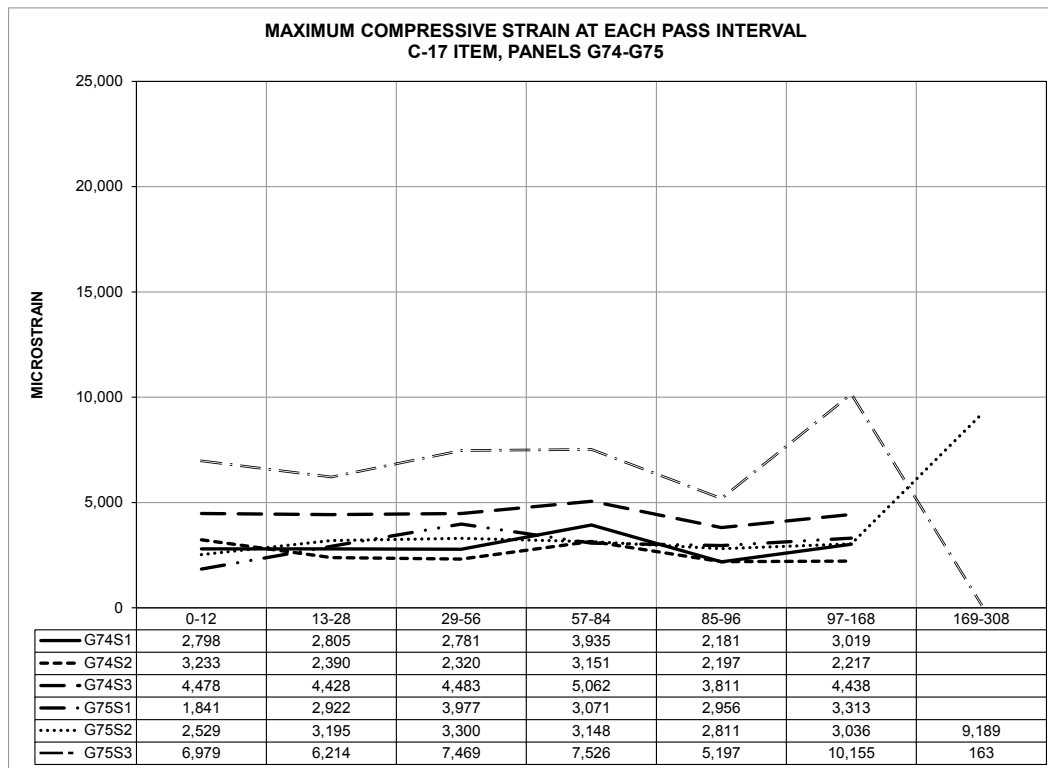


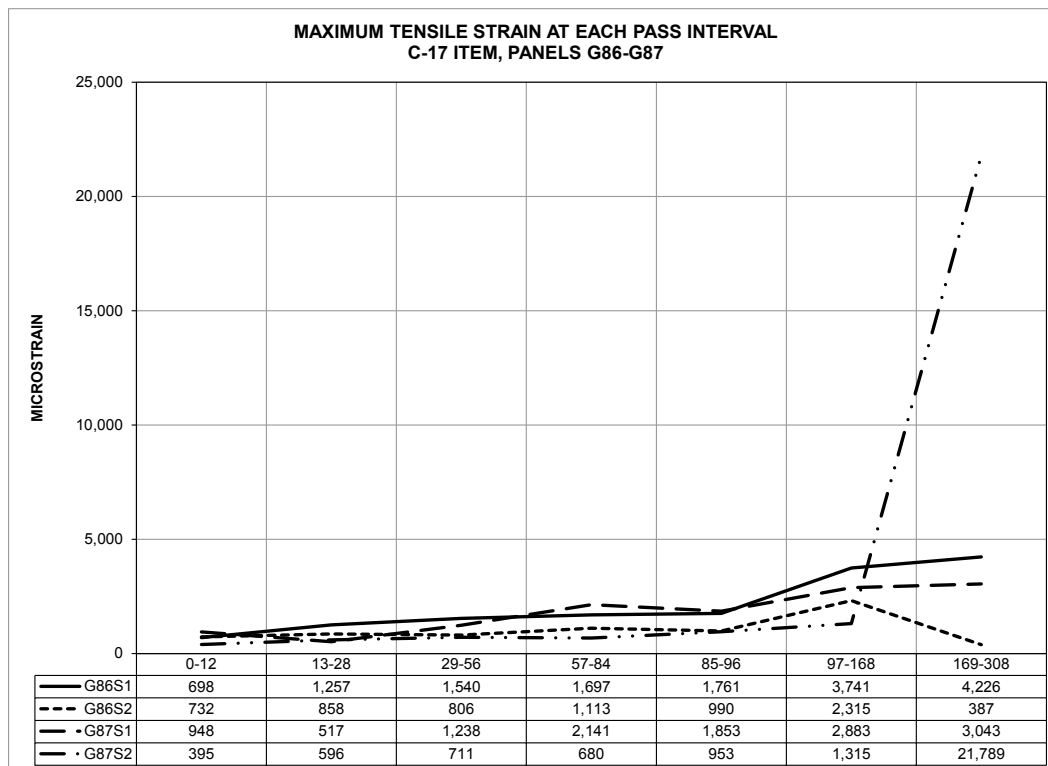
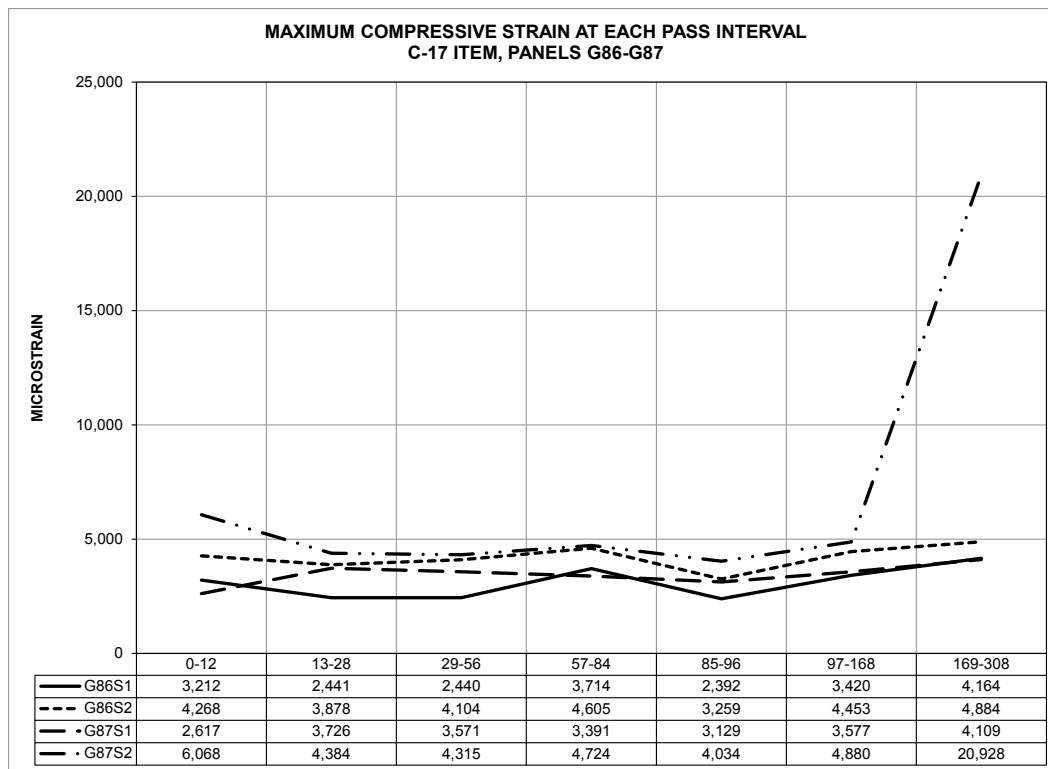


Appendix C: C-17 Item Strain Gage Data Summary









REPORT DOCUMENTATION PAGE

Form Approved
OMB No. 0704-0188

Public reporting burden for this collection of information is estimated to average 1 hour per response, including the time for reviewing instructions, searching existing data sources, gathering and maintaining the data needed, and completing and reviewing this collection of information. Send comments regarding this burden estimate or any other aspect of this collection of information, including suggestions for reducing this burden to Department of Defense, Washington Headquarters Services, Directorate for Information Operations and Reports (0704-0188), 1215 Jefferson Davis Highway, Suite 1204, Arlington, VA 22202-4302. Respondents should be aware that notwithstanding any other provision of law, no person shall be subject to any penalty for failing to comply with a collection of information if it does not display a currently valid OMB control number. **PLEASE DO NOT RETURN YOUR FORM TO THE ABOVE ADDRESS.**

1. REPORT DATE (DD-MM-YYYY) December 2016		2. REPORT TYPE Final report		3. DATES COVERED (From - To)																	
4. TITLE AND SUBTITLE AM2 Brickwork Pattern Evaluation				5a. CONTRACT NUMBER																	
				5b. GRANT NUMBER																	
				5c. PROGRAM ELEMENT NUMBER																	
6. AUTHOR(S) Lyan Garcia, Jeff Fisher, Timothy W. Rushing, and Jeb S. Tingle				5d. PROJECT NUMBER P2 457442																	
				5e. TASK NUMBER																	
				5f. WORK UNIT NUMBER FWIC 91796K																	
7. PERFORMING ORGANIZATION NAME(S) AND ADDRESS(ES) U.S. Army Engineer Research and Development Center Geotechnical and Structures Laboratory 3909 Halls Ferry Road Vicksburg, MS 39180-6199				8. PERFORMING ORGANIZATION REPORT NUMBER ERDC/GSL TR-16-34																	
9. SPONSORING / MONITORING AGENCY NAME(S) AND ADDRESS(ES) Headquarters, Air Force Civil Engineer Center Tyndall Air Force Base, FL 32403-5319				10. SPONSOR/MONITOR'S ACRONYM(S)																	
				11. SPONSOR/MONITOR'S REPORT NUMBER(S)																	
12. DISTRIBUTION / AVAILABILITY STATEMENT Approved for public release; distribution is unlimited.																					
13. SUPPLEMENTARY NOTES																					
14. ABSTRACT AM2 airfield matting has a long history of successful performance as an expeditionary airfield surfacing system. The U.S. Marine Corps established different lay patterns to assemble AM2 mat expanses that can be used to form aircraft operating surfaces. A program was initiated by the Naval Air Systems Command to evaluate and identify optimal AM2 lay patterns under different traffic conditions and to validate a Dynamic Interface Model with mat breakage, deformation, and recorded strain data. The efforts of the test program discussed in this report focused on evaluating an AM2 surface installed in a brickwork pattern on both a uniform subgrade surface and a subgrade with artificial voids to determine the effect of voids beneath the mat on the structural integrity of AM2. The mat surface was subjected to simulated F-15E and C-17 traffic while monitoring damage, deformation, and strain response. Premature failure was observed, but posttest investigations and analyses revealed a manufacturing error that produced a weak end connector design. This report provides test results for each evaluation and discussions comparing their performance to previous tests conducted under similar conditions.																					
<table border="0"> <tr> <td colspan="2">15. SUBJECT TERMS</td> <td>Expeditionary airfields</td> <td>Airfield surfacing system</td> </tr> <tr> <td colspan="2">AM2</td> <td>Aluminum mat</td> <td>Runways (Aeronautics)--Evaluation</td> </tr> <tr> <td colspan="2">Airfield mat</td> <td>Landing mats</td> <td>Strains and stresses</td> </tr> <tr> <td colspan="2"></td> <td></td> <td>Aluminum alloys--Fracture</td> </tr> </table>						15. SUBJECT TERMS		Expeditionary airfields	Airfield surfacing system	AM2		Aluminum mat	Runways (Aeronautics)--Evaluation	Airfield mat		Landing mats	Strains and stresses				Aluminum alloys--Fracture
15. SUBJECT TERMS		Expeditionary airfields	Airfield surfacing system																		
AM2		Aluminum mat	Runways (Aeronautics)--Evaluation																		
Airfield mat		Landing mats	Strains and stresses																		
			Aluminum alloys--Fracture																		
16. SECURITY CLASSIFICATION OF:			17. LIMITATION OF ABSTRACT	18. NUMBER OF PAGES	19a. NAME OF RESPONSIBLE PERSON																
a. REPORT UNCLASSIFIED	b. ABSTRACT UNCLASSIFIED	c. THIS PAGE UNCLASSIFIED	SAR	121	19b. TELEPHONE NUMBER (include area code)																